Interaction between extended and localized electronic states in the region of the metal to insulator transition in semiconductor alloys

DISSERTATION

zur Erlangung des Doktorgrades
der Naturwissenschaften
(Dr. rer. nat.)

vorgelegt von

Jörg Teubert

I. Physikalisches Institut
Justus-Liebig-Universität Gießen

– anno 2008 –

To My Family

Contents

1 Introduction

One of the main reasons why semiconducting materials proved to be so extremely useful for device applications is the possibility of doping which allows for significant modifications of the electronic properties of semiconductors. Mostly, the electronic states related to impurities are localized in space. In fact, localized states provide a huge variety of interesting physics, especially at low temperatures where they govern the properties of semiconductors almost completely.

In the case of donors or acceptors, localized states determine whether a semiconductor appears as an insulator or as a metal at low temperatures. It is well known that the material can undergo an insulator to metal transition when their concentration is raised above some threshold. This phenomenon has been studied extensively during the past decades and nevertheless many unanswered questions persist, as for instance the influence of correlation effects.

With the appearance of new material systems such as (Ga,In)(N,As), scientists gained huge possibilities to design new devices for electronic or optoelectronic applications. Again localized states, or more precisely localized states of isovalent impurities, play a major role in the understanding of their properties. The knowledge of their influence especially on the transport properties is essential for performing effective device design. In this context, the material system (B,Ga,In)As turns out to be a very interesting system from a fundamental point of view. Isovalent boron is found to generate highly localized states resonant with the conduction band. These states are very close to the conduction band edge, which makes them accessible by applying hydrostatic pressure. Chapters 4 and 5 will address the influence of isovalent localized states on the electronic and thermoelectric properties of (B,Ga,In)As and (Ga,In)(N,As). It will be shown that a subtle interplay between localized states and extended states of the host crystals takes place.

The last chapter will address the influence of magnetic interactions on the transport properties near the metal-insulator transition (MIT). The first part of that chapter focuses on $Zn_{0.94}Mn_{0.06}Se$:Cl, a representative of so called dilute magnetic semiconductors (DMS). In this material Mn^{2+} ions provide a large magnetic moment due to their half filled inner 3d-shell. It is well known that the resulting interaction between these localized magnetic moments and the electron spins leads to a spin splitting of the band states. However, little is known about the modifications of the impurity band transport due to magnetic interactions. It will be shown that magnetic interactions in conjunction with disorder effects

are responsible for the unusual magnetotransport behavior found in this and other II-Mn-VI semiconductor alloys. In the second part, a different magnetic compound, namely InSb:Mn, is of interest. It is a representative of the III-Mn-V DMS, where the magnetic impurity Mn serves both as the source of a large localized magnetic moment and as the source of a loosely bound hole due to its acceptor character. Currently in this area the main interest lies on obtaining ferromagnetic semiconductors with Curie temperatures above room temperature for application in semiconductor spintronic devices. In order to achieve this goal one usually attempts to raise the magnetic ion content within the semiconductor to a few percent. Samples with low magnetic impurity content are less important in this context and little is known about the influence of magnetic donors or acceptors on the metal-insulator transition up to now. However, as it will be shown, there exists an extremely interesting doping regime close to the metal-insulator transition where localized states of magnetic impurities can dramatically alter the transport properties. Chapter 6.2 will try to shed some light on this topic by comparing magnetic InSb:Mn and nonmagnetic InSb:Ge which reveal distinct differences in their electric resistivity near the metal-insulator transition.

This thesis is structured as follows. The first chapter provides information about the experimental techniques used in the framework of this work and gives a detailed description of the various experimental setups. The following chapter has introductory character and is supposed to present the fundamentals of doped semiconductors with emphasis on transport phenomena and the metal-insulator transition. The last three chapters present the results obtained as indicated above. In the last section an outlook for further research is given.

2 Experimental methods

An investigation of the metal-insulator transition of semiconductors of course requires the application of transport measurements as the main method for characterization. The static conductivity was probed while varying temperature, magnetic field and hydrostatic pressure. Since thermoelectric measurements can yield useful information as well, a setup for measurements of the Seebeck coefficient was used. When necessary and possible, the results were backed up by optical measurement techniques such as Raman scattering or modulation spectroscopy. The following sections will describe the different experimental setups.

2.1 Magnetotransport measurements

Figure 2.1 shows a schematic drawing of the experimental setup used for magnetotransport measurements. The samples were mounted inside an Oxford Instruments magnet system. Its superconducting coil generates magnetic fields of up to 10 T. The variable temperature inset allows a variation of the measurement temperature in the range from 1.5 K to 300 K. A calibrated 'Cernox'-temperature sensor placed directly below the sample assures a very accurate determination of the sample temperature. All magnetotransport measurements were performed in van der Pauw geometry [1, 2].

Electrical connection to the measurement devices is done in the so called guarded circuit technique [3] using Keithley triaxial cables to assure high signal to noise ratio and to prevent leakage currents. The Keithley Hall-Effect Card 7065 with excellent signal to noise characteristics is used as a switching unit. The measurement current is generated by a stabilized DC current source (Keithley 220) and the current and voltage measurements are carried out by a picoammeter (Keithley 6485) and a nanovoltmeter (Keithley 2182). A specially designed measurement software is used to control and monitor all devices, which allows an extensive automation of the whole measurement procedure. In the case of magnetic field dependent measurements, the software provides a precise control of the measurement temperature over the whole period of one measurement (a typical duration for a standard field-dependent measurement would be 3 hours). This is of great importance, since the van der Pauw geometry makes it necessary to average between $\rho, R_H(-B)$ and $\rho, R_H(+B)$. Because the magnetic field is usually swept from $-B$ to B, some of these two values are measured with a time difference of several hours. Therefore, precise control of temperature variations

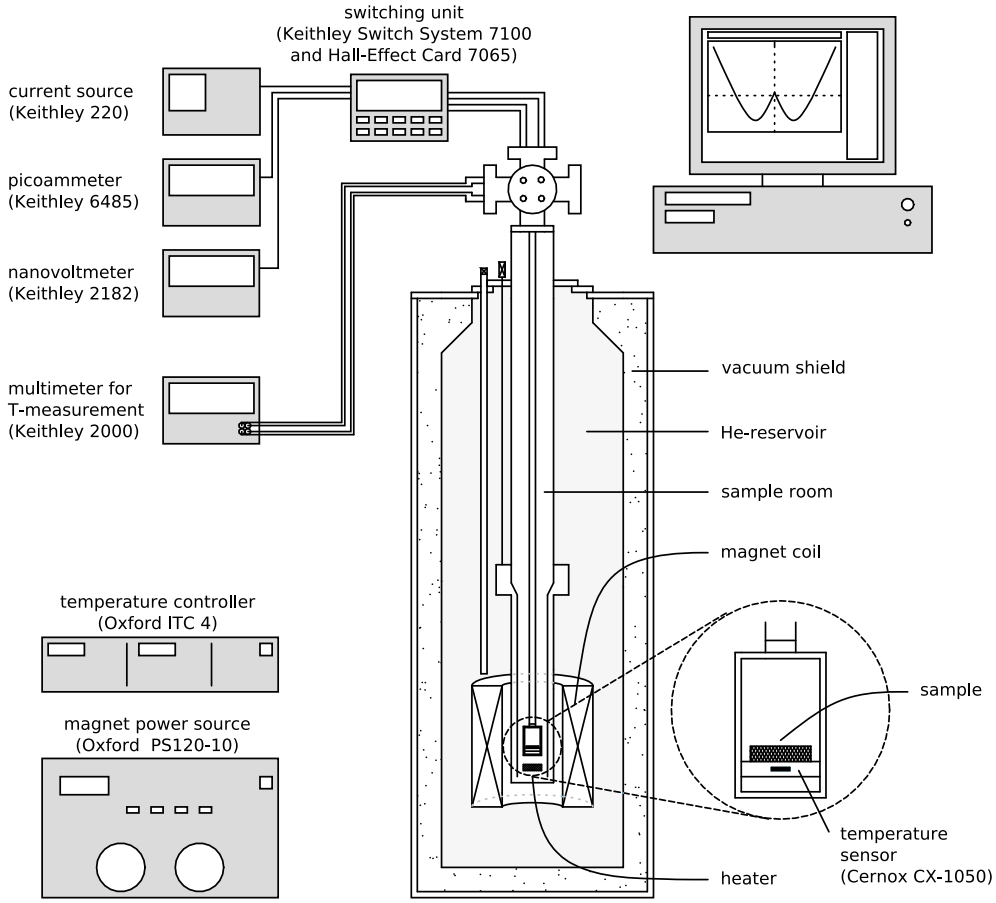

Figure 2.1: Schematic drawing of the experimental setup used for magnetotransport measurements.

is crucial and not more than $\pm 0.1\,\mathrm{K}$ were tolerated at low temperatures. For all measurements indium was used as contact material. It was allowed to diffuse into the epitaxial layer by keeping the sample piece at $400^\circ\,\mathrm{C}$ under argon atmosphere for a period of 10 minutes.

2.2 Thermopower — measurement of the Seebeck effect

In the presence of a temperature gradient between different areas of a given material, a voltage ΔU_{Th} is built up which is proportional to the temperature difference ΔT between the two areas. This phenomenon is known as the thermoelectric effect. The factor of proportionality is the Seebeck coefficient (or thermopower) S:

$$U_{\mathrm{Th}} = S\Delta T \tag{2.1}$$

The thermopower determines the average energy, with respect to the Fermi level, which is transported by charge carriers under the influence of a thermal gradient, and is therefore informative as it provides alternative information concerning the main conduction path.

The samples used for the thermoelectric measurements have been cleaved into stripes of typical dimensions of 3–5 mm in width and 10–15 mm in length. Figure 2.2 schematically illustrates the basic measurement principle and provides details of the experimental setup. A temperature gradient ΔT was established along the sample stripe by independently controlled heaters causing a thermoelectric voltage $\Delta U_{\mathrm{Th}} = S\Delta T$ between its ends. Two small indium contact areas were attached about 1 to 2 mm from the ends of the stripes, indicated by numbers 1 and 2 in fig. 2.2. Electrical connection was achieved by two standard thermocouples (type E: NiCr/CoNi) that were soldered into the contacts. This simple arrangement of two thermocouples is sufficient to extract all necessary information for determining the Seebeck coefficient by measuring the voltage between two of the four legs at a time. In more detail: The voltages between two legs of the same thermocouple (U_{T_1}, U_{T_2}) yield information about the temperature at the contact points (T_1, T_2), whereas the voltages between the legs made of the same material ($U_{\mathrm{Th,\,CoNi}}$, $U_{\mathrm{Th,\,NiCr}}$) provide two equivalent measurements of the thermoelectric voltage. The advantage of this setup, besides its simplicity, is the following: Because of the thermal conductivity of the substrates and the relatively bad thermal contact to the heaters that generate the temperature gradient, it is crucial to measure the exact temperature at the contacts used for the determination of the Seebeck voltage. This is automatically achieved by soldering the CoNi/NiCr thermocouples into the In contact material.

Since this experimental setup was built up entirely within the time period of this thesis, some of its details shall be explained more precisely in the following. Indium was used as contact material which is known to form ohmic contacts on GaAs-based semiconductors. The indium was allowed to diffuse into the epitaxial layer by heating the sample to 400°C for 10 min under Ar-atmosphere. The thermocouples soldered to the contacts were made from plain commercial CoNi and NiCr wires of a thickness of either 30 µm or 80 µm. In order to prevent heat flow through the measurement wires, they were chosen to be as thin as practicably feasible. In order to establish a temperature gradient, the samples were mounted on copper blocks that can be heated independently by standard resistors. The heating blocks are mounted on a copper ground plate which is attached to the cooling finger of a modified liquid helium continuous flow cryostat that allows for measurements in the range from 40–300 K. The position and relative distance of the copper blocks can be adjusted so that samples of different size can be inserted. Since the samples were epitaxial layers grown on semi-insulating substrates, no further insulation was needed. The samples are held on the copper blocks with teflon clamps to allow for slight movements on the copper blocks. For better thermal contact insulating heat conducting paste was used. This semi-elastic mounting technique is necessary to prevent the sample from breaking loose from the heaters due to different thermal expansion-

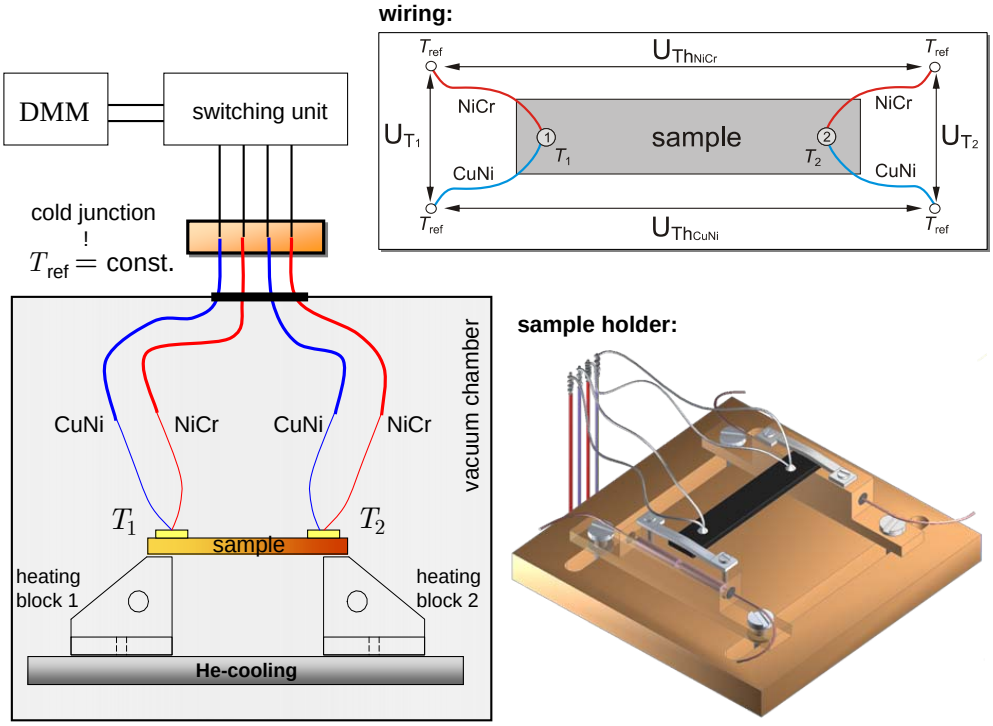

Figure 2.2: Schematic illustration of measurement principle. Two thermocouples soldered into the contact areas are used both for determining the temperature gradient and the thermovoltage.

coefficients between sample and holder and thus to ensure good thermal contact at all measurement temperatures.

The thin bare measurement thermowires are attached to thicker wires of the same material leading outside the cryostat and towards the reference junction. Electrical contact between thin and thick wires has to be made by clamping both together using teflon ribbon. Because fabrication tolerances and differences in alloy composition between those two types of wires are not negligible, any temperature difference at these junctions produces additional voltages and can disturb the measurement. Therefore, all four junctions are held close to each other and in a symmetrical arrangement to the cooling finger of the cryostat.

The same problem occurs at the reference junction. The slightest temperature difference among the four junctions has dramatic influence on the accuracy of the measurement of the thermovoltages, especially at low temperatures. Usually this problem is addressed by keeping the reference junction(s) at constant temperature. This, however, is difficult to achieve experimentally with the demanded accuracy and over the long periods of time (several days) for a complete measurement. Therefore, a different ansatz is used. The temperature of the reference junctions are held at a semi-constant but precisely known value. The junctions are embedded into a solid copper block whose cavity had been filled

with an electrically insulating but heat conducting paste which was placed into a thermally insulating dewar. Due to a large heat capacity of the copper block and the insulation layer, this offers protection against sudden changes of the reference temperature. However, gradual changes are constantly determined with great accuracy in equal time intervals during the whole thermopower measurement. This is done by using a calibrated PT100 temperature sensor that had been embedded in the copper block nearby the reference junctions and that allowed the measurement of the reference temperature at an accuracy of 0.01 K. For the calculation of T_1 and T_2, this time dependent reference temperature is taken into account. With this technique the reference junction is not held at a constant value as usually done but is measured with great accuracy during the whole thermopower measurement.

The switching between the several measurement configurations (see above) is done using a Switch System (Keithley 7100) with an attached matrix card (Keithley Hall-Effect Card 7065) which provides an excellent state of the art signal to noise ratio. The voltages are determined using a Keithley Voltmeter 2700 with integrated multiplexer card that allows for measurements of additional parameters, as e.g. the heating power. All devices are controlled by a specially developed LabVIEW-based measurement software.

Since it is impossible to make the two contacts on the sample completely identical and purely ohmic, an additional contact potential may develop which distorts the thermopower measurement by creating an offset in the function of $\Delta U(\Delta T)$. Therefore, it is not sufficient to measure the Seebeck voltage just for one temperature gradient. In order to suppress these influences it is in fact indispensable to measure ΔU at different temperature gradients ΔT while keeping the average temperature $T_{\mathrm{avg}} = \frac{1}{2}(T_1 + T_2)$ constant. The Seebeck coefficient is then determined from the slope of $\Delta U(\Delta T)$ using a least squares fit.

The use of a semi-insulating substrate guarantees that the epitaxial layer, though orders of magnitude thinner, completely determines the overall measured Seebeck voltage. According to [4] the following relation holds:

$$S_{\mathrm{total}} = \frac{\sigma_{\mathrm{sub}}}{\sigma_{\mathrm{epi}} + \sigma_{\mathrm{sub}}} S_{\mathrm{sub}} + \frac{\sigma_{\mathrm{epi}}}{\sigma_{\mathrm{epi}} + \sigma_{\mathrm{sub}}} S_{\mathrm{epi}} \tag{2.2}$$

with S, σ_{sub} and S, σ_{epi} denoting the Seebeck coefficient and conductivity of the substrate and epitaxial layer, respectively. As the conductivity of the semi-insulating substrate is many orders of magnitude lower, the Seebeck effect of the substrate can be neglected.

With this setup accurate thermopower measurements using reasonable temperature gradients are achievable for temperatures in the range of 50 K to 300 K.

Influence of the measurement wires

A principle issue that has to be considered is the influence of the measurement wires on the absolute Seebeck coefficient of the sample. Following the path of one type of measurement wires in fig. 2.2, it holds for the measured thermovoltage:

$$U_{\text{measured}} = S_{\text{wire}}(T_{\text{ref}} - T_1) + S_{\text{sample}}(T_1 - T_2) + S_{\text{wire}}(T_2 - T_{\text{ref}}) \tag{2.3}$$

where U_{measured} denotes the measured voltage, T_1 and T_2 are the temperatures at the samples contact points, T_{ref} the temperature at the reference junction and S_{wire} the Seebeck coefficient of the measurement wires. Therefore, the Seebeck coefficient of the sample under study has to be corrected according to

$$S_{\text{sample}} = S_{\text{measured}} + S_{\text{wire}}. \tag{2.4}$$

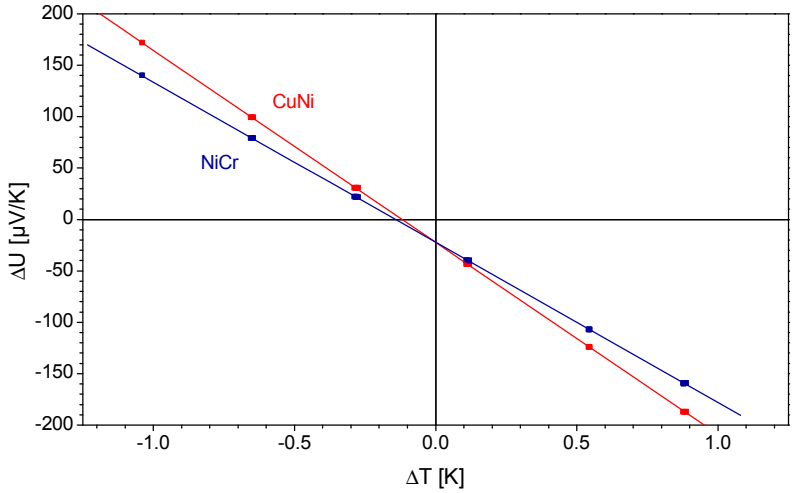

Figure 2.3: Thermopower measurements of an exemplarily chosen n-(Ga,In)(N,As) sample at 100 K. The two different slopes that stem from the usage of either CuNi or NiCr wires are clearly visible. The offset in the linear relation requires measurements at several ΔT for each $S(T_{\text{m}})$.

In order to illustrate the relevance of this issue, fig. 2.3 depicts measurements for one exemplarily chosen n-type (Ga,In)(N,As) sample. The different slopes that stem from the use of either CuNi or NiCr wires are clearly visible. Consequently the temperature dependences of the Seebeck coefficients of NiCr and CuNi have to be known in the measurement range from 50–300 K. In the case of CuNi one can exploit

$$S_{\text{CuNi}} = S_{\text{Cu}} - S_{\text{Cu/CuNi}} \tag{2.5}$$

with S_{Cu} being the absolute Seebeck coefficient of copper and $S_{\text{Cu/CuNi}}$ the Seebeck coefficient of the standardized thermocouple of type T (Cu/CuNi). The

data for type T thermocouples after standard ITS-90 were taken from [5], S_{Cu}-data had been provided by J. Nyström [6] and were approximated by a polynomial least squares fit. When S_{CuNi} is known, the relation

$$S_{\mathrm{NiCr}} = S_{\mathrm{NiCr/CuNi}} - S_{\mathrm{CuNi}} \tag{2.6}$$

yields information about the second wire material with $S_{\mathrm{NiCr/CuNi}}$ being the Seebeck coefficient of the type E thermocouple itself. The available data could then be represented analytically using a least-squares fit by polynomial functions. These are

$$\begin{aligned} S_{\mathrm{CuNi}} &= \sum_{i=0}^{5} a_i \, (T/K - 273.15)^i \frac{\mu V}{K} \qquad (2.7) \\ \text{with:} & \\ a_0 &= -37.01801 \\ a_1 &= -0.08233 \\ a_2 &= +1.18051 \times 10^{-4} \\ a_3 &= -1.55014 \times 10^{-7} \\ a_4 &= +2.11826 \times 10^{-9} \\ a_5 &= +9.03261 \times 10^{-12} \end{aligned}$$

and

$$\begin{aligned} S_{\mathrm{NiCr}} &= \sum_{i=0}^{5} b_i \, (T/K - 273.15)^i \frac{\mu V}{K} \qquad (2.8) \\ \text{with:} & \\ b_0 &= +21,42199 \\ b_1 &= +0,02468 \\ b_2 &= -7,51875 \times 10^{-5} \\ b_3 &= +2,4623 \times 10^{-7} \\ b_4 &= +1,32233 \times 10^{-9} \\ b_5 &= +9,03261 \times 10^{-12} \end{aligned}$$

2.3 Modulation spectroscopy

Modulation spectroscopy measures the relative changes of the optical quantities reflectance R or transmission T due to an external modulation. The modulation can in general be achieved in various ways, such as modulation of temperature, pressure, wavelength of incident light, external electrical field etc. The advantage of the measurements of the relative quantities, e.g. $\Delta R/R$, is the following:

Whereas measurements of R often suffer from rather large spectral broadening of the signals, the objective of modulation spectroscopy is to obtain sharp, well resolved spectra. The lineshapes of bulk semiconductor materials observed in modulation techniques have been shown to be closely related to the third derivative of the unperturbed dielectric function [7]. As a consequence, modulation spectroscopy is characterized by a strongly enhanced sensitivity at critical points of the band structure and strongly suppressed background effects. Thus one obtains sharp, derivative like signals at points of the Brillouin zone with a high combined density of states. Additionally, corrections for the spectral response of the experimental setup are automatically included. The modulation can affect an optical transition in either energetic position, spectral width or its intensity (transition probability). The lineshape of the modulated signal is finally determined by the relative contribution of the changes of these three parameters.

The two techniques used in the context of this work are electromodulated spectroscopy (ER) and photomodulated spectroscopy (PR). In both cases electrical fields are the modulated quantities. In ER-measurements the modulation is caused by an externally applied, alternating electrical field. In PR-measurements the incident light causes excited carriers in the sample which reduce the built-in electric field due to band bending at the surface.

Photomodulated reflectance

The experimental setup used for photomodulated measurements is sketched in fig. 2.4. A 0.25 m spectrometer was used to spectrally disperse the white light of a halogen lamp into its wavelength spectrum and to yield tunable monochromatic probe light. This probe light was then focused onto the sample surface and the reflected light was detected using a Si-photo diode. Both the DC-part and the modulated AC-part of the total detector signal were measured using a DC-voltmeter and a lock-in-amplifier, respectively. As the source for the modulated light field a HeCd-laser with wavelength of 442 nm together with a mechanical chopper wheel was used. Typical modulation frequencies were several 100 Hz. An optical edge filter was placed in front of the detector in order to exclude any reflected laser light, as it would otherwise produce a large unwanted modulation signal. As it is necessary to subtract a constant photoluminescence-background from the ΔR-signal, the lock-in-signal was measured with the path of the white light blocked before each measurement. At the same time the signal-phase of the lock-in amplifier was set (with respect to the samples photoluminescence signal). For temperature dependent measurements, the sample was mounted into a liquid helium continuous flow cryostat that allowed for measurement temperatures between 10 K and 300 K.

Contactless electromodulated reflectance

In contactless electromodulated reflectance measurements (CER) one uses an externally applied electric AC field as the modulation. The schematic drawing

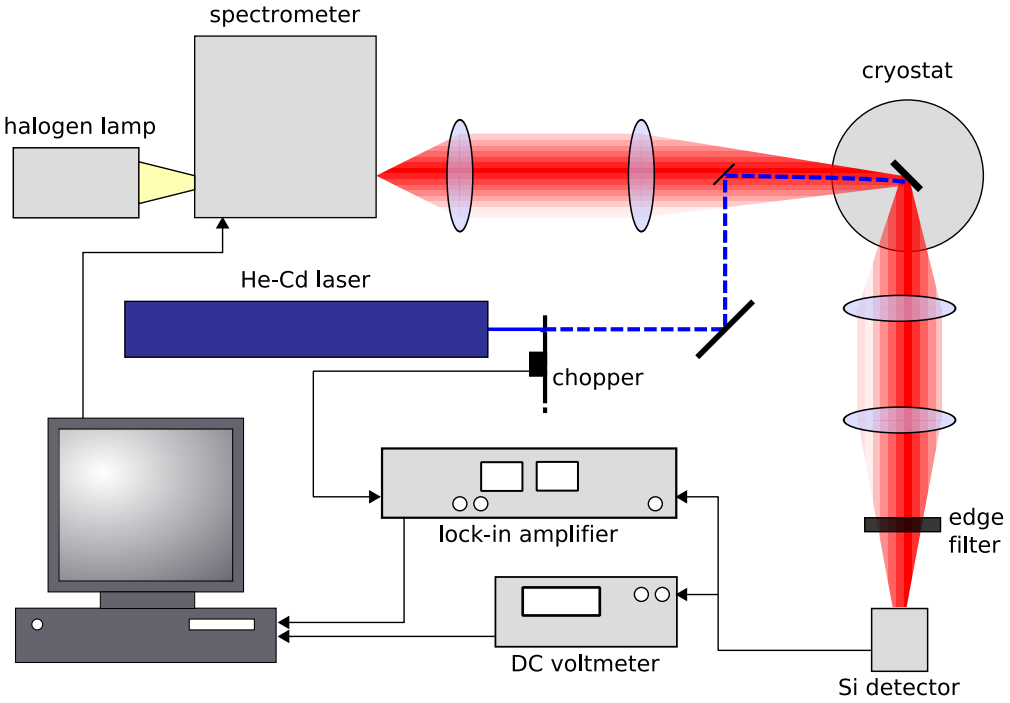

Figure 2.4: Schematic illustration of the measurement setup used for PR-measurements.

of the sample holder is given in fig. 2.5. The sample is mounted into a parallel-plate capacitor having a transparent electrode on one side. This electrode is made out of a thin glass disc coated with a conducting layer of indium-tin-oxide (ITO). The final distance between the sample surface and the transparent electrode can be adjusted with a screw to be in the range of approximately 100 µm. The alternating field in the capacitor is generated using the output of a waveform generator in conjunction with a high-voltage amplifier which allowed for amplitudes in the kV-range and a broad frequency range. The measurements shown

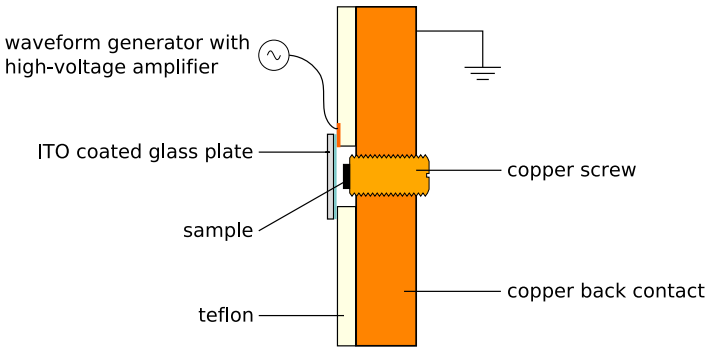

Figure 2.5: Sample holder used for contactless electromodulated reflectance (CER) measurements. The sample is mounted in a parallel-plate capacitor with a transparent plate on one side.

within this work were done at a frequency of approximately 300 Hz. A liquid helium continuous flow cryostat allowed to vary the measurement temperature, however limited to temperatures above 50 K due to the cryostat design. Besides the sample holder and the cryostat, the experimental setup was identical to the one used for photomodulated measurements. Of course, the use of the HeCd laser and an edge filter could be omitted, as well.

2.4 Raman spectroscopy

The Raman effect is based upon inelastic scattering of light by phonons and therefore provides useful information about the phonon structure of a material. It can be understood as a three step coherent process involving the incident photon, the interaction with the phonon system and an emitted photon of different energy. In the first step, the electronic system is excited by the incident photon into an intermediate state. This state can either be a real or a virtual state. In the case of a real state the transition matrix element (Raman intensity) is strongly enhanced and one speaks of resonant Raman scattering. In the second step, the electronic system wins or looses energy via electron-phonon interaction. In this process one or more phonons are either created (Stokes-effect) or absorbed (anti-Stokes effect). Finally a photon with different energy is emitted and detected. The experimental setup used within this work is a commercial 'inVia' Raman microscope from Renishaw plc. A schematic illustration of the optical path is shown in fig. 2.6. Here the light is focused via a standard microscope yielding increased light density on the sample surface and good spatial resolution. As an excitation source, the Renishaw system allows for three different laser wavelengths to be used: HeNe (633 nm), Nd:YAG (532 nm) and HeCd (325 nm). For UV measurements, of course, special quartz optics have to be used.

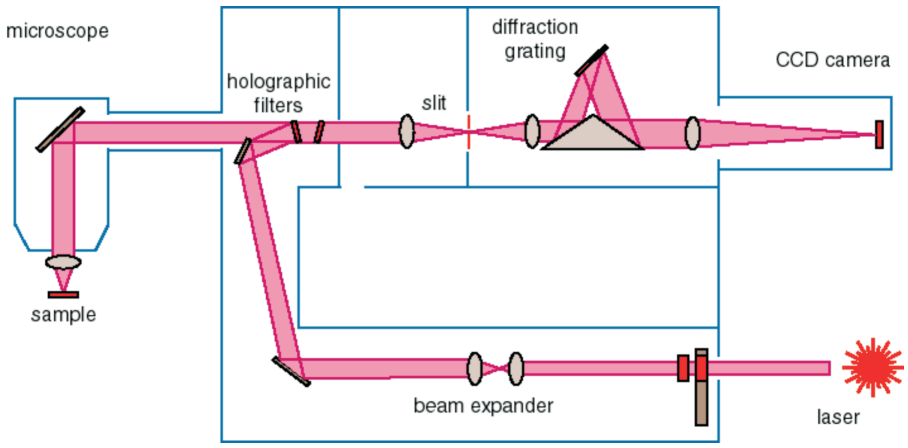

Figure 2.6: Schematic illustration of the Raman setup (provided by Renishaw plc.).

2.5 Measurements under hydrostatic pressure

Many of the measurements of this thesis were performed under hydrostatic pressure. For this purpose two different clamp-type pressure cells were available. One of them was designed for electrical measurements, while the other allows optical access.

Non magnetic clamp pressure cell for electrical measurements

The pressure cell used for magnetotransport measurements under hydrostatic pressure consists of a special non-magnetic copper-beryllium alloy. It allows to establish hydrostatic pressure in the range from 4 kbar up to 20 kbar at room temperature and 0.5 kbar to 16 kbar at 1.6 K. Figure 2.7 shows a schematic

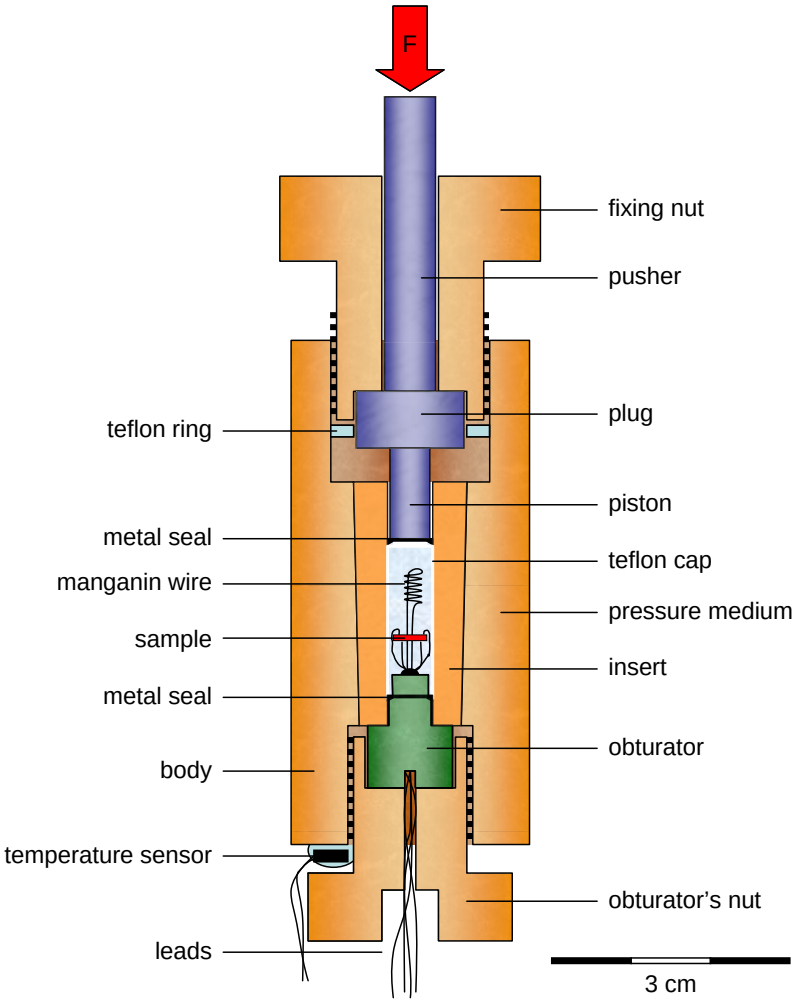

Figure 2.7: Schematic illustration of the nonmagnetic clamp pressure cell for electrical measurements under hydrostatic pressure.

drawing of its design. The samples used for measurements in the cell were about $3.5 \times 3.5\,\mathrm{mm}^2$ in size and had to be mounted on the obturator which was pushed into the inner opening of the cell. Kerosene was used as pressure transmitting medium. It is known to provide hydrostatic pressure even at low temperatures and high pressures. A teflon cap is used both for holding the pressure medium during cell loading and as a first seal at low pressure. At high pressure metal rings made from copper-beryllium ensured persistent sealing. The electrical contacts to the sample were made from Indium and were placed in van der Pauw geometry. After loading, the cell is placed in a hydraulic press and the pressure inside was adjusted as demanded. The cell had been calibrated using a coil of 5 cm manganin wire[1] which is a standard gauge in this pressure range. The details of this calibration process are given in [8]. A calibrated 'Cernox'-sensor was placed on the outside of the cell (outside the He-flow) to get information about the sample temperature. It was covered with heat conducting paste in order to assure good thermal contact. Because of the heavy metallic cell body, one can assume good agreement between the measured temperature outside the cell and the sample temperature inside[2].

Clamp pressure cell for optical measurements

The pressure cell used for optical measurements under hydrostatic pressure (fig. 2.8) is similar to the one just described. However, since it was not designed for measurements in magnetic fields, its body consists of steel and on one side a sapphire window (thickness of 4 mm) allows for optical access. The inner diameter is 6 mm. Due to its mechanical design the pressure range is limited to approximately 16 kbar at room temperature. The pressure transmitting medium used for the measurements was a mixture of methanol/ethanol (4:1) which is a standard medium for optical measurements under pressure.

Because the pressure medium etches the insulation of most electrical wires, a calibration with manganin wire is not possible, since electrical shortcuts cannot be excluded. Alternatives are the well known pressure shift of the GaAs bandgap or the use of the ruby pressure standard [9].

For measurements of photomodulated reflectance under hydrostatic pressure, the setup of fig. 2.4 had to be slightly modified, as shown in fig. 2.9. The use of the pressure cell requires a special geometry, since incident and reflected light have to enter and leave the cell at normal incidence. Therefore, a beam splitter is needed to extract the reflected light. Because of the beam splitter, the small aperture of the cell and the additional sapphire window the measurements under pressure suffer from a considerable loss in PR intensity.

[1] Manganin is an alloy consisting of 85% copper, 12.5% manganese and 2.5% nickel.

[2] Unfortunately, the sensor cannot be placed inside the cell, as no temperature sensors are available with known temperature, pressure and magnetic field dependence.

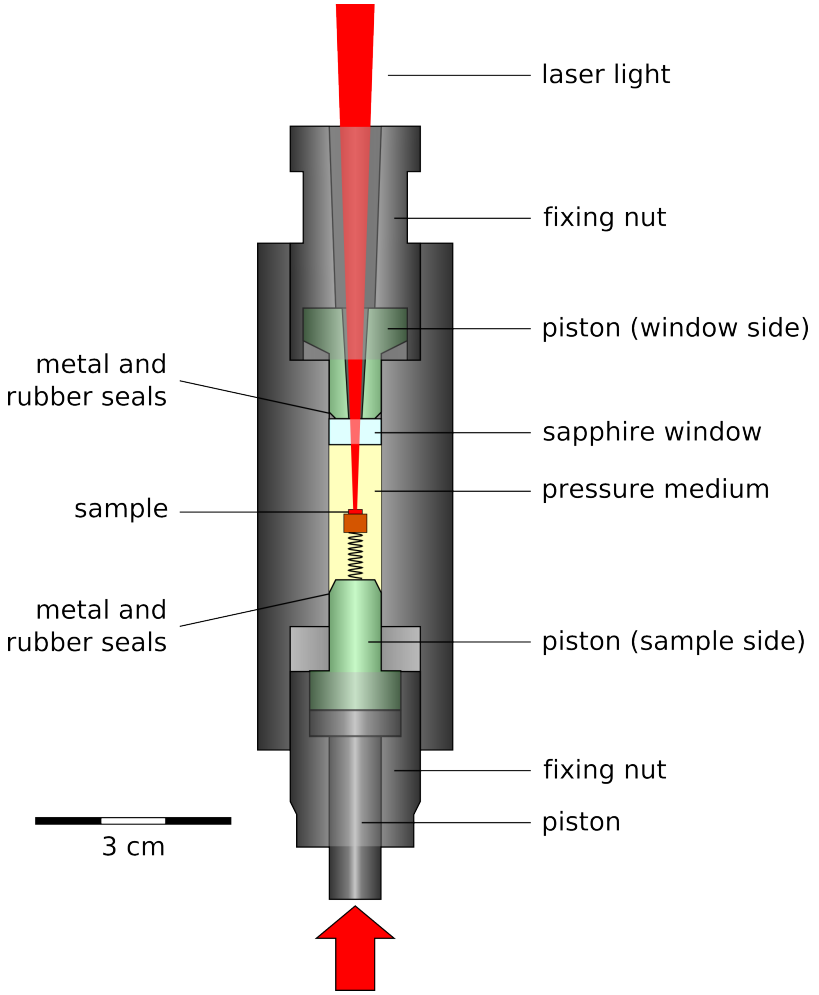

Figure 2.8: Schematic illustration of the clamp pressure cell with optical access.

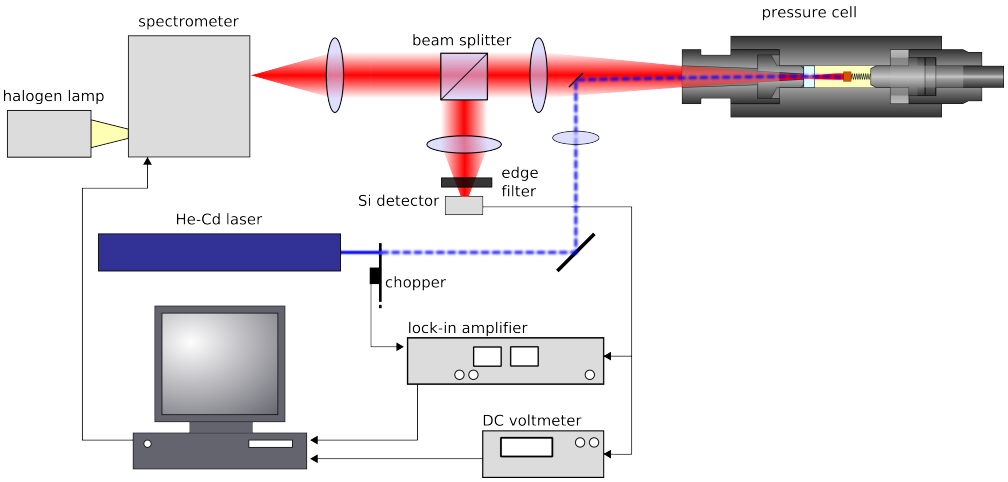

Figure 2.9: Schematic illustration of the measurement setup used for PR-measurements under hydrostatic pressure.

3 Some fundamentals of electronic properties of doped semiconductors

The most important way to manipulate the properties of semiconductors is doping, i.e. the replacement of some of the crystal's atoms with impurity elements that differ in the number of valence electrons. Donors provide more electrons than are needed to form crystal bonds, whereas acceptors provide less electrons introducing holes into the crystal. An impurity is called isovalent, if it possesses the same number of valence electrons as the atom it replaces. The ability for doping is the basis of every electronic or optoelectronic device containing semiconducting material. Most devices are supposed to work at room temperature and above. In this temperature range, doping almost exclusively serves as a tool to vary the resistivity via the free carrier concentration and to shift the Fermi energy close to one of the band edges. At low temperatures, which is the regime that will be considered in this work, impurities have a much greater influence on the transport properties. In this temperature range their characteristics and energetic distribution determine most of the electronic properties of semiconductors. This section will sketch out some of the most important consequences of the introduction of donor or acceptor states into semiconductor host crystals and will provide some of the fundamentals of the electronic properties of doped semiconductors. It will cover the phenomenon of a metal-insulator transition and will introduce the most important transport mechanisms.

3.1 Shallow impurities in semiconductors

The energy levels of donor and acceptor states are located in the forbidden gap between valence and conduction band. If the temperature is sufficiently high, these impurities can be ionized in the crystal. In the case of donors for instance, ionized impurities provide electrons to the conduction band that can participate in transport processes and therefore give rise to the electronic type of conduction in semiconductors. Besides their type (donor or acceptor), impurities are mainly characterized by their ionization energy $E_{\mathrm{D,A}}$. It is one of the most important parameters in the description of doped semiconductors, as it determines for instance the characteristic temperature for a carrier freeze-out, which will

be discussed below. The term *shallow* impurity characterizes an impurity with an energy level close to the conduction or valence band edge $E_{C,V}$, i.e. with small ionization energy. This corresponds to a defect potential that is slowly varying in space. It is interesting to note, that in the case of shallow impurities the structure and energy of an impurity state are almost independent of its particular chemical structure. In contrast, there exist deep centers that are mainly characterized by their large ionization energy. If the core (the atom without the outer valence electrons) of the impurity atom resembles the core of the host atom, the impurity levels tend to be shallow. If the impurity atom induces a strongly localized potential (such as a strain field around the impurity atom), the result is most likely a deep center. The part of the defect potential which is localized within one unit cell is known as a central cell correction. Closely related to the ionization energy is the so called localization radius which denotes a characteristic distance at which an electron can be localized near a shallow impurity center. For shallow impurities this distance is much larger than the lattice constant, which means that in a Fourier expansion only values of k in the vicinity of the band extremum have to be considered, which is the basis for the theory of the existence of an effective mass. Shallow impurities play a special role in semiconductor physics since they can be described uniformly with an effective hydrogen model[1]. The main results of this approach shall be presented in the following. A detailed analysis can be found in the review by Bassani et al. [10].

The hydrogen model

The eigenvalue problem of a shallow impurity center embedded in a host matrix coincides with the Schrödinger equation for a hydrogen atom, but with the effective mass m_{eff} of the electron or hole and the dielectric constant κ of the semiconductor. A band is called non degenerate, if it possesses no more than a twofold spin degeneracy near its extremal point. An example would be the conduction band in GaAs in contrast to the valence band which is degenerate at Γ. In the non-degenerate case the wave function of an impurity state is a Bloch function at the bottom of the band, modulated by a large-scale hydrogenlike function. The eigenvalues are

$$E_t = \frac{e^4 m_{\text{eff}}}{2\kappa^2 \hbar^2} \frac{1}{t^2} , \qquad t = 1, 2, \ldots \tag{3.1}$$

and the wave function of the ground state is of the form

$$\Psi(r) = (\pi a_{\text{B}}^3)^{-1/2} \, e^{-r/a_{\text{B}}} \tag{3.2}$$

where

$$a_{\text{B}} = \frac{\hbar^2 \kappa}{m_{\text{eff}} e^2} \tag{3.3}$$

[1] Central cell corrections violate the assumption that the defect potential is slowly varying in space. They can therefore not be described within the effective mass approximation and the effective hydrogen model is not applicable.

is an effective Bohr radius which determines a characteristic dimension of the wave function. In degenerate bands (e.g. valence band of GaAs) the situation is different because of different effective masses. The important parameter is the ratio $\beta = \frac{m_{\mathrm{lh}}}{m_{\mathrm{hh}}}$ of the light hole mass m_{lh} and the heavy hole mass m_{hh}. In case of disparate hole masses, the asymptotic behavior of the wave functions at large distances is governed by the light mass, while the binding energy is mainly determined by the heavy mass.

In the description of doped semiconductors, the properties of a single impurity (in the case of shallow impurities mainly the ionization energy and localization radius) are belonging to the main parameters. Another parameter of equal importance is the concentration of impurities $N_{\mathrm{A,D}}$. At high temperature, when all impurities are ionized, this quantity controls the resistivity via the number of free carriers that contribute to the charge transport. At low temperatures, when most impurities are neutral, the concentration is of great importance, as well. When both donors and acceptors are present, the semiconductor is said to be compensated, because under equilibrium conditions some of the donor electrons will be captured by acceptors leaving both ionized donors and acceptors. The compensation ratio K is defined as $K = N_{\mathrm{A}}/N_{\mathrm{D}}$. In the context of this work compensation does not play a significant role and will not be discussed further. However, it is worth noting that a small amount of compensation is likely to occur in any semiconductor.

When the number of impurities N is small enough that their average separation significantly exceeds the effective Bohr radius a_{B} (i.e. $Na_{\mathrm{B}}^3 \ll 1$), the wave function of a localized state decreases exponentially (eq. 3.2) and there is only a small overlap between electronic states belonging to different impurities. No significant interaction of neighboring impurity states is expected and the impurities can be regarded as isolated. In such a situation one speaks of *light doping*. It is important to note that the radius of an electron state near a shallow impurity depends strongly on the kind of semiconductor (κ) and on the band near which the state is located (m_{eff}). Therefore, the range of concentrations corresponding to what is called lightly doped varies from one material to another. With an increasing impurity concentration, the question about how impurity states belonging to different centers influence one another becomes more and more important and effects like level repulsion, Coulomb interaction etc. come into play. In the case of a finite concentration of similar impurities, the single degenerate impurity level is replaced by a distribution of localized energy levels of small but finite width in energy, called an impurity band. However, the term impurity *band* is misleading, because it cannot be considered as a real electronic band, since short and long range order, i.e. translational symmetry, are absent. Thus it cannot be compared to real electronic bands consisting of the eigenenergies of a crystal. The term denotes however the aggregate of energy levels arising due to impurity centers. Bands formed by impurities are no more than half filled, since every impurity contributes (or takes away) one electron and the band is twofold degenerate.

It is useful but difficult to make a clear distinction between light and heavy dop-

ing. A natural, experimental criterion for this is the temperature dependence of the static conductivity at low temperatures. In heavily doped semiconductors, the conductivity is of a metallic type, i.e. the conductivity is constant at low T. In lightly doped semiconductors however it is activated, i.e. it vanishes exponentially, as $T \to 0$. It is reasonable to draw the boundary between light and heavy doping at the impurity concentration N_M at which a non-vanishing conductivity first appears in a weakly compensated semiconductor at zero temperature. This transition is called the metal-insulator transition[2].

3.2 The metal-insulator transition

A fundamental phenomenon studied in semiconductor physics is the transition from an insulating state towards a metallic state with increasing impurity (i.e. acceptor or donor) concentration in a semiconductor host crystal. The metal-insulator transition manifests itself in the temperature dependence of the resistivity. There are several approaches from theory to describe this transition from activated towards metallic behavior. Three different approaches, the models proposed by Mott, Anderson and Lifshitz, shall be sketched briefly in the following. The simplest model would be the assumption of periodically arranged impurities leading to the formation of a real band and conduction within this band would be metallic. However, this is wrong even with given periodicity. The problem is the single electron picture which, though adequate for wide bands of metals, breaks down in the case of a narrow band like an impurity band.

It is well known today that carrier-carrier interactions play a fundamental role in the metal-insulator transition (MIT), as first pointed out by Neville Mott [11]. Mott developed his theory in order to describe the electronic properties of crystalline solids. He therefore considered a periodic arrangement of atoms with a given period b_0 in real space. The model was transferred to the situation of doped semiconductors with the impurity atoms forming a sublattice with a period b_0 much larger than the lattice constant of the host material. The Mott transition arises from electron-electron interactions. The Pauli principle allows two carriers of different spin to be located at the same impurity site, which makes these levels two-fold spin degenerate. However, the two carriers will feel a Coulomb repulsion and one can estimate the interaction energy to $U_0 \approx e^2/a_\mathrm{B}$.

For an infinitely large b_0 this strong Coulomb interaction yields an energy gap separating a low-lying state with one electron per atom and energy E_0 from a second state with two electrons per atom and energy $E_0 + U_0$. For finite b_0 these energy levels broaden into bands (fig. 3.1). The width of these bands depends on the energy overlap integral $I(b_0)$. The number of positions in each branch equals the number of (impurity-)lattice sites. At $T = 0$ the lower band (one electron

[2]Weak compensation is important. When the compensation is strong, the metal-insulator transition occurs at much higher concentrations.

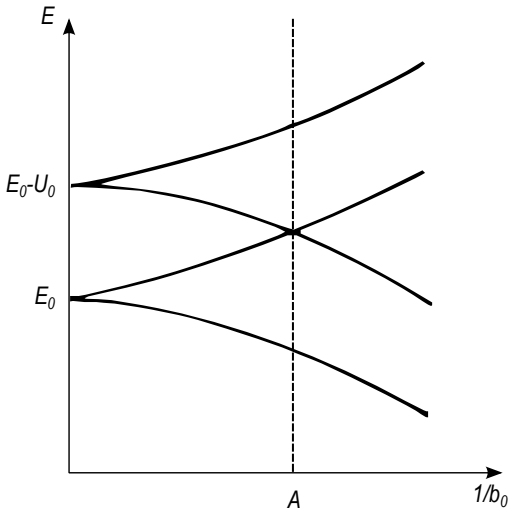

Figure 3.1: Dependence of electron bands on impurity sublattice period b_0. To the left of point A the system is an insulator, to the right a metal. Extracted from [12].

per site) will become filled, whereas the upper band (two electrons per site) remains empty. Thus each site contains only one electron. This does not follow from the Pauli principle (which would allow an occupation by two electrons of opposite spin), but from the Coulomb interaction which is in this case more restrictive. Thus in the case where $|I(b_0)| \ll U_0$, the material is an insulator. With increasing b_0 the gap between the two branches decreases and finally they start to overlap at the point A where a transition towards a metallic state occurs. In other words, the system undergoes the so called Mott transition from a metallic to an insulating state, when U_0 exceeds some threshold. The corresponding localization of the electron wave functions is known as Mott localization. A simple and widely used approach to take these correlation effects into account is the Hubbard model [13]. This extremely simplified model assumes that electrons repel each other only when they are located at the same site. The Hamiltonian is of the form

$$H = \sum_{j\,,\,m\neq 0} I(m)\, a^{+}_{j,\,\sigma} a_{j+m,\,\sigma} + \frac{U_0}{2} \sum_{j\,,\,\sigma} n_{j,\,\sigma} n_{j,\,-\sigma} \tag{3.4}$$

where $a^{+}_{j,\sigma}$ and $a_{j,\sigma}$ are creation and annihilation operators of the state j with spin σ and $n_{j,\sigma} = a^{+}_{j,\sigma} a_{j,\sigma}$ is the occupation number operator. I and U_0 denote the overlap integral and the interaction energy due to Coulomb interaction, respectively. For one dimensional problems, where the Hubbard model admits an exact solution, it is found however, that the gap remains in the spectrum for all $I(b_0)/U_0$, i.e. in 1D the semiconductor is always an insulator. Mott's model defines the term light doping as referring to Hubbards bottom band. This means that low impurity concentrations are given, when the broadening of this band (due to quantum overlap or a fluctuating classical field randomly shifting the levels) can be assumed to be small compared to U_0.

The *Anderson model* uses a different approach. It also assumes a regular lattice, but allows for different electron levels on each site. The energy distribution is assumed to be uniform in an energy interval W. The criterion for localization as formulated by Anderson [14] reads $\lim_{t\to\infty} |\psi_i(t)|^2 > 0$ which expresses that states are regarded as localized, when they do not spread out indefinitely as $t \to \infty$. The important parameter of the model is W/V, where V is the nearest neighbor hopping matrix. Anderson found that for sufficiently large W/V all states are localized. However, there exists a critical value W_C/V where delocalized states start to appear in the middle of the band. With further decreasing W/V the delocalized states region becomes larger, taking over almost the entire band.

The essence of the Anderson transition is the following: One can call two or more sites resonant, if their energies are sufficiently close, i.e. within some energy interval Δ of the order V. The important point is that two resonant sites equally share an electron state, provided the states are nearest neighbors. A simple quantum mechanical analogon is a system of two neighboring quantum wells with similar depth where the probability to find an electron is equally shared between the two wells. One considers two resonant sites as connected, if they are either nearest neighbors or if they are connected via a third resonant site. A conglomerate of connected sites is called a cluster. The important attribute of such a cluster is that the wave functions are nearly constant (in order of magnitude) inside a cluster and negligible outside.

When W/V is large, only small and isolated clusters exist. With decreasing W/V the clusters grow larger and at the critical value W_C/V, an infinite cluster consisting of linked resonant sites arises, which means that the electron wave functions are spread out indefinitely over the infinitely extending paths. At this point the system undergoes the Anderson transition towards a metallic state. The fraction of resonant sites at the transition point is identified with the percolation threshold and the critical value W_C/V can be found using the methods of percolation theory. It can be calculated for specific situations such as special lattice problems or random site problems. Another meaning of the Anderson transition is the following. Consider a band containing both localized and delocalized states separated by a sharp boundary. If one varies the number of electrons in the band, the Fermi level will move with respect to the band and may cross the boundary of the localized states region. The effect is called Anderson transition as well and describes a substantial change in the system's electronic properties.

As in the case of the Hubbard model, the Anderson model predicts total localization in one dimensional systems, i.e. any site fluctuation, however small, turns a one dimensional conductor into an insulator and so does the electron-electron interaction. The same is true for 2D. In the Anderson model one finds that, above the percolation threshold, there is a coexistence of localized and delocalized states. The energy that separates those two is called the mobility edge. The concept of a mobility edge was first introduced by Mott and is of

great importance in the theory of disordered systems and amorphous semiconductors. In some sense the mobility edge plays the role of band boundaries. In disordered systems short-range order is generally preserved which maintains the band picture. However, the boundaries of the density of states are washed out and their tails reach into the forbidden gap. The lower density of states in those tails forces electrons to be localized and the mobility edge serves as a new boundary. If the Fermi energy ε_F lies in a localized region, transport is only possible either via thermal activation into the delocalized states region or via activated hopping between localized states. The latter results in an exponential temperature dependence at low temperatures.

The transition from localized to delocalized states in semiconductors that occurs with increasing impurity concentration, as mentioned above, is best called Mott-Anderson transition, as it comprises features of both idealized theoretical concepts.

As a matter of completeness one should also mention the Lifshitz model. It assumes identical potential wells randomly positioned in space and is therefore in some sense the opposite of the Anderson model. As the levels of different sites are resonant in the sense given above, one would expect metallic conduction. On the other hand, the overlap of wave functions of neighboring sites will lead to a shift of the energy levels. Since every site has a different neighborhood situation, these shifts will be different for each site leading again to the formation of an impurity band. The Anderson model regards the overlap and the dispersion of energy levels as two independent parameters. In that way the Lifshitz model differs essentially from the Anderson picture. Here both overlap and dispersion have the same origin and the same order of magnitude, on average. Because the Lifshitz model does not shed any further light on the metal-insulator transition, it shall not be discussed in more detail here and it shall only be mentioned that this model predicts localization at low impurity concentrations, as well.

3.3 Mechanisms of transport at low temperatures

At high temperatures semiconductors possess an intrinsic electrical conductivity due to thermal activation of carriers across the fundamental band gap E_g. The intrinsic carrier concentration equals

$$n = p = \frac{\left(2\pi\sqrt{m_e m_h}k_\mathrm{B}T\right)^{\frac{3}{2}}}{4\pi^3\hbar^3}\exp\left(-\frac{E_\mathrm{g}}{2k_\mathrm{B}T}\right). \tag{3.5}$$

Because of the large activation energy $E_\mathrm{g}/2$ the intrinsic n decreases very rapidly with decreasing T. At sufficiently low temperatures it becomes smaller than the concentration of carriers in the band states contributed by impurities. This is

the region where the conductivity is entirely determined by the nature and the concentration of impurities (extrinsic region).

There is a temperature range (called saturation range) in which the impurities are ionized and hence the carrier concentration in the band is independent of T. In this range the temperature dependence of the resistivity is entirely determined by the temperature dependence of the mobility μ, which results mainly from a weaker phonon scattering at lower temperatures.

If the temperature is lowered and $k_\mathrm{B}T$ reaches the order of the ionization energy of the impurities E_0, one enters the so called freeze-out region: Here a gradual freezing out of impurity electrons (i.e. deionization or capturing of carriers at impurity sites) takes place. In this region the temperature dependence of the conductivity is due to the rapid decrease of free electron concentration according to

$$n(T) = \sqrt{\frac{N_D\, N_C}{2}}\, \exp\left(-\frac{E_0}{2\, k_\mathrm{B}T}\right) \quad \text{with } N_C = \frac{(2\pi\, m_e\, k_\mathrm{B}T)^{\frac{3}{2}}}{4\,\pi^3\,\hbar^3}. \tag{3.6}$$

Equation 3.6 holds, when $KN_D \ll n(T) \ll N_D$, which makes the range of validity very narrow. This range does not exist unless the compensation is low enough. The temperature dependence of the resistivity shows an activation energy ε_1, i.e. $\rho(T) = \rho_1 e^{\varepsilon_1/k_\mathrm{B}T}$ with $\varepsilon_1 \approx E_0$.

Hopping conductivity

The gradual freezing-out of conduction electrons with decreasing temperature leads to a situation in which the main contribution to the conductivity comes from electrons tunneling directly between impurity sites without involving extended conduction band states. This mechanism is called hopping conductivity. The possibility of hopping conduction was theoretically predicted by Gudden and Schottky [15]. The probability for such a hop, i.e. the transition probability Γ_{ij} between two states i and j, is given by

$$\Gamma_{ij} = \Gamma_{ij}^0 \exp\left(-\frac{2r_{ij}}{a_\mathrm{B}} - \frac{\varepsilon_{ij}}{k_\mathrm{B}T}\right) \tag{3.7}$$

with r_{ij} being the distance between the two impurities, a_B their effective Bohr radius and $\varepsilon_{ij} = \frac{1}{2}\left(|\varepsilon_i - \varepsilon_j| + |\varepsilon_i - \mu| + |\varepsilon_j - \mu|\right)$ the energetic distance between the two states taking into account that hops can only occur from occupied into empty states. The presence of empty positions on donors is a necessary condition which at low T can be fulfilled only by compensation. To overcome any energetic difference between two impurity states, the electron has to absorb and emit phonons, while hopping over impurity sites. This results in an exponential dependence of the resistivity on temperature. The hopping mechanism thus contributes a term of the form $\rho_3^{-1} e^{\varepsilon_3/k_\mathrm{B}T}$ to the overall temperature dependence with $\varepsilon_3 \ll \varepsilon_1$. The ε_3 conduction is usually referred to as *nearest-neighbor hopping*. Within this picture of hopping between neighboring impurity sites, the

activation energy ε_3 is constant and the average hopping length is of the order of the mean separation between impurities and does not vary with temperature.

It is well known that the hopping energy ε_3 depends on the impurity density. At low densities it increases with $N^{1/3}$ [12]. At higher impurity concentrations the overlap of neighboring wave functions becomes more important and tends to decrease ε_3, resulting in a peak of $\varepsilon_3(N)$ at intermediate densities. Thus, except for the limit of low doping, it holds in general that a stronger wave function overlap results in smaller activation energies. For instance, this was shown for different types of impurities in germanium. Larger values of ε_3 were obtained for impurities with larger ionization energy, i.e. smaller average extension of the wavefunction[16–19].

One of the most striking properties of hopping conduction is a very low mobility. The reason is that the electron jump is associated with a weak overlap of the wave functions' tails. Nevertheless it can win in the competition with band transport, because only an exponentially small number of free carriers can participate in the latter at sufficiently low temperatures. Another characteristic feature of hopping conduction is an extremely strong dependence of ρ_3 on the impurity concentration (ρ_3 is determined by an extrapolation of the low-T-part of $\rho\left(T^{-1}\right)$ to $T^{-1} = 0$). The reason is that the probability of a jump between two impurities is determined by the overlap. In the region where the wave functions fall exponentially (average distance much larger than the Bohr radius) the probability (overlap integrals) also falls exponentially with increasing distance. This exponential dependence of the conductivity on impurity concentration is considered as the main experimental evidence for the hopping mechanism of conduction.

Experiments performed by Fritzsche and Cuevas on p-type neutron doped germanium with $K = 0.4$ show clearly the transition between these two transport mechanisms (fig. 3.2): band transport at high T and hopping conductivity at low T.

In general, the temperature dependence of the resistivity in doped semiconductors can usually be parametrized by

$$\rho^{-1}(T) = \rho_1^{-1} e^{\varepsilon_1/k_\mathrm{B}T} + \rho_2^{-1} e^{\varepsilon_2/k_\mathrm{B}T} + \rho_3^{-1} e^{\varepsilon_3/k_\mathrm{B}T}. \tag{3.8}$$

The first term (ε_1-conductivity) is due to band conduction. It is independent of carrier concentration, but depends on the compensation K. It vanishes at low temperatures due to the carrier freeze-out effect. The third term is related to hopping conduction. It arises from the dispersion of impurity levels. At a certain carrier concentration ε_3 vanishes. This concentration corresponds to a transition between activated and the metallic types of conductivity. In addition to band and hopping mechanisms of conduction, there is a third activated mechanism which contributes $\rho_2^{-1} e^{\varepsilon_2/k_\mathrm{B}T}$. It answers the question why the hopping term – "jumping the queue" – is given the number 3, since $\rho_1 \ll \rho_2 \ll \rho_3$ and

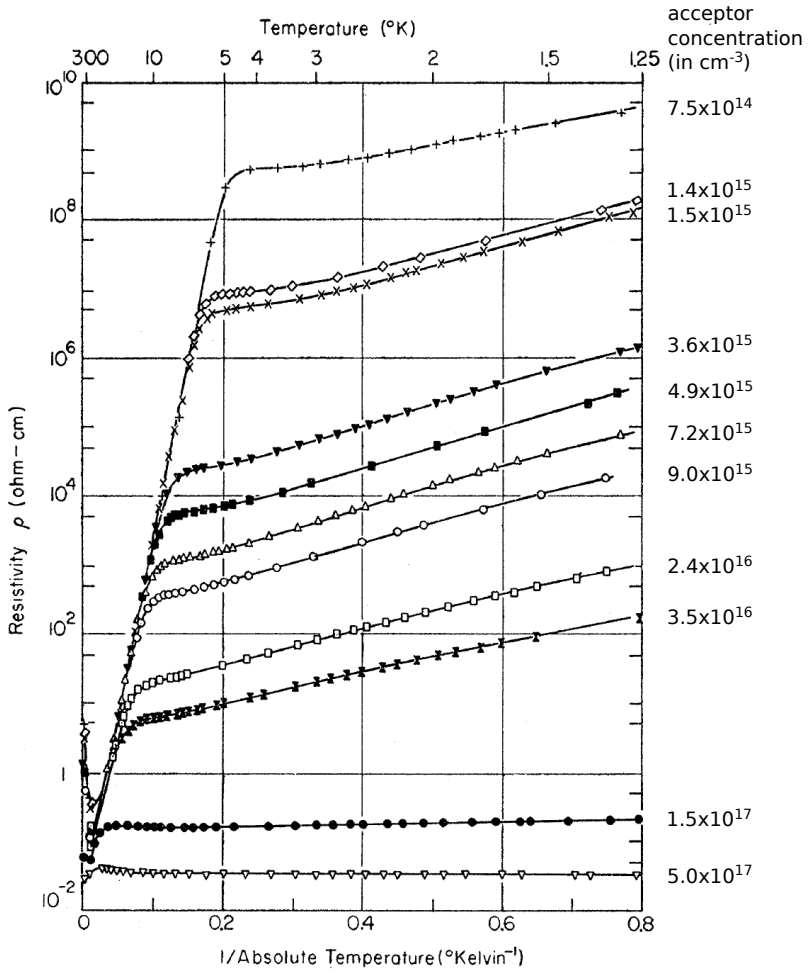

Figure 3.2: Resistivity of compensated p-germanium ($K = 0.4$) [20]. The results clearly show the regions of activated band transport at high T (ε_1-conductivity) and hopping transport (ε_3-conductivity) at low T.

$\varepsilon_1 > \varepsilon_2 > \varepsilon_3$. Therefore, the mechanism works in the intermediate temperature range between band and hopping regimes. It is visible for semiconductors with low compensation ($K \leq 0.2$) and limited to a small range of concentrations near the Mott transition. The mechanism is connected with the motion of electrons over singly filled donors. Neutral donors possess a second electronic state "D^-" with binding energy of order $0.1\,E_0$ [12]. The corresponding large Bohr radius and strong overlap results in a wide band (analogous to upper Hubbard band, however, the presence of disorder is leading to complete or partial localization). The D^--band has higher mobility than hopping conduction over empty states because of the large Bohr radius. Thus, ε_2-conductivity can exceed ε_3 in a narrow range of temperatures. On the other hand: Because of the large width of the D^--band its lower mobility edge can be much closer to ε_F than the bottom of the conduction band, which means that ε_2-conduction can also win the competition with the conduction band (which has a much larger mobility, but substantially

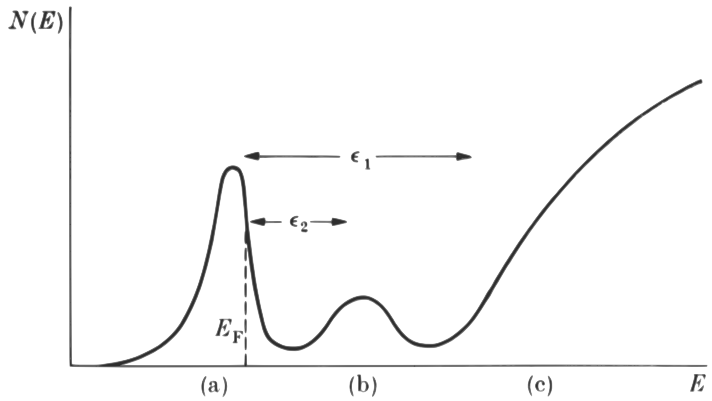

Figure 3.3: The impurity band is split into two subbands: ε_2, range (b) and ε_3, range (a). Range (c) corresponds to conduction band transport. Extracted from [21].

lower electron concentration).

Due to its special properties ε_2-conductivity can only be observed, when first the impurity concentration is high (low n leads to a narrowing of the D^--band and since $\varepsilon_2 \approx \varepsilon_1$, it would not win the competition with band conduction) and secondly the compensation is low (a large concentration of neutral donors is needed). Increasing K improves the conditions for ε_3-transport and worsens those for ε_2-conductivity. If one of those conditions is not fulfilled, the temperature range where ε_2 is more favorable than ε_1 or ε_3 disappears.

Variable range hopping

In a system with localized states near the Fermi level another transport mechanism can take control at low temperature, namely variable range hopping (VRH). Because the hopping probability between two given states depends exponentially on the difference of their energies, it can be concluded that in such a situation only states whose energies lie within a very narrow band around the Fermi level (whose width decreases, as $T \to 0$) will contribute to transport. Because of the narrow width of this band, its constituent states are far away from each other. In other words, the hopping probabilities between neighboring impurities may become smaller than those connecting some remote impurities whose energy levels happen to be very close to the Fermi level. In this case the characteristic hopping length increases with decreasing temperature in contrast to nearest-neighbor hopping (or ε_3 conduction, see above) giving name to the mechanism. In 1968 Mott found that for the temperature dependence of the resistivity, it holds [22]:

$$\rho(T) = \rho_0 \exp\left[\left(\frac{T_0}{T}\right)^{\frac{1}{4}}\right] \tag{3.9}$$

with

$$T_0 = \frac{\beta}{k_\mathrm{B}\, g(\mu)\, a^3}\,, \tag{3.10}$$

which is today referred to as *Mott's law*. T_0 depends on the numerical coefficient β, the density of states at the Fermi level $g(\mu)$ and the localization radius of states near the Fermi level a. Excellent agreement was found for amorphous semiconductors, whereas in crystalline material the exponential factor of 1/4 is replaced by 1/2, which is related to modifications due to the presence of a Coulomb gap, i.e. a diminishing of the density of localized states around the Fermi level, when Coulomb interaction is taken into account. For a sufficiently strongly varying density of states even activated behavior is found, i.e. $\ln(\rho) \propto T^{-1}$ [23, 24].

3.4 Isovalent impurities

Isovalent impurities are defined as substitutional impurities which have the same number of valence electrons as the atoms they replace. In literature, the term *isoelectronic impurity* is widely used as a synonym. However, since the total number of electrons of the atom to be substituted necessarily differs from that of the substitutional impurity, the term *isoelectronic* is misleading. The preceding sections dealt with impurities that had either more or less valence electrons than needed to form crystal bonds which lead to a doping of the host crystal, namely donors and acceptors. Isovalent impurities in contrast are impurities that do not lead to a doping of the semiconductor host crystal.

The simplest way to establish a classification scheme is to distinguish between two kinds of isovalent impurities [25]. The first kind are isovalent impurities that generate localized states and give rise to discrete levels. Typical examples are oxygen in ZnTe, bismuth in GaP or nitrogen in GaP. The second class consists of isovalent impurities that do not produce discrete levels. Instead they generate resonant states which overlap with the band structure and hybridize with the Bloch states. They can exist in a wide range of solubility with the host crystal and lead to a continuous shift of band gap energies as a function of their concentration. The band structure of these alloys can be calculated by assuming the crystal to be perfect except for having an average effective or virtual crystal potential. This approach is known as the *virtual crystal approximation* (VCA). Alloys based on this kind of isovalent impurities seem to be more abundant in nature. Typical examples are Si-Ge, Ga(As,P), or (Ga,In)As.

This simple classification scheme should be regarded as consisting of particularly simple limiting cases, as there exist systems where isovalent impurities might change from first to second kind as a function of concentration or systems for which a clear distinction between the two kinds is not straightforward. In the following, only the first kind of isovalent impurities forming localized

states shall be considered. These have become known as isovalent or isoelectronic traps.

A model that has been very successful in explaining the experimental results made on isovalent traps has been proposed by Hopfield and Thomas [26]. It assumes that an isovalent trap can be attractive either for electrons or holes. Since there is no net charge involved, the binding will not be due to Coulomb forces, but to forces of very short range. Therefore, it is impossible to treat this bound state within an effective mass approximation and the states have to be distinguished from shallow states as discussed in the preceding sections. After an isovalent trap has captured an electron or a hole, this trap is negatively or positively charged and by long range Coulomb interaction it will capture a carrier of opposite charge. This leads to an exciton bound to the isovalent trap. If the carriers attracted to the isovalent trap are bound strongly enough, the wave function of the second carrier bound by Coulomb interaction will be acceptor-like for an electron trap or donor-like for a hole trap. Since the spins of electron and hole can be oriented either in parallel or anti-parallel, the angular momentum of the exciton state can be either $J = 1$ of $J = 2$, respectively.

Experimental evidence for the model was given mainly from emission and absorption spectra. As an example, fig. 3.4 shows data for ZnTe:O where very sharp emission lines are visible on the high energy side (labeled as A and B). They are related to the exciton bound to the isovalent impurity. At higher temperatures, only the optically allowed transition from $J = 1$ to the crystal ground state ($J = 0$) can be observed. At low temperatures, the optically "forbidden" transition from the $J = 2$ state is visible due to thermal depopulation of the energetically higher $J = 1$ state. In either case a series of LO_Γ phonon replica are observed. The dashed lines (A' and B') are replica due to acoustical phonons.

Besides the very typical optical emission and absorption spectra, modifications of the transport behavior related to isovalent traps have been observed. Isovalent traps give rise to an additional scattering of free carriers, which manifests itself in a reduction of the mobility as reported for instance in the case of GaP:N [27] or Ga(N,As) [28, 29].

In order to give a more quantitative description of the binding at the isovalent trap, the interaction between charge carriers and impurities was assumed as being due to a potential derived as the difference between the pseudopotentials for the substituted and substitutional atoms. This approach was quite successful, especially when a relaxation of the lattices was allowed [30, 31].

However, there exists a much simpler phenomenological approach proposed by Aten [32] that uses the electronegativity as the quantity to describe the strength of the short range binding force of isovalent impurities. The difference in electronegativity between the atom to be substituted and the substitutional impurity Δx determines its character. According to reference [25], the impurity

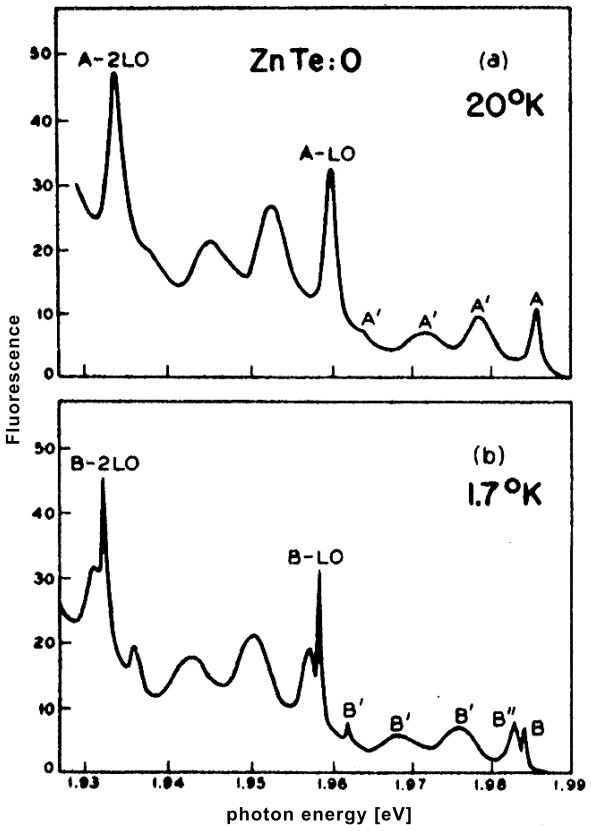

Figure 3.4: Emission spectra of ZnO:Te with phonon replica of the A-line (at 20 K) and of the B-line (at 1.7 K). From [26].

will form an isovalent electron trap, if $\Delta x \leq -1.01$, and it will form a hole trap, if $\Delta x \geq +0.39$. For Δx in between these limits, no isovalent trap, but an isovalent impurity of the second kind (see above) is expected. Although the electronegativity is a rather poorly defined quantity, the concept of electronegativity in connection with isovalent traps appears to be quite successful, as it gives heuristic rules or guide-lines to determine the character of a given isovalent impurity. Another aspect that determines the character of an impurity is strain. Large differences in the atomic radius between the substituted and the substitutional impurity may also result in significant perturbations of the electronic structure advancing the conditions for the formation of isovalent traps. As a final remark, it is interesting and surprising that so far isovalent traps were found only through substitution on anion sites. However, a general reason for this behavior is not known to date.

4 Influence of localized isovalent impurity states on the conduction band structure of (Ga,In)As

The properties and electronic structure of many conventional semiconductor alloy systems such as (Al,Ga)As or (Ga,In)As can be well described using the so called virtual-crystal approximation (VCA). Within the VCA approach, different atoms on the same sublattice are replaced by virtual atoms whose properties are an average of the original ones. As mentioned in section 3.4, these alloys are created by substitution with isovalent impurities that are similar in electronegativity and atomic size compared to the substituted atoms. Thus, those impurities do not represent a strong perturbation and generate resonant states that hybridize with the Bloch states of the original host crystal. For example, the properties (e.g. density, lattice constant, effective mass, etc.) of the alloy $Ga_{1-x}In_xAs$ can be found with good accuracy by a linear interpolation between $0 \leq x \leq 1$, i.e. between GaAs and InAs.

On the other hand, there exist semiconductor alloys that can be regarded as being extreme in the sense that the virtual-crystal approximation totally fails. An example would be the substitution of the group V element in III-V compounds with small amounts of nitrogen which leads to dramatic changes of the electronic properties. The most prominent examples that have been studied extensively in the recent past are Ga(N,As) and (Ga,In)(N,As). These alloys will be briefly discussed at the beginning of the following section in order to motivate the interest in (B,Ga)As and (B,Ga,In)As where cationic substitution by the isovalent impurity boron is studied. As mentioned in section 3.4, so far no isovalent traps have been found by substitution on cation sites. However, as it will be shown, both theoretical and experimental results indicate that boron indeed forms highly localized states, which is a main property of isovalent traps. Consequently it might be regarded as the first isovalent trap substituted on cation site.

4.1 Isovalent impurity nitrogen in GaAs

The semiconductor alloys (Ga,N)As and (Ga,In)(N,As) attracted much attention, because they show very unusual electronic properties that contradict the

predictions of the virtual-crystal approximation. Most famous is the observed extremely strong redshift of the fundamental energy gap with increasing nitrogen fraction [33, 34]. Similarly puzzling from the VCA point of view are the considerable and nonmonotonic enhancement of the electron effective mass [35, 36] and the nonmonotonic changes of the gyromagnetic factor [37] with increasing nitrogen content. Both are well understood today and can be attributed to the influence of nitrogen related localized states in the vincinity of the conduction band edge (CBE) [38].

Besides interesting fundamental questions, these alloys are of particular interest for device applications. Since the fundamental band gap can be varied within a wide range of energies by changing the nitrogen concentration, whereas simultaneously the internal strain can be adjusted by additionally incorporating In in group III sites, (Ga,In)(N,As) alloys offer promising possibilities for optoelectronics on GaAs basis. For example, they are used as active medium in vertical cavity surface emitting lasers (VCSELs) for telecommunication wavelength of 1.3 or 1.5 μm (already commercially available). Because N and In concentrations can also be adjusted to obtain lattice matching to the GaAs substrates, this alloy was also regarded as a promising candidate for a 1 eV material in multilayer solar cells for space applications [39]. Another application concept exploits the fact of low electron mobilities and proposes (Ga,In)(N,As) as an absorber medium in highly efficient avalanche photo-diodes [40].

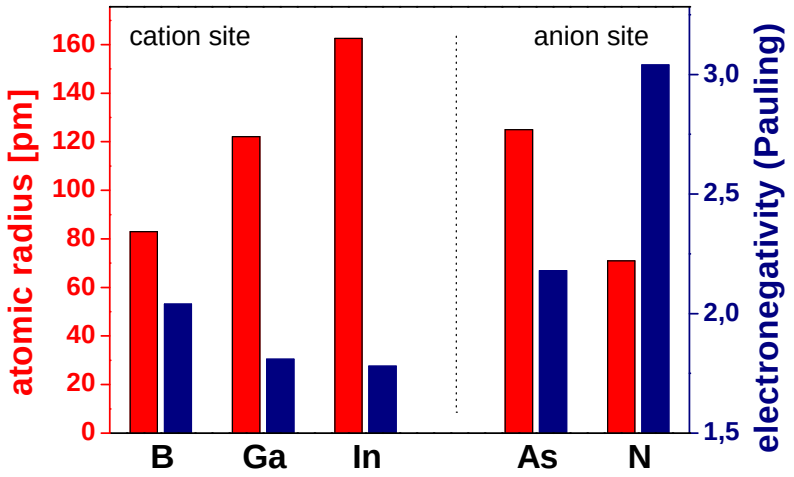

Figure 4.1: Comparison of electronegativity and atomic radius for the chemical elements under discussion [41].

Because nitrogen is an isovalent impurity in GaAs, the remarks of section 3.4 are relevant. Accordingly, the underlying reason for the unusual behavior can be found by comparing the electronegativity and atomic radius of nitrogen and arsenic atoms, which is shown in fig. 4.1. It is obvious that nitrogen differs considerably in both quantities from the arsenic atoms. These well pronounced differences result in a very strong perturbation of the electronic structure of the host crystal.

It is known today that nitrogen forms highly localized electronic states that are resonant with the conduction band about 1.7 to 1.8 eV above the valence band edge of GaAs [42, 43]. With raising the nitrogen content up to a few percent, states attributed to nitrogen pairs and higher nitrogen clusters gain in importance. In fact, the total distribution of nitrogen related states stretches out considerably within the conduction band as depicted in fig. 4.2. Their appearance in the bandgap of GaAs:N was shown for [N] $\approx 10^{17}\,\mathrm{cm}^{-3}$, using hydrostatic pressure [44]. The unusual band structure changes in this non-amalgamation type semiconductor alloy arise from the interplay of those N-related localized states with the extended conduction band states of the host [45–48].

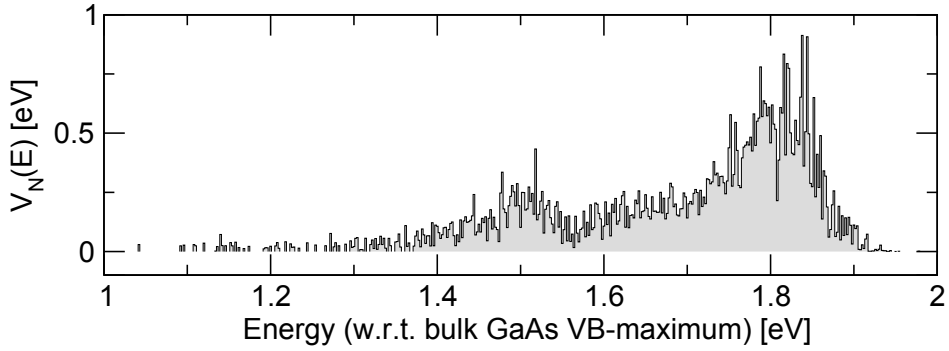

Figure 4.2: Distribution of nitrogen relates states with respect to the bulk GaAs valence band maximum calculated for $Ga_{0.920}In_{0.080}N_{0.037}As_{0.963}$. The conduction band edge of this alloy lies at 1.0 eV. Calculations performed by A. Lindsay [49].

Transport experiments on n-type (Ga,In)(N,As) exhibit striking similarities with strongly disordered systems, whereas p-type samples behave like conventional semiconductor alloys. The nitrogen pair states were found to lie in the vicinity and slightly above the conduction band edge (see fig. 4.2) and have been identified as the main reason for the strong reduction of electron mobility in these systems [28, 29]. An important point in this context is the considerably enhanced cross section for elastic scattering by nitrogen impurities.

Besides the reduction of the mobility, this strong elastic scattering is responsible for enhanced weak Anderson localization effects observed in (Ga,In)(N,As) samples [50–52] which are usually regarded as evidence for the presence of enhanced disorder. These become manifest in strong negative magnetoresistance (MR) effects as depicted in fig. 4.3 exemplarily for one $Ga_{0.950}In_{0.050}N_{0.016}As_{0.984}$:Si sample with free carrier concentration of $n = 1.0\times10^{18}\,\mathrm{cm}^{-3}$.

In conclusion, nitrogen strongly disturbs the conduction band structure, leading to numerous unexpected effects that cannot be explained within the virtual-crystal approximation. The existence of strongly localized states related to nitrogen has to be taken into account in order to properly explain the electronic behavior of these alloys. With the knowledge about the enormous impact of isovalent nitrogen on the properties of conventional GaAs, the question about

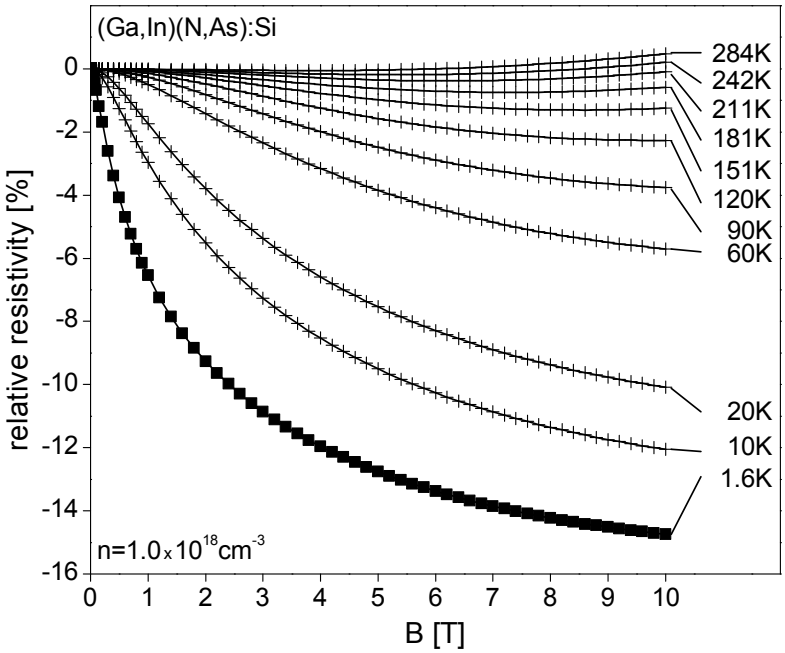

Figure 4.3: Enhanced weak Anderson localization effects of the magnetoresistance of n-type $Ga_{0.950}In_{0.050}N_{0.016}As_{0.984}$:Si.

the influence of other isovalent impurities arises. The rest of this chapter will deal with the isovalent impurity boron in GaAs or (Ga,In)As which in contrast to nitrogen is substituted on the cationic sublattice. Whereas (Ga,N)As and (Ga,In)(N,As) have been, and still are, extensively studied, only little is known about the boron containing alloys up to now.

4.2 Isovalent impurity boron in GaAs

The semiconductor alloys (B,Ga)As and (B,Ga,In)As fill the gap between conventional and extreme semiconductor alloys in the sense given in the introduction of this chapter. From fig. 4.1, it can be seen that boron differs strongly from the gallium and indium atoms it substitutes on the cationic sublattice, however, the differences are not as pronounced as in the case of nitrogen. From this simple point of view it can already be expected that the incorporation of boron into GaAs or (Ga,In)As might result in unconventional behavior, although not as dramatic as in the case of nitrogen – an expectation which was also encouraged by theory [45, 53]. Indeed, as it will be shown in the following, some aspects of these alloys can be regarded as conventional behavior, whereas in other situations extreme and unexpected facets appear.

Speaking in favor of a conventional semiconductor, only a weak influence of boron incorporation on the fundamental band gap was found. Shan et al. ob-

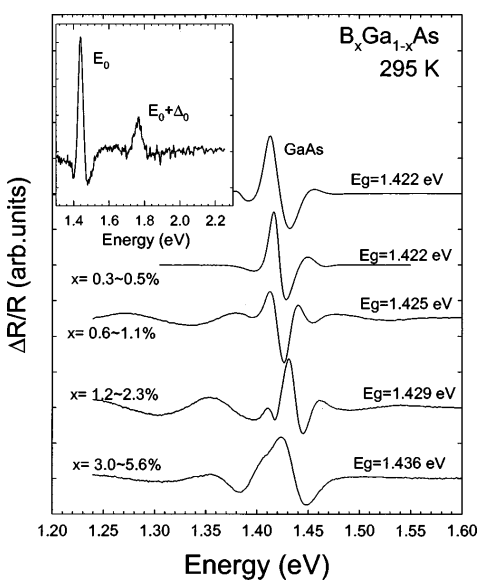

Figure 4.4: PR spectra taken with several $B_xGa_{1-x}As$ samples at 295 K. The inset is a PR-spectrum taken over a wide energy range from 1.3 to 2.35 eV for a sample with a boron concentration of 3–5.6%. Extracted from [54].

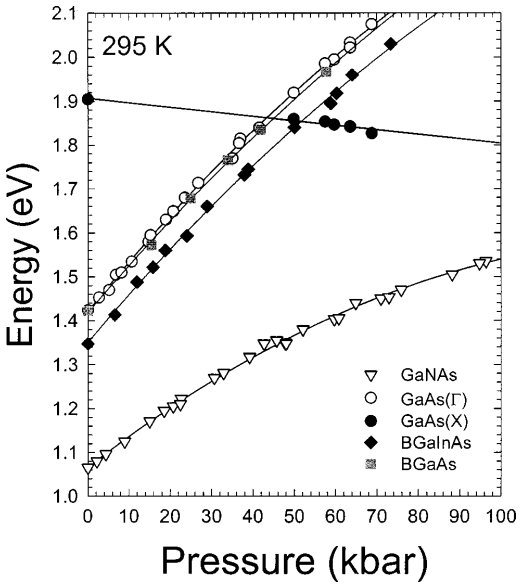

Figure 4.5: The energy of optical transitions associated with the direct band gaps of (B,Ga)As and (B,Ga,In)As samples as a function of pressure. The results from a $Ga_{0.97}N_{0.03}As$ sample are also plotted for comparison. Extracted from [54].

tained photoreflectance (PR) spectra from $B_xGa_{1-x}As$ samples with varying composition x and studied the pressure dependence of the observed signals [54]. The results from Shan's work are presented in figures 4.4 and 4.5. It can be seen (fig. 4.4) that to a first approximation the fundamental band gap is not affected by an increasing boron content. From the PR-measurements under hydrostatic pressure (fig. 4.5), it was found that the variation of the bandgap of (B,Ga)As does not show the unusual behavior as for Ga(N,As). Instead it shifts parallel to that of GaAs. The slightly lower E_g in the case of the (B,Ga,In)As sample is due to In incorporation. These experiments confirmed the theoretical predictions given by Szwacki et al. [55] who explained the much weaker influence of localized boron states on extended conduction band states (compared to N) as being due to symmetry reasons that stem from the different substitution sites of B and N. These experimental and theoretical findings suggested that the influence of boron on the conduction band structure is much weaker than in the case of nitrogen.

On the other hand, Hofmann et al. reported a strong increase of the electron effective mass [56]. They used far-infrared magneto-optic ellipsometry to determine the effective mass and observed an 44% increase in m_{eff} over that expected for $In_{0.06}Ga_{0.94}As$. This is considerably larger than the predicted value using the virtual-crystal approximation and a further increase in mass was measured with increasing carrier concentration.

Lindsay et al. performed full tight binding calculations [47] to study the conduction band structure. They used an accurate sp^3s^* nearest-neighbor tight-binding approach to investigate the electronic structure of different alloys. The calculations were undertaken on 1000-atom supercells in which all atomic positions have been allowed to relax and the interatomic parameters were allowed to vary with bond length, while the magnitude of the on-site parameters depended explicitly on the overall neighbor environment. In this GaAs supercell 13 Ga atoms were replaced by B atoms, giving an alloy composition of $x = 2.6\%$. Figure 4.6 presents the results they obtained for 3 different situations.

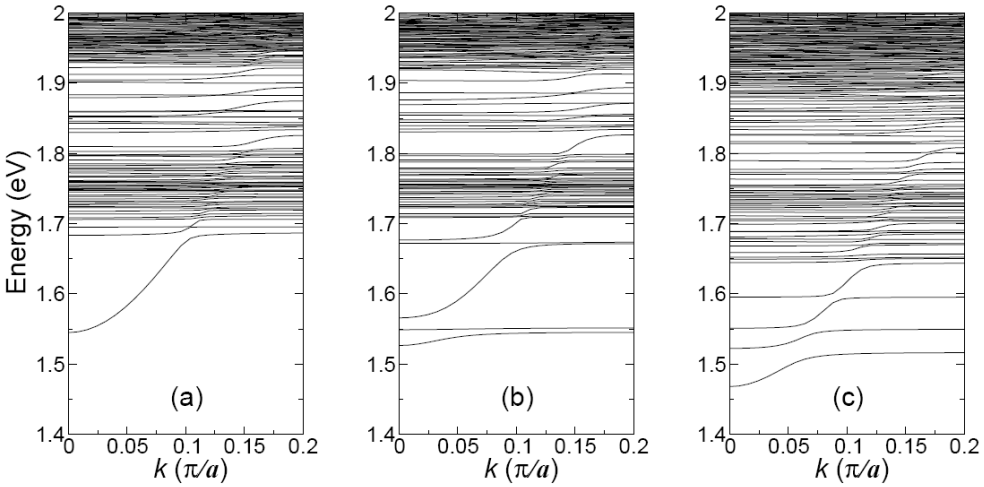

Figure 4.6: Results of the tight bindung calculation by Lindsay et al. [47]. Calculated band structure of a $B_{13}Ga_{487}As_{500}$ supercell (2.6% B alloy) containing (a) 13 isolated B atoms, (b) nine isolated B atoms and two B-B pairs, and (c) the alloy $B_{13}In_{30}Ga_{457}As_{500}$ with nine isolated B atoms, two B-B pairs, and 30 randomly distributed In atoms replacing Ga. The band dispersion is calculated along the k_z direction in units of π/a, where a is the appropriate alloy lattice constant.

At first glance, in a situation where only isolated boron atoms are considered (fig. 4.6 a), the results seem to resemble normal VCA behavior, showing a small blueshift of the band gap (which is consistent with experiments) and an effective mass close to that predicted by the virtual-crystal approximation (in contrast to experiment). However, the incorporation of boron introduces a large number of B-related defect states above the conduction band edge between 1.7 and 1.8 eV (with respect to the valence band edge) that are associated with highly localized B states of T_d-type symmetry. Above, there is a further group of highly localized B states of A_1 symmetry. But since T_d-states do not interact with the conduction band edge for symmetry reasons and A_1 levels have a much weaker interaction and effect in (B,Ga)As compared to Ga(N,As) due to the different host state character of the A_1 states [57], no significant perturbation on account of boron incorporation is found. But the assumption of isolated boron atoms is not realistic. At the composition of $x = 2.6\%$, the formation of B-B pairs is quite likely and has to be taken into account, which is done in the calculations shown in fig. 4.6 b. Here the supercell contained two B-B pairs and nine isolated B-atoms.

This has dramatic effects near the conduction band minimum, introducing two new levels associated with the two B-B pairs which lie just above the conduction band edge. These states have a small interaction through which they strongly hybridize with the conduction band edge at Γ, an effect which more than doubles the calculated band edge effective mass. This increase is in good agreement with experiment. The additional incorporation of In moves the band edge away from the pair levels and figure 4.6 c finally depicts the results for a $B_{13}In_{30}Ga_{457}As_{500}$ supercell. Basically, one observes a strong recovery in the dispersion near the conduction band minimum. According to Lindsay et al., a shift of the band edge down by around 50 meV reduces the effect of these levels on the band edge mass by more than a factor of 2. But still the calculated m_{eff} is around 30% larger than the VCA value for this alloy, which is comparable with the 44% increase obtained for the $B_{0.027}In_{0.06}Ga_{0.913}As$ alloy studied by Hofmann et al. [56].

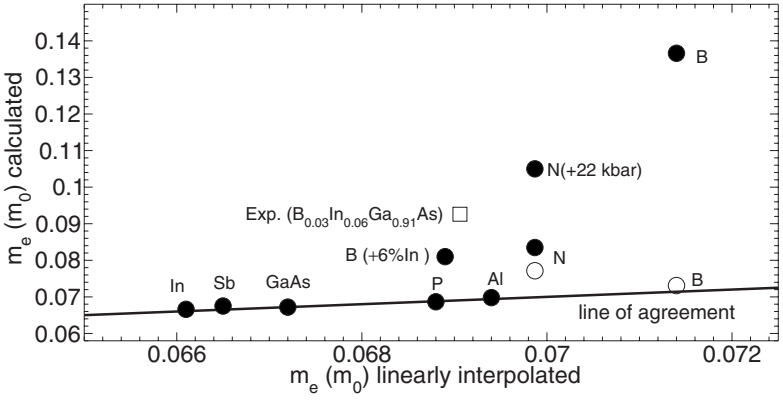

Figure 4.7: Calculated effective masses of different $X_xGa_{1-x}As$ and GaY_xAs_{1-x} alloys (X = B, Al, In and Y = N, P, Sb) as extracted from [47].

Figure 4.7 summarizes the results for the calculated effective masses obtained from the tight binding calculations. The diagram compares the calculated values to those obtained by a linear interpolation according to the virtual-crystal approximation. The solid line shown in fig. 4.7 therefore renders the diagonal or 'line of agreement' between the calculations and the virtual-crystal approximation. Additionally to B and N, the authors included calculations for a variety of other $X_xGa_{1-x}As$ and GaY_xAs_{1-x} (X = Al, In and Y = P, Sb) alloys, as well. The model is able to correctly reflect VCA behavior for these conventional alloys, which further increases the confidence in the calculations. Open symbols represent situations where only isolated impurities were considered, while full symbols display supercells including pairs of impurities. Whereas in the case of X = Al, In and Y = P, Sb this does not make any difference (the symbols cannot be distinguished in fig. 4.7), the effect is dramatic for Ga(N,As) and (B,Ga)As as described above.

In order to conclude, one can say that (B,Ga)As and (B,Ga,In)As indeed show an intermediate behavior, somewhere between the conventional behavior of,

i.e. (Ga,In)As, and the extreme non-amalgamation behavior of Ga(N,As). Most important in the context of this work is that the incorporation of boron does not only strongly increase the effective mass, but introduces a number of highly localized electronic states just above the conduction band edge. This indicates that modifications of the electronic transport are to be expected. In the following the influence of boron incorporation on the electronic transport properties of n-type (B,Ga,In)As-layers will be studied.

4.3 Influence of localized isovalent centers on the metal-insulator transition

As mentioned in the previous section, the influence of isovalent nitrogen and boron are mainly restricted to a perturbation of the conduction band of their GaAs-based host crystals. This is reflected in the transport measurements on p-type (Ga,In)(N,As) and (B,Ga,In)As, as shown in fig. 4.8. The two samples represent a whole variety of p-type samples with different carrier concentrations which all show qualitatively similar behavior. The relative magnetoresistance[1] curves show a quadratic dependence on the applied magnetic field as expected from standard Boltzmann transport theory (see e.g. [58, 59]). Especially no negative magnetoresistance is found even at the lowest temperatures.

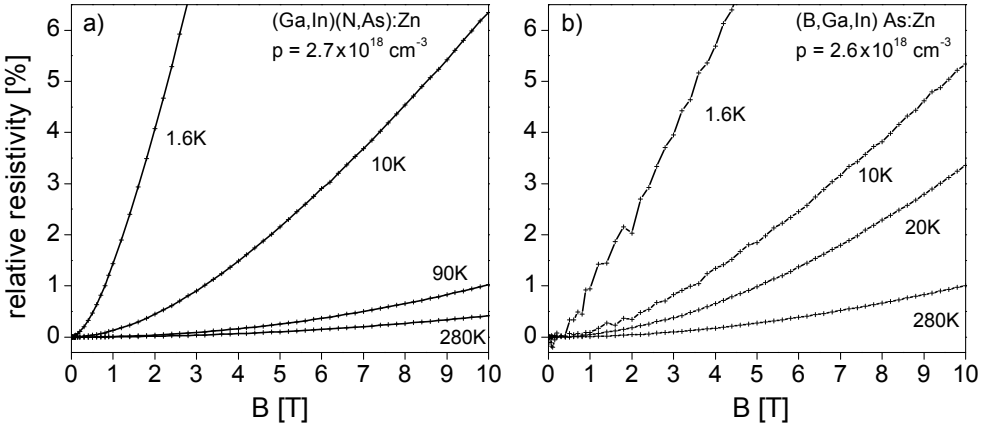

Figure 4.8: Magnetoresistance measurements of p-(Ga,In)(N,As) and p-(B,Ga,In)As for various temperatures. The curves resemble normal quadratic behavior.

The following discussion will therefore be restricted to three n-type (B,Ga,In)As epitaxial layers with boron and indium contents of 2.7% and 6.0%, respectively. They were grown by metal-organic vapor-phase epitaxy (MOVPE) and the indium concentration was chosen to obtain lattice matching on (100) GaAs substrates [60]. All samples are n-type doped with Si, but vary in Si-dopant con-

[1] The relative magnetoresistance is defined as $\frac{\rho(B)-\rho(0)}{\rho(0)}$.

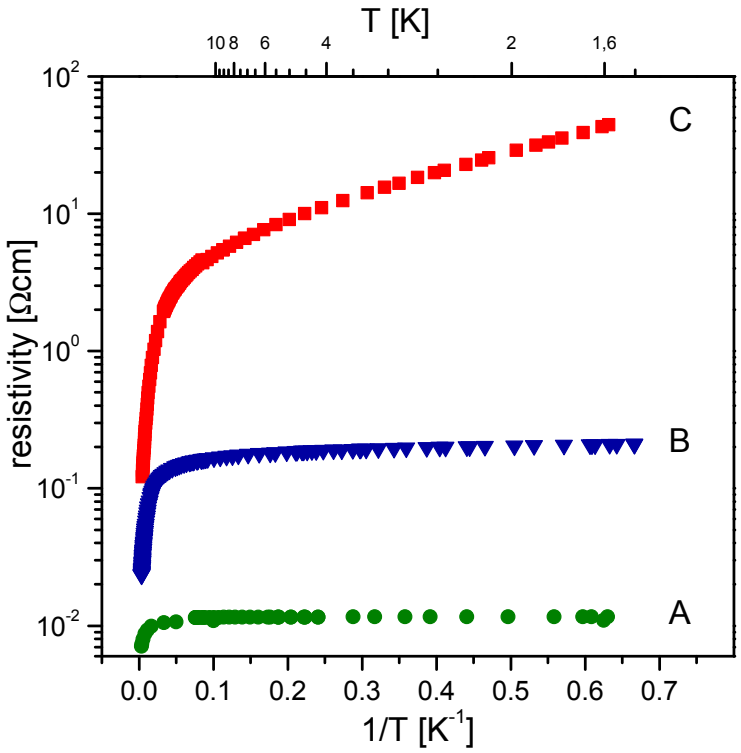

Figure 4.9: Temperature dependence of the resistivity. The three samples show a transition from metallic towards activated behavior.

centration. The free carrier concentration, determined by Hall measurements, ranges from $4.0 \times 10^{16}\,\mathrm{cm}^{-3}$ to $7.2 \times 10^{17}\,\mathrm{cm}^{-3}$ at room temperature. Sample characteristics are summarized in table 4.1.

Figure 4.9 depicts the temperature dependence of the resistivity for all three samples. Sample A, having the highest carrier concentration, shows metallic behavior with a constant resistivity at low temperatures. With decreasing doping concentration, an activated transport behavior at low T is found which is reflected in a linear dependence of the logarithm of the resistivity on the reciprocal temperature, as described in section 3.3. The corresponding activation energies ε_3 were extracted from a fit in the range from 1.6 K to 4 K and have values of 0.017 meV and 0.31 meV for sample B and C, respectively. The linear dependence

Nr.	$n(280\,\mathrm{K})[\mathrm{cm}^{-3}]$	$\mu(280\,\mathrm{K})[\mathrm{cm}^2/\mathrm{Vs}]$
A	7.2×10^{17}	1160
B	1.2×10^{17}	1719
C	4.0×10^{16}	2193

Table 4.1: Summary of sample properties. Free carrier concentration and mobility as determined by Hall measurements.

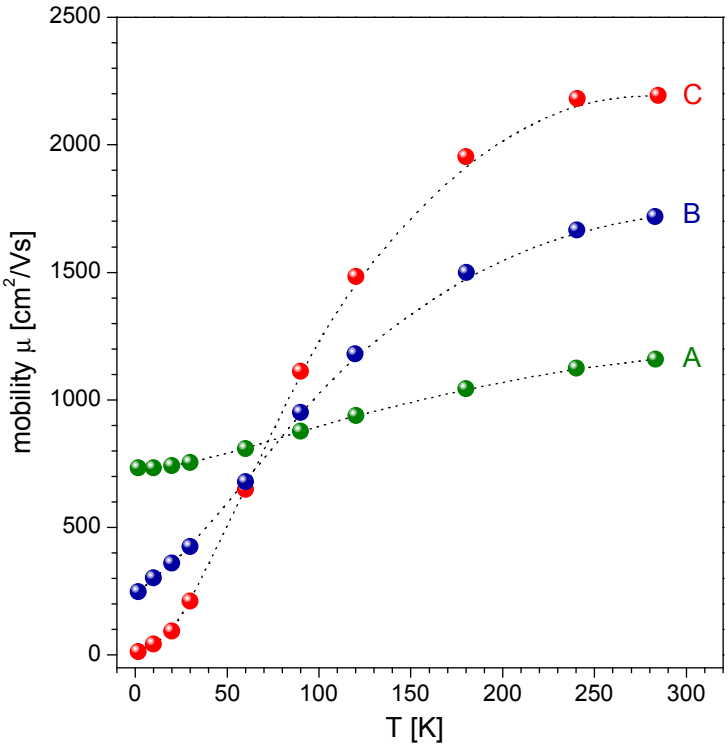

Figure 4.10: Temperature dependence of the Hall mobility.

in the Arrhenius plot can be interpreted as evidence for nearest neighbor hopping [4]. However, for a density of states that varies sufficiently strongly, variable range hopping cannot be excluded [23, 24].

The temperature dependence of the Hall-mobility reflects the overall picture deduced from the conductivity measurements. The measurements were carried out in a low field of 1 T. As can be seen from figure 4.10, samples A and B show only a weak variation of the mobility with temperature and quite high values of the mobility at low T. This indicates a metallic behavior. Sample C, however, shows the highest mobility at room temperature and by far the lowest mobility at low temperature where values fall below $10\,\mathrm{cm}^2/\mathrm{Vs}$, reaching the limit of reliable mobility determination by Hall measurements in van der Pauw geometry. Thus from the point of view of mobility measurements, sample C differs from the other two, as it cannot be considered as metallic – however, conduction in an impurity band or nearest neighbor hopping seems likely.

While the temperature dependence of the resistivity and mobility provide useful hints about the transport mechanism, the most valuable information can be extracted from magnetotransport measurements. In order to provide a reference, fig. 4.11 displays relative magnetoresistance curves of an n-type GaAs sample with $n = 2 \times 10^{18}\,\mathrm{cm}^{-3}$ for $T = 1.6\,\mathrm{K}$ and $T = 285\,\mathrm{K}$. At both temperatures a quadratic dependence of the resistivity on the applied magnetic field is found. In n-GaAs the positive magnetoresistance at 10 T is usually of the order of 100%.

At low temperatures the onset of Shubnikov-de-Haas oscillations is observed. Additionally, a very small negative magnetoresistance of -0.5% is found that can be explained in the framework of weak Anderson localization [61] which is a quantum mechanical correction of the conductivity. In a system with enhanced elastic scattering mechanisms (e.g. caused by disorder), quantum interference of different scattering paths leads to an enhanced probability for elastic backscattering of electrons as compared to other scattering directions and increases the resistivity at zero field. An applied magnetic field destroys this interference and decreases the resistivity resulting in negative magnetoresistance effects. This mechanism scales with the amount of energetic disorder at the Fermi level and the effectiveness of elastic scattering processes.

The relative magnetoresistivity curves for (B,Ga,In)As are shown in fig. 4.12 for various temperatures. At the highest doping level (sample A), the measurements show typical band transport behavior, i.e. a small negative contribution to the magnetoresistance at low temperatures (up to -3% at 1.6 K) and a normal positive contribution leading to a small positive magnetoresistance of 2% at 10 T for $T = 1.6$ K. At the lowest temperatures, an onset of Shubnikov-de-Haas oscillations can be seen. The negative magnetoresistance in this sample can be easily interpreted in the framework of weak Anderson localization, considering the situation of slightly disturbed band transport [51]. The negative magnetoresistance effect decreases with increasing temperature and vanishes at about 90 K.

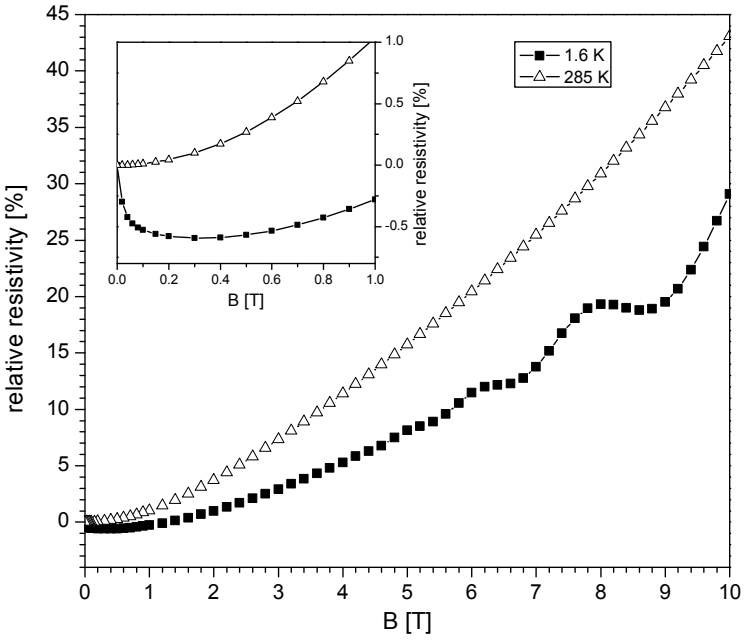

Figure 4.11: Magnetoresistivity curves of n-GaAs ($n = 2 \times 10^{18}\,\mathrm{cm}^{-3}$) at 1.6 K and 285 K. The inset magnifies the low field region where a small negative magnetoresistance is observed at low temperatures.

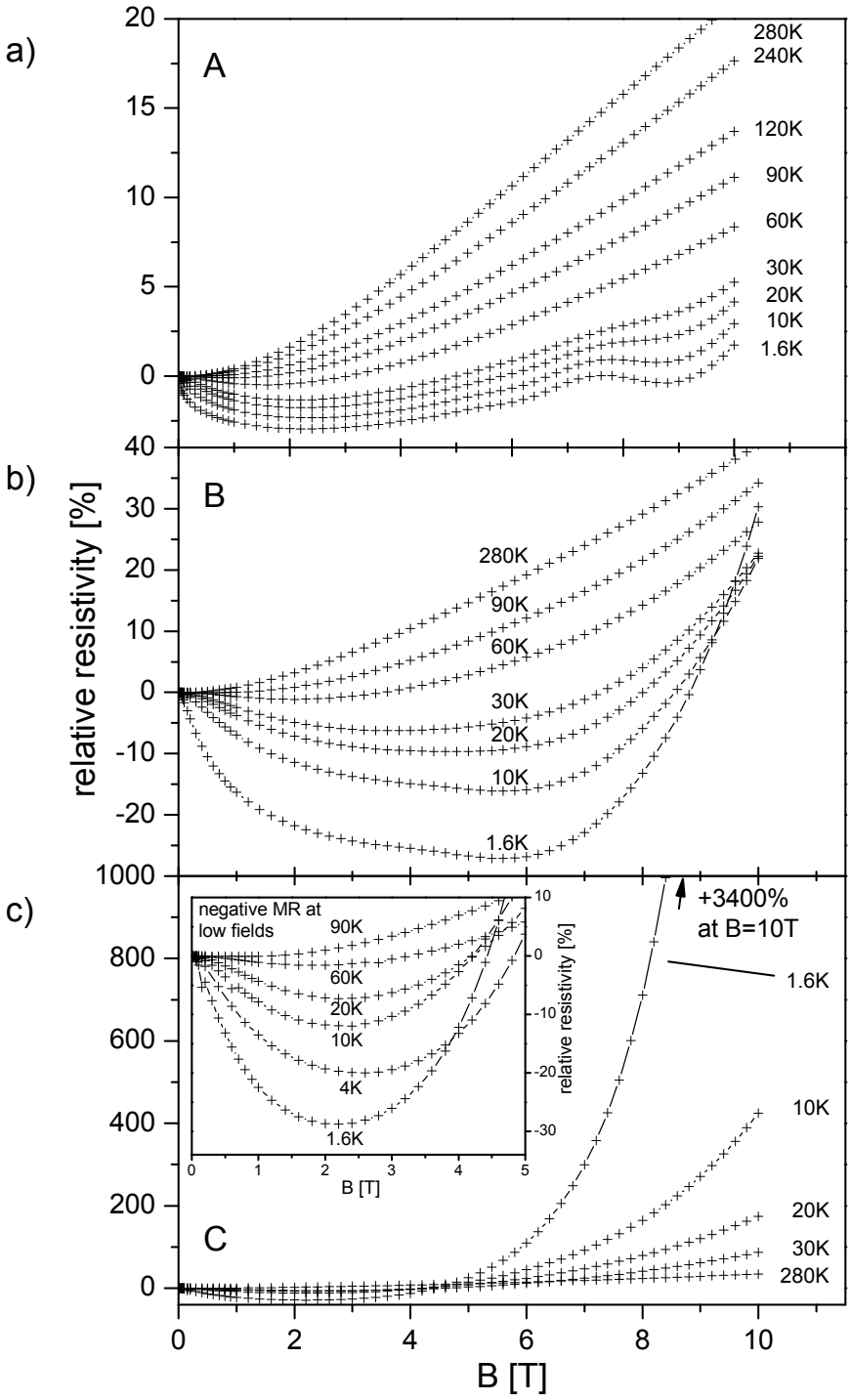

Figure 4.12: Relative magnetoresistivity curves at various temperatures. The size of the magnetoresistance effects and hence the scales of the individual figures vary strongly for the different samples. The measurements are interpreted as a transition from band-like transport towards hopping-like transport with decreasing doping concentration.

The observation of weak Anderson localization corresponds well to the metallic temperature dependence of the resistivity (fig. 4.9). Lowering the doping concentration creates two crucial changes of the magnetotransport behavior at low temperature that can be well observed in sample B and dominate in sample C. These effects are, first, an increase of the negative contribution at lower magnetic fields and secondly an additional strong positive contribution at higher fields. For sample B this means a negative magnetoresistance of up to -27% at 5.6 T which is ten times larger than the negative magnetoresistance in sample A. The positive contribution starts to dominate at fields above 6 T leading to a relative magnetoresistance of 30% at the highest value of the magnetic field. Furthermore, one finds a subtle structure in the magnetoresistance curve at the lowest temperature, more precisely a weak "hump" at 4 T. At even lower doping concentration (sample C), both effects become even more pronounced. While one can still observe a large negative magnetoresistance of -29% at low field, the positive contribution starts to control the magnetoresistance above 3 T and the crossing towards positive magnetoresistance takes place at 4.5 T. At higher fields, this contribution gains extraordinary strength, leading to a very large positive magnetoresistance of 3400% at 10 T. At fields above 6 T the resistivity increases exponentially with magnetic field. In all samples, both negative and positive effects undergo a rapid decrease with increasing temperature, as depicted in fig. 4.12. Obviously, the lower doped samples B and C differ strongly from the metallic sample A. The exponential increase of the resistivity at higher magnetic fields is the most important hint towards a change of transport mechanism at the doping concentrations considered.

The wavefunction shrinkage effect

A gigantic positive magnetoresistance which depends exponentially on the applied magnetic field has been observed in a variety of different materials and for different impurity atoms [62–76].

It is well known that in the presence of a strong magnetic field, the wave functions of impurity electrons do not preserve their spherical symmetry, but are squeezed in the transverse direction, becoming cigar-shaped [77–79]. For weak fields, the magnetic forces are not comparable to the Coulomb forces and have no effect on the wave function describing the state. With increasing magnetic field strength, as the hydrogen-like donor wavefunction elongates, it shrinks in all dimensions, thus there is a steady increase in the magnitude of the Coulomb energy.

As a consequence, the ionization energy becomes larger. In the high field case, determined by $H \gg H_{\text{C, freeze-out}}$ with [79]

$$H_{\text{C, freeze-out}} = 2\,T \times 10^5 \left(\frac{m^*}{m_0 \epsilon_\infty}\right)^2, \tag{4.1}$$

where ϵ_∞ is the high frequency dielectric constant, the ionization energy is a function of the magnetic field and increases with increasing field strength. In

the present case, i.e. with $m^*/m_0 \approx 0.1$ and $\epsilon_\infty \approx 12.2$ (using the value for $Ga_{0.94}In_{0.06}As$), this value can be estimated to be $H_{C,\,\text{freeze-out}} \approx 13\,\text{T}$. Thus, the high field case is not accessible with the experimental setup used here. A particular increase of the ionization energy which would decrease the number of ionized carriers in the conduction band, the so called magnetic freeze-out effect, cannot explain the dramatic increase of the resistivity alone. Furthermore, the effect of an increasing ionization energy is relevant for electrons thermally activated into the conduction band (band transport) and of minor importance for the hopping mechanism of conduction.

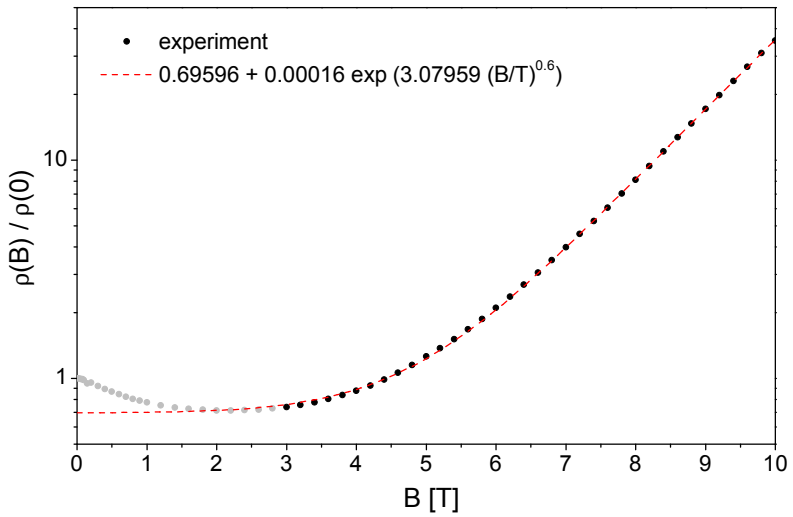

Figure 4.13: Comparison of the high field part of $\rho(B, T = 1.6\,\text{K})$ with theory done for sample C.

However, the shrinkage of the wave functions in the plane perpendicular to the magnetic field has a second, much more important effect. It leads to a significant decrease in the overlap of the wave function tails of neighboring impurities. This in turn exponentially increases the resistivity. An exponential positive magnetoresistance is usually an unambiguous evidence that the conduction mechanism is controlled by the overlap of wave functions of the charge carriers and can be regarded as proof of the hopping mechanism of conduction [12]. According to Shklovskii and Efros [12], as long as $H \gg H_C$, the magnetic field dependence has the form

$$\rho_3 = \rho_{3,0} \exp(\text{const} \cdot H^\alpha), \quad \text{for} \quad H_C = \frac{n^{\frac{1}{3}}\, c\, \hbar}{a_B\, e} \tag{4.2}$$

with α being slightly greater than 0.5. For n-GaAs this effect has been widely studied [65, 66, 68, 71]. In our case $H_C \approx 3\,\text{T}$ and thus the strong field case is expected. As shown in fig. 4.13, good agreement between experiment and theory is found for $\alpha = 0.6$. The weak field case cannot be investigated because of the strong negative contribution that obviously is of different origin.

Besides the exponential increase of $\rho(B)$ at high field, an enhancement of the activation energy ε_3 is expected due to wave function shrinkage. This was observed in sample C, as shown in fig. 4.14, where ε_3 increased from 0.31 meV without applied field to 0.58 meV at $B = 10$ T (fig. 4.9). The same is valid for sample B that showed an onset of exponential behavior at high fields in the magnetoresistance measurements. Although still small in absolute value, for sample B E_A increases by a factor of three.

Whereas the origin of the exponential positive contribution is clearly understood, the explanation of the strong negative contribution to the magnetoresistance seems to be more demanding. Similar results to those discussed here have been found for pure n-GaAs [80–82]. On the other hand, this does not seem to reflect common behavior, since experimental evidence exists showing either no or only small negative magnetoresistance [65, 66, 68, 71] in n-GaAs at low doping concentrations. From the theoretical point of view, there are several attempts to explain the origin of negative magnetoresistance in the hopping regime. One possible explanation proposed by Raikh [83] is related to the shrinkage of the wavefunction in the directions perpendicular to the applied field, which also accounts for the very large positive magnetoresistance at high magnetic fields as described above. In low magnetic fields, however, it is argued that the shrinkage of the wave function of the localized electronic states reduces the repulsion of the energy levels of neighboring states. This can affect the local density of states, leading to an increasing number of states at the Fermi energy and therefore to a higher conductivity.

Another mechanism of negative magnetoresistance is a model based on the interference of tunneling amplitudes for the electron that has transversed different paths, corresponding to different sequences of scattering acts. In this model, the coherent superposition of partial tunneling amplitudes that stem from the different paths results in a high resistance. Phase factors acquired by the motion

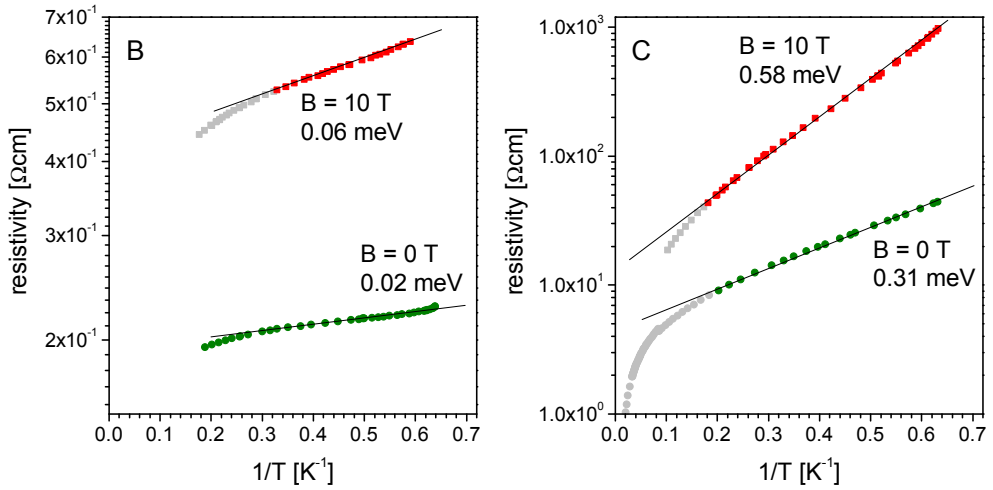

Figure 4.14: Increase of the activation energy ε_3 under the presence of a magnetic field presented for samples B and C.

in a magnetic field will destroy the interference, which increases the probability of a hop and reduces the resistance. This argument applies only for low magnetic fields in which the shrinkage of the wave function can be neglected. In the simplest case this involves just a triangle connecting three hopping states with interference between direct tunneling and tunneling with one scatterer only [84, 85].

Reference [81] describes a non-monotonous structure in the field region of negative magnetoresistance, similar to the one observed in sample B. The authors of reference [81] explain this structure as an interplay between the two mechanisms responsible for the negative magnetoresistance described above. Maliepaard et al. found this structure as well, but assumed Shubnikov-de-Haas oscillations as its origin [80].

Both mechanisms explain the existence of a negative magnetoresistance in the hopping regime. The results of the present work, however, cannot distinguish between the two mechanisms. Additionally, one has to keep in mind that the two mechanisms mentioned above assume a true hopping scenario. This assumption is not completely satisfied in the present situation. However, the samples under study approach the metal-insulator transition from the metallic side where weak localization plays an important role. It is well known that this effect leads to negative magnetoresistance as well and is getting more pronounced at lower carrier concentrations. In this context, it is not astonishing to observe an increased negative magnetoresistance for samples B and C.

In conclusion, it was shown that one observes a transition from metallic towards activated transport behavior within the range of impurity concentrations studied. One sample shows clearly metallic behavior without a hint of hopping conduction, while another shows all typical properties of hopping conduction, as activated transport is observed at zero field and the magnetoresistance curves are dominated by the wavefunction shrinkage effect in the presence of a magnetic field. The carrier concentration of the sample in between these two extremes marks the transition point by showing band transport at zero field (proven by the very small activation energy at $B = 0$ and high mobility of $248\,\mathrm{cm}^2/\mathrm{Vs}$ at $2\,\mathrm{K}$) and hopping transport at high applied fields.

It is important to note that the metal-insulator transition occurs at unexpectedly high carrier concentration, since similar samples of binary GaAs:Si were reported to show metallic conductance (e.g. [86]). This gives evidence for either a high degree of compensation present in the sample or a high degree of alloy-disorder introduced by the B-incorporation. Both would lead to an increased critical carrier concentration for a metal-insulator transition.

4.4 Evidence and influence of boron localized states on optical and transport properties of n-(B,Ga,In)As

The results of the last section already showed interesting modifications of the transport properties of n-(B,Ga,In)As alloys. The observed effects suggest an influence of boron localized states on the conduction band transport. In the following, further evidence for the existence of these states will be given and the influence of the localized B-states on the band structure will be discussed in more detail. The input from theory, i.e. the tight binding and supercell calculations performed by A. Lindsay, described at the beginning of this section, were found to be extremely valuable in this context. Experimentally, transport measurements once more proved to be a very sensitive probe for detecting the footprints of B-states. Especially transport measurements in conjunction with applied hydrostatic pressure were very useful in this context.

Boron related states - results of supercell calculations

A very valuable tool of theoretical band structure analysis for investigating the influence of localized states on the band structure of semiconductors is the so called *linear combination of isolated states (LCIS) model* introduced by A. Lindsay et al., which has been applied very successfully in the case of nitrogen localized states in Ga(N,As) [38, 87, 88]. Within this approach, one calculates the interaction of the B-states with the host (unperturbed) Γ conduction band minimum, while also incorporating the complexities of the local B environment. The model uses ultra large disordered (B,Ga,In)As supercells containing $M \sim 8000$ boron atoms placed at random on the group III sites of the lattice. The number M of boron atoms and the size of the supercell is adjusted to obtain the desired boron fraction of 2.7%. In a first step, full tight binding calculations using an accurate sp^3s^* tight binding Hamiltonian revealed that the electronic state of an isolated boron atom $\psi_{B,0}$ is resonant with the conduction band of the GaAs host. Furthermore, it is highly localized, namely approximately 50% to 60% of the probability of the electronic impurity state on B-sites and the corresponding first neighbors. Thus, in a second step, one can associate a similar localized wave function $\psi_{B,i}, i = 1, ..., M$ with each B atom in the system and the wave functions of the perturbed system can be well represented as a linear combination of M isolated boron resonant states together with the GaAs CBE wave function, which is the basis of the LCIS. The distribution of B cluster state energies is derived by diagonalizing the $M \times M$ matrix, linking the M individual B states $\psi_{B,i}$ to obtain M boron cluster states $\psi_{B,l}$ with energies ϵ_l. The histogram in fig. 4.15 depicts the distribution of these boron related cluster states which stretches out considerably in energy[2].

[2]The extended states of the host crystal are not included in fig. 4.15.

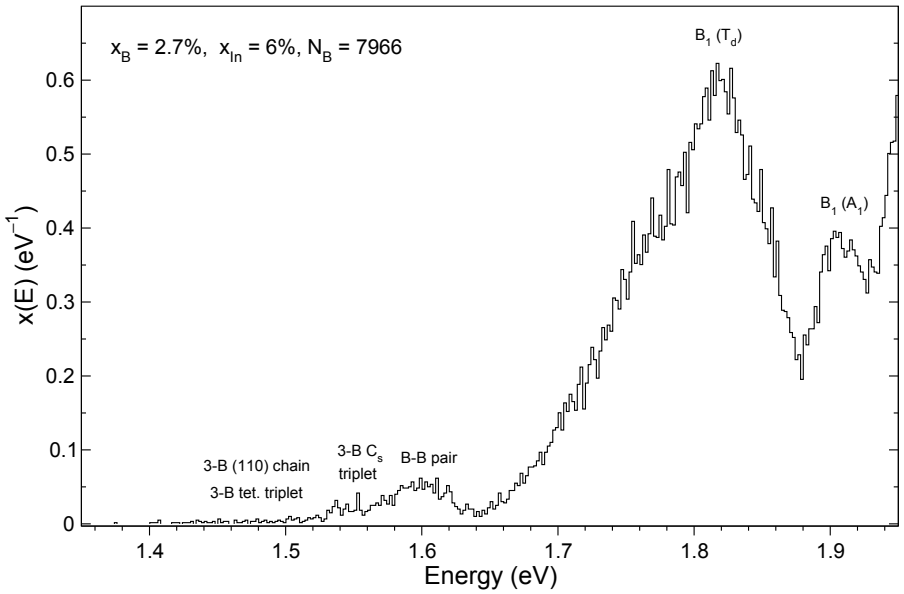

Figure 4.15: Density of boron related states calculated within the LCIS-approach, using an ultra large supercell containing $N_\mathrm{B} = 7966$ boron atoms ($x(E)$ gives the fraction of B-states with energy E with $\int_0^\infty x(E)/4\,dE = 0.027$). $T = 0\,K$. Energies are given with respect to the valence band maximum. Figure courtesy of A. Lindsay [49].

The calculations indicate a distinct structure in the density of boron related states. Clearly visible are the two peaks related to isolated boron B_1 with T_d and A_1-symmetry at approximately 1.7 eV and 1.8 eV, respectively. However, there also exist cluster states in considerable numbers at much lower energies, i.e. in the vicinity of the band edge which is located at $E_\mathrm{C} = 1.45\,\mathrm{eV}$ at 10 K. Those states are attributed to boron pair states and higher cluster states such as states of B-triplets or longer B-chains. The structure in the low energy extension of the distribution is not very well resolved by the calculations because of the limitations in the supercell size.

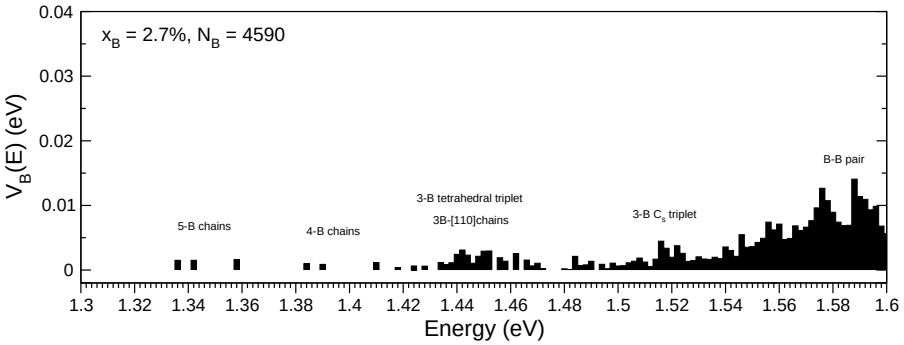

Figure 4.16: Calculated distribution of B-cluster states weighted by their interaction with the CBE state, i.e. their fractional Γ-character. Figure courtesy of A. Lindsay [49].

For optical measurements not only the pure density of states, but also their Γ-character is relevant, as it determines the probability for optical transitions. It is obtained by a projection of the calculated B-states on the unperturbed CBE states of the host. Due to their lack of Γ-character, many B-related states cannot be detected in optical studies, as e.g. all B_1-states of T_d-symmetry. Figure 4.16 presents a histogram similar to fig. 4.15 with the difference that the density of boron cluster states is weighted by their Γ-character. Although the two plots 4.15 and 4.16 are not directly comparable, because the latter is calculated for an In free case, which slightly changes the distribution, fig. 4.16 can give useful information. It shows that, approaching from the low energy side, the first states with significant relevance are the 3-B tetrahedral triplets and 3-B chains. They have a lower density (as e.g. compared to B-pairs), but are comparatively strong in Γ-character. The calculations suggest that these states are in the direct vicinity of the (Ga,In)As host conduction band edge which is located at 1.426 eV at low T [89]. Hence the theory sketched out so far gives a good starting point for the interpretation of the experimental results that will be presented in the following. It should be noted that within the limits of the tight binding parametrization, the energies of these levels can only be predicted within an accuracy of a few tens of meV. However, this does not affect the nature of these impurity states.

Results of optical spectroscopy

The theoretical analysis suggested a widespread distribution of resonant B-related cluster states that stretches out towards the conduction band edge of the unperturbed (Ga,In)As host. Within the search for indications of isovalent B states, at first results of optical measurements shall be discussed. These were obtained by photomodulated reflectance and contactless electromodulated reflectance. The spectra were recorded using the setups described in section 2.3. The 442 nm line of a HeCd laser was used as the source of the modulated light field. The spectra were taken at various temperatures in the range from 10 K to room temperature in the case of photomodulated measurements. With the cryostat used for electromodulated measurements temperatures below 50 K were not accessible. The samples used for the optical measurements were undoped but of the same B and In-composition ([B]=2.7%, [In]=6%) than those studied in the transport measurements.

Figure 4.17 presents the results of these measurements. Since the bandgap of $B_{0.027}Ga_{0.913}In_{0.060}As$ is expected to be located at 1.426 eV at low T, the energy scale is restricted to the range from 1.3 eV to 1.54 eV. As modulation spectroscopy reveals signals at critical points of the band structure, one would expect one single derivative like signal due to the interband transition between valence and conduction band of the unstrained layer. However, for both measurement techniques, more complicated lineshapes are observed. Besides the usual Varshni-shift towards higher energies with decreasing T, both signal strength and signal shape show distinct variations with temperature. At 10 K, the PR-measurements show two maxima of equal height. With increasing T, signal

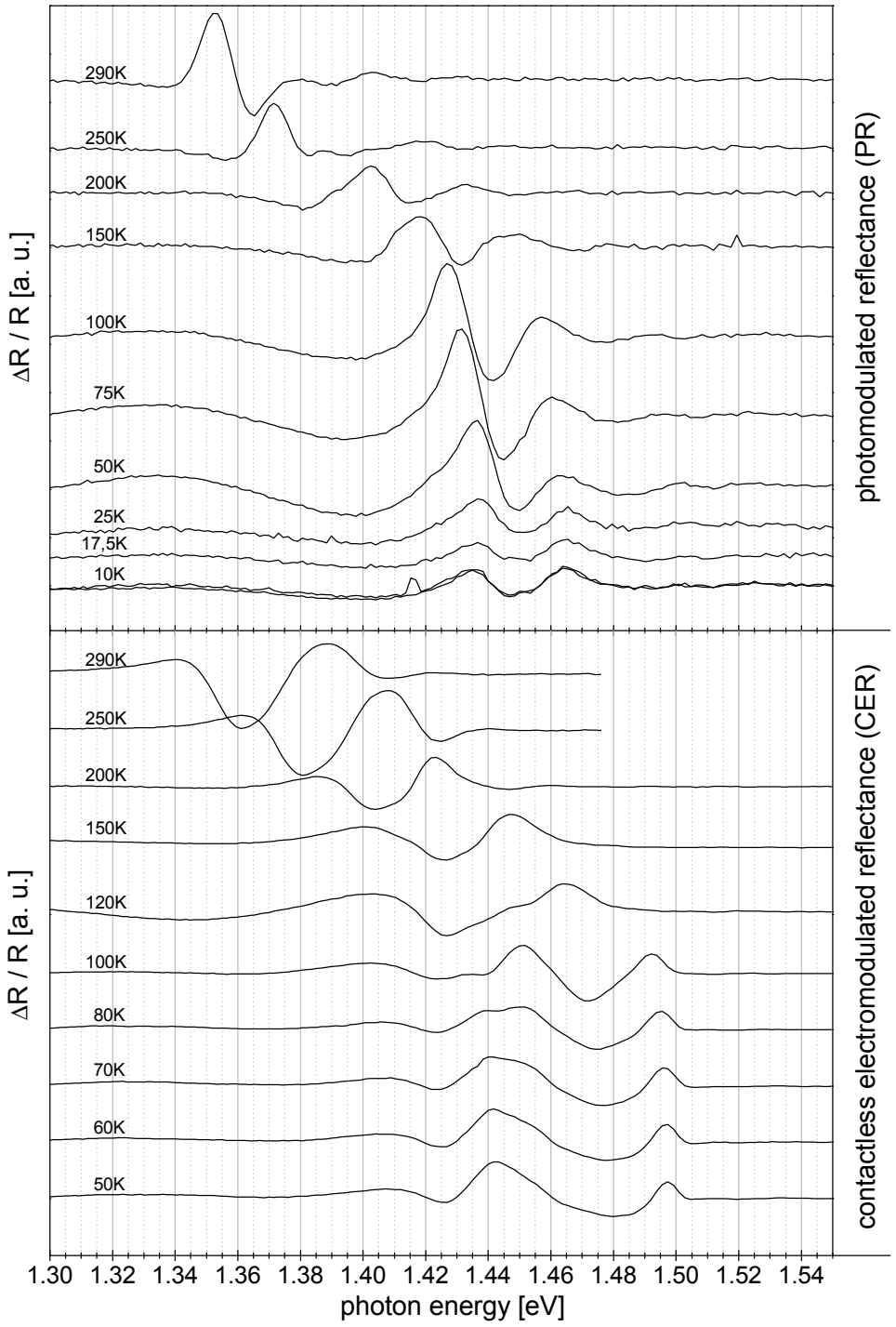

Figure 4.17: Optical spectra of undoped (B,Ga,In)As samples. The spectra were recorded at various temperatures, using different measurement setups. Top: photomodulated reflectance; bottom: electromodulated reflectance (contactless method). All spectra show a complicated signal shape indicating the presence of boron related states in the vicinity of the band edge.

strength is transferred in favor of the low energy signal, while above 150 K just one signal can be observed. In electromodulated spectra the complex lineshapes become even more apparent. The signal shape drastically changes from single derivative like at room temperature towards peak like at $T = 50$ K with a very complicated shape at intermediate temperatures. The additional signal at 1.49 eV is most likely due to the GaAs buffer layer between the epitaxial layer and the substrate.

Taking into account the results of the calculations, these unusual lineshapes can be interpreted as an influence of B-states on the conduction band edge. Because of the continuous and extended structure of their distribution and their very small Γ-character, no clear signals are to be expected, but subtle modifications of the lineshape cannot be excluded. In both types of modulation spectroscopy, internal electrical fields are modulated, thus one has to have a closer look at the peculiarities of the Stark effect and the resulting modifications of the oscillator strength. In the typical case, when the states involved in optical transitions are well separated in energy, i.e. the corresponding transition energies do not coincide, the energy shift (Stark shift) of the levels dominates the oscillator strength and modulated spectra have a typical lineshape consisting of derivatives of a single complex oscillator (e.g. Lorentzian of Gaussian). However, if transition energies coincide and the corresponding states are resonant in energy, an exchange of oscillator strength may occur, which may enhance the intensity of the weaker oscillator (e.g. B-related transition), whilst decreasing the intensity of the main transition (e.g. band gap transition). This results in a complex lineshape no longer describable by a single oscillator.

Since the temperature dependence of the conduction band edge differs from that of the B-states, the B-environment at the band edge will vary when the temperature is changed. For the B-cluster states, an energy shift of +40 meV with decreasing T between room temperature and 0 K can be assumed [49]. Because the Varshni-shift of the conduction band states is about twice as large, the separation between the conduction band edge and the B-clusters will be lowered with decreasing T and the corresponding transitions approach each other. This can explain that the unusual lineshape modifications are not visible at room temperature, but become apparent at intermediate T. According to the tight binding calculation, one may speculate that the states responsible for these effects are those of B-triplets.

Another way of altering the relative energetic positions of the conduction band edge and the boron related states is to apply hydrostatic pressure. Under hydrostatic pressure, the band gap of (B,Ga,In)As increases and, with respect to the valence band maximum (VBM), both CBE- and B-states change their energetic positions. However, this occurs with different pressure coefficients. Whereas the conduction band edge and shallow donor states shift at a rate of about $dE_C/dP = 11$ meV/kbar [54], the localized boron states hardly change in energy within the experimentally accessible pressure range, i.e. below 20 kbar. According to the tight binding calculations of A. Lindsay, they even have a small, but here negligible negative pressure coefficient. This is intrinsic to the nature

of these impurity states which are derived significantly from the host X-states (which for GaAs and most conventional semiconductors have a negative pressure dependence with respect to the valence band maximum)[3]. Consequently, by applying hydrostatic pressure one gradually changes the number and type of B-cluster states in the vicinity of the conduction band edge. For this reason optical measurements were performed under hydrostatic pressure. The measurements were performed using the optical clamp pressure cell described in section 2.5.

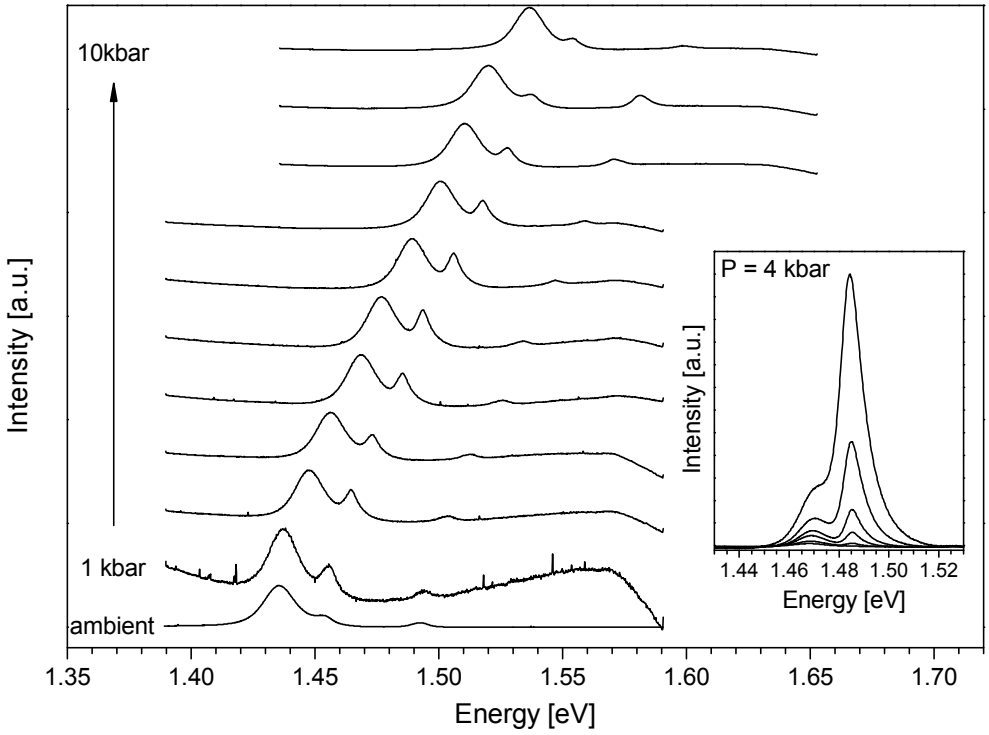

Figure 4.18: Photoluminescence spectra of (B,Ga,In)As at 10 K for various pressures. Inset: Measurements at 4 kbar with increasing excitation power.

If the B-states possessed a typical character of isovalent traps, one would expect to find luminescence of excitons bound to isovalent B-traps as soon as they appear in the band gap. Figure 4.18 shows photoluminescence spectra at 10 K for various values of the applied pressure. Two signals at 1.438 eV and 1.454 eV are visible with the narrower one being higher in energy. It is due to the interband transition between conduction and valence band. The second signal, significantly broader and lower in energy, can be identified as being caused by carbon acceptor states (C is a common impurity in MOVPE grown semiconductors). The impurity character of the low energy signal is confirmed by the excitation density dependence, as this transition saturates and shifts towards higher energies with increasing excitation power (see inset of fig. 4.18). Signa-

[3]This is in contrast to the N-states in Ga(N,As) which consist mainly of L and Γ character and therefore have a similar pressure dependence as the conduction band edge, although significantly weaker.

tures of B_{As} double acceptors or $B_{As} - Si_{Ga}$ complexes [90] have not been found. With increasing pressure both signals shift in parallel towards higher energies at a rate that agrees with the expected value. However, no indications of B-states appearing in the band gap can be detected. On the one hand one may argue that B-cluster states are present in sufficient numbers to be detectable up to 10 kbar. On the other hand one has to keep in mind that recombination via

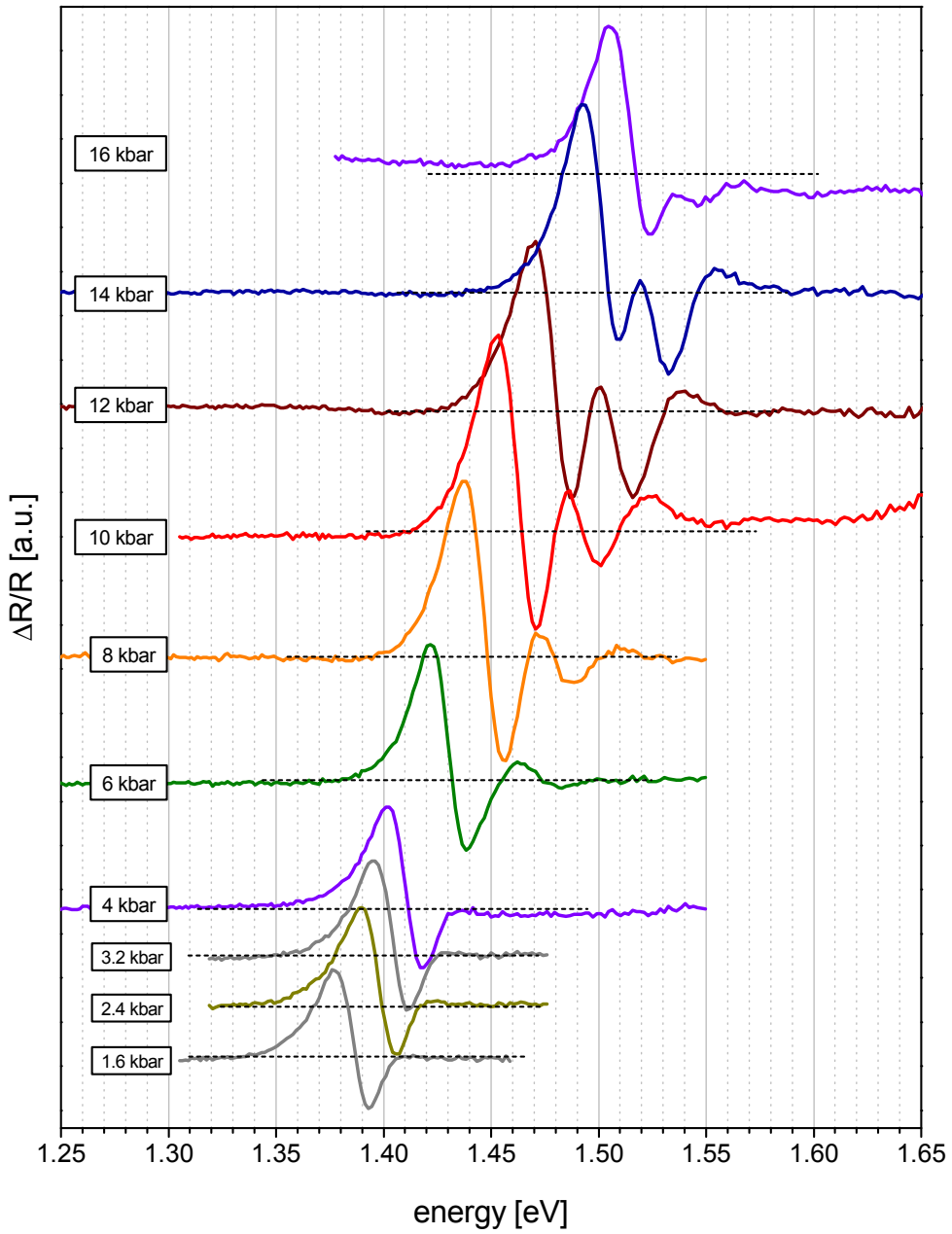

Figure 4.19: Optical spectra obtained by photomodulated reflectance at room temperature under the influence of hydrostatic pressure. The results show modifications of the signal shape above 6 kbar.

carbon-acceptor bound excitons provides a very efficient recombination channel that may totally cover any signs of isovalent traps such as boron where excitons are expected to be bound very weakly.

Therefore, photoluminescence appears to be inadequate in this special case. Another attempt to find the signs of B-cluster states are photomodulated reflectance measurements under hydrostatic pressure. These measurements were performed at room temperature, using the optical clamp pressure cell. The results are presented in fig. 4.19. Despite the fact that the signal increases in energy at the rate of $dE_C/dP = 10\,\mathrm{meV/kbar}$ close to the reported value, the signal does show well pronounced variations in its shape and strength above 6 kbar. This result supports those of the temperature dependent measurements, as in both experiments unusual signal modification appear, when the separation between conduction band edge and B-cluster states decreases.

Although the optical experiments give useful hints for the existence of boron localized cluster states closely above the conduction band edge and the overall validity of the physical picture described so far, there is the need for a much more sensitive probe to fully clarify the situation. In the following, it will be shown that transport measurements under hydrostatic pressure do serve as such a sensitive probe, since changes in the nature of the electronic states that contribute to transport have critical impact on the measured resistivity.

Influence of hydrostatic pressure on the magnetotransport properties of n-GaAs

Before discussing the influence of hydrostatic pressure on the transport properties of n-(B,Ga,In)As, it is very useful to study first its influence on n-GaAs which can be considered as a reference alloy. The contrast in transport behavior between GaAs and (B,Ga,In)As will then become even more obvious.

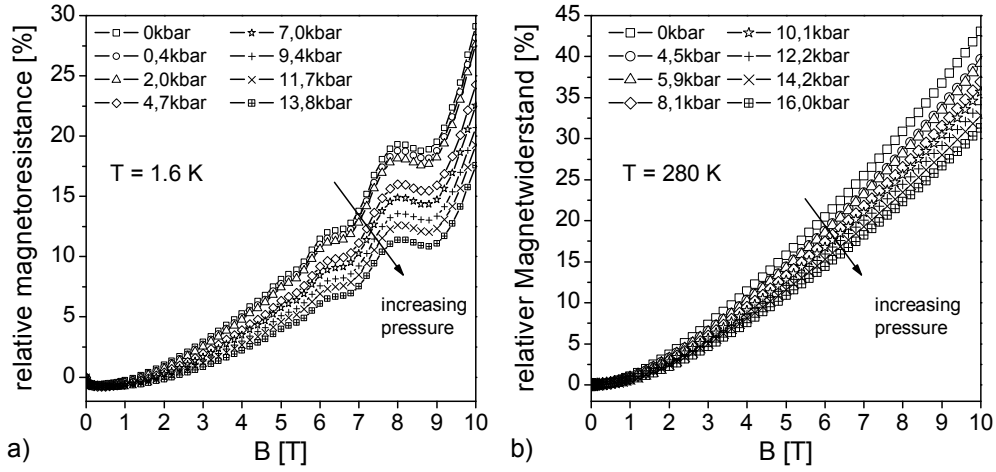

Figure 4.20: Magnetoresistance of GaAs:Te at various hydrostatic pressure at a) 1.6 K and b) 280 K.

The n-GaAs sample used for these measurements is the same one already presented in section 4.3, discussing fig. 4.11. It was mounted into the clamp pressure cell described in section 2.5 and hydrostatic pressure up to 16 kbar at room temperature (14 kbar at 1.6 K) was applied. The absolute values of the resistivity hardly change under pressure, i.e. from $1.4 \times 10^{-4}\,\Omega$cm at ambient pressure to $1.8 \times 10^{-4}\,\Omega$cm at 14 kbar (1.6 K). Figure 4.20 presents pressure induced changes on the relative magnetoresistance curves both at low temperature (a) and at room temperature (b). Obviously, hydrostatic pressure cannot change the overall qualitative behavior at all up to the highest pressure value. The small negative magnetoresistance at low temperature ($\approx -1\%$) is hardly changed and Shubnikov-de-Haas oscillations are preserved. For all pressures the quadratic behavior is maintained. The only significant influence of pressure is an increasing aperture (broadening) of the parabolas, although the changes are very small (decrease of relative magnetoresistance at 10 T by 10% only).

This effect can be well explained with a decreasing mobility under pressure, which is confirmed by the mobility values extracted from the Hall data, as shown in fig. 4.21. The steady decrease of the mobility is due to an increasing effective mass, as reported e.g. in [91, 92]. In GaAs the fundamental band gap increases under pressure at a rate of 11.5 meV/kbar. Since shallow donor levels are closely connected to the states of the conduction band edge, the shallow impurity levels shift in parallel with the conduction band edge. For this reason, no variation of the free carrier concentration and thus no variation of the ionization energy was found (see fig. 4.21).

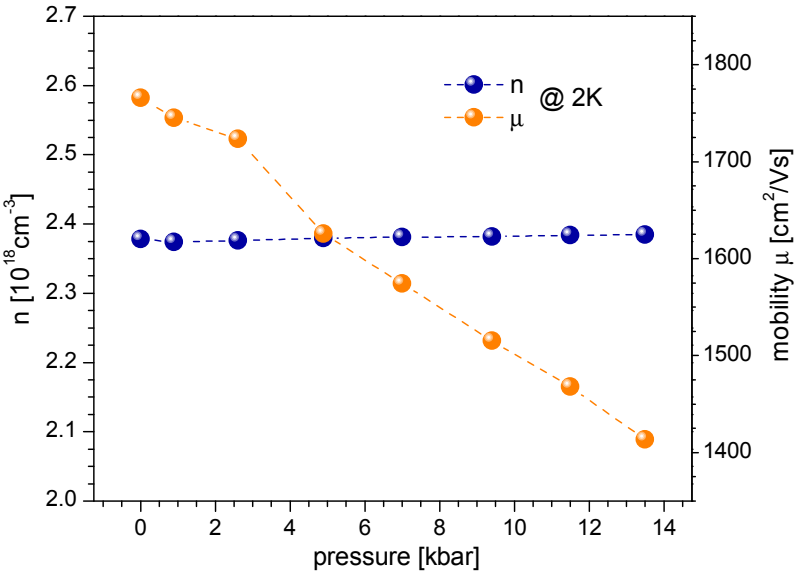

Figure 4.21: Changes of carrier concentration and mobility under hydrostatic pressure of the GaAs:Te reference sample.

Influence of hydrostatic pressure on the interplay of extended and localized states

It was shown that the influence of hydrostatic pressure on the transport properties of n-GaAs is rather weak. In the following, pressure induced effects on the transport in (B,Ga,In)As will be studied. As it will be shown, the changes in this system are quite dramatic compared to GaAs.

Up to now, there exists no theoretical approach that properly describes the physics close to the transition range between metallic and non-metallic transport regimes. The approximations used in many theoretical models developed for extreme limits of low and heavy doping break down in the intermediate range, which makes it extremely difficult to find suitable explanations for the observed experimental results. Circumstances seem even more challenging in (B,Ga,In)As due to the complexity of the situation where the interplay between three subsystems has to be considered. Those are the extended band states of the (Ga,In)As host, the slightly broadened distribution of localized Si shallow donor states and the very broad distribution of extremely localized boron related states with its distinct structure. Astonishingly, despite these difficulties, the observed experimental results can be quite well understood qualitatively.

The samples under investigation are the same as in section 4.3. It will be shown soon that the resistivity of the samples increases strongly under hydrostatic pressure. Unfortunately, this excluded sample C (with the lowest concentration of Si donors) from the pressure measurements because of its hardly measurable resistivity even at ambient pressure. Thus, only samples A and B were used for the experiments under high pressure.

Figures 4.22 b) and d) depict the influence of hydrostatic pressure on the absolute resistance values. Common to both samples is that hydrostatic pressure induces a strong exponential increase of the absolute resistivity at zero field. Whereas the effect is quite moderate at room temperature, it is well pronounced at low temperatures where the increase of resistivity extends over several orders of magnitude and is much stronger than in n-GaAs. A simple enhancement of the effective mass does not seem sufficient at all as an explanation. In the case of sample A, $\rho_{1.6\,\mathrm{K}}(P)$ seems to increase even more rapidly above 10 kbar. The resistance of sample B grew too large to allow accurate and reliable measurements above 5.6 kbar.

When studying the magnetoresistance variations under pressure, the two samples seem to show qualitatively different behavior at first glance. In the case of sample B (lower n, fig. 4.22a), one observes a dramatic increase of the positive contribution at high fields that had been attributed to wave function shrinkage in hopping transport (see section 4.3). Whereas the negative contribution hardly changes (as seen best in the magnification in the inset of fig. 4.22a) and maintains its value of approximately -30%, the onset of the exponential positive contribution is shifted towards lower magnetic fields, leading to extraordinary

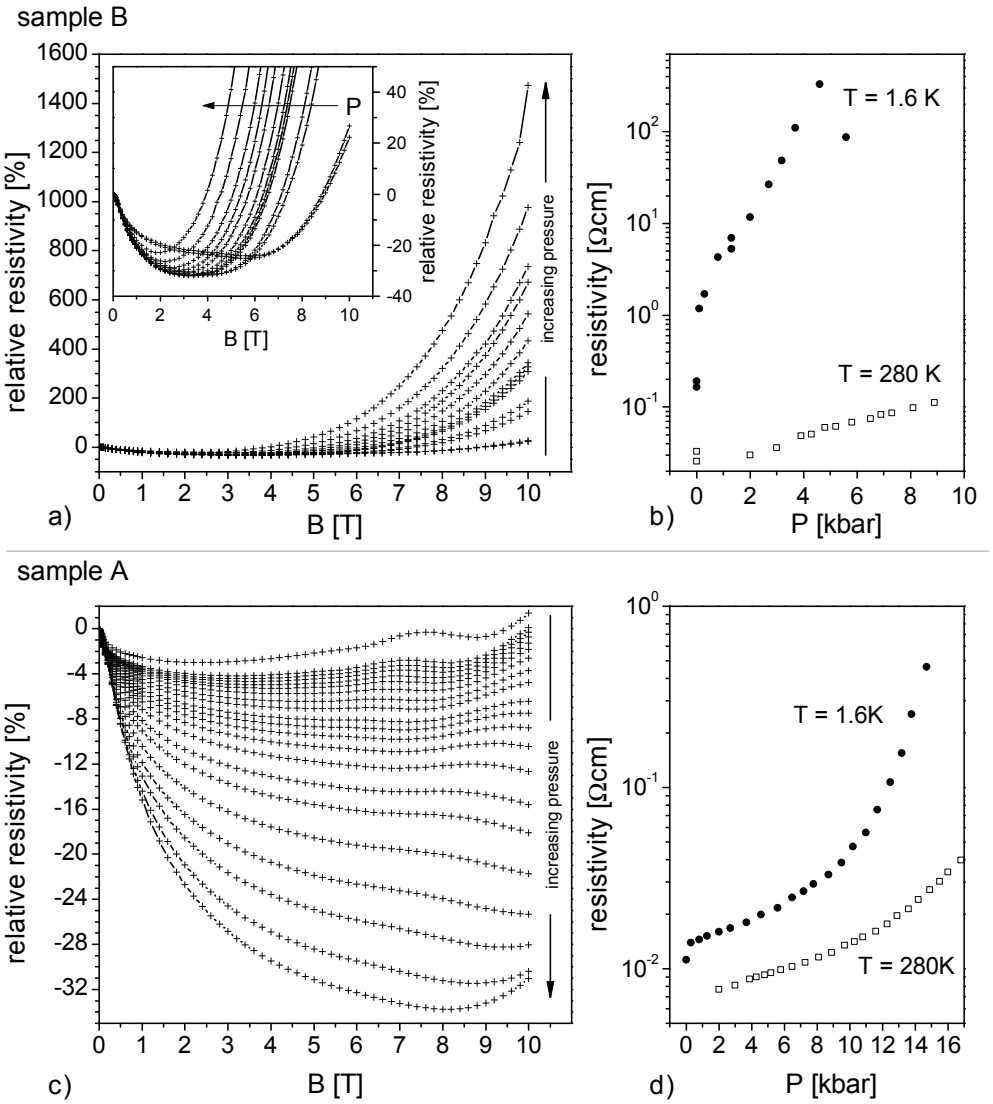

Figure 4.22: Resistivity under hydrostatic pressure. a, c) Relative magnetoresistance curves for various applied pressure values. b, d) Pressure dependence of the absolute resistivity at zero magnetic field.

high values of more than 1500% at 10 T. At ambient pressure already, this sample was on the verge of being non-metallic and a considerable amount of the transport took place between localized states, otherwise wave function shrinkage effects would not have been visible. Under pressure these shrinkage effects become more pronounced, indicating a greater role of localized states. One may presume a shift of the Fermi level towards the region of localized states. In general, the qualitative behavior resembles that of the "hopping sample" C in section 4.3.

At first sight the results of the metallic sample A are in contrast to those just described. For this sample (higher n, fig. 4.22c) applying pressure leads to a

strong enhancement of the negative magnetoresistance effects. The minimum of the magnetoresistance curves decreases from -3% at ambient pressure towards approximately -30% at 14 kbar which is about the same value as observed in all samples that showed indications of hopping transport. At the highest accessible pressure, the increase of ρ above 8 T might be interpreted as an onset of the wave function shrinkage effect. If this were true, one would again interpret the results as a shift of the Fermi level towards a region of localized states. The more pronounced negative magnetoresistance effects under pressure are then easily explained by the increasing disorder due to potential fluctuations within the framework of weak Anderson localization.

In conclusion, both samples show surprising magnetoresistance effects under pressure, when compared to the GaAs case where the resistance and magnetoresistance curves hardly change under pressure. The results already admitted the assumption of a shifting Fermi level towards a region with localized states.

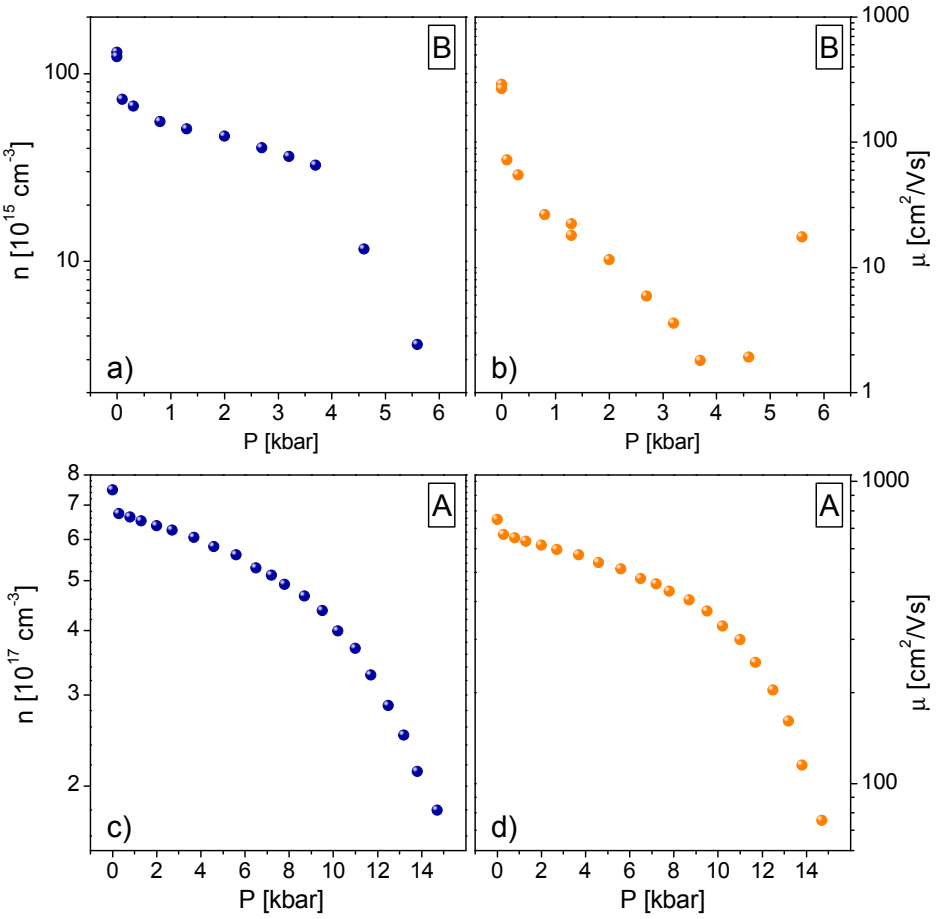

Figure 4.23: Dependence of free carrier concentration n and electron mobility μ on hydrostatic pressure. Data obtained from combined resistivity and Hall measurements at 1.6 K.

The reasons for these drastic changes in resistivity become clearer, when investigating the dependencies of the free carrier concentration n and mobility μ on hydrostatic pressure as determined from combined Hall and resistivity measurements that are presented in fig. 4.23.

Both samples show qualitatively similar results, i.e. a strong decrease of both quantities n and μ. In the case of sample B, n decreases by almost two orders of magnitude and the rate rises considerably above 4 kbar. The mobility decreases up to 4 kbar as well and slightly increases again above 4 kbar. For sample A, a monotonous decrease of both n and μ is observed. Above approximately 8 kbar, this happens with increasing rate. This observation indeed is a most valuable hint towards an explanation of the unusual magnetotransport results.

At ambient pressure, both samples show almost (sample B) or clearly (sample A) metallic behavior with quite high electron mobilities. This allows to conclude that the Fermi level must be close to the extended conduction band states of the host.

Under pressure the conduction band edge shifts towards higher energies with respect to the valence band maximum, as mentioned above, whereas the B-cluster states hardly change. Consequently, one obtains a variation of the relative energetic position of the conduction band edge with respect to the boron localized states. Schematically, the different situations at 2 K and at room temperature are illustrated in fig. 4.24[4]. At low temperatures, a significant portion of the boron cluster states, namely the several triplet states, that lie above the conduction band edge at ambient pressure are assumed to be located below the conduction band edge at 15 kbar.

With this picture in mind, the reduction of the free carrier concentration n under pressure is closely connected to boron cluster states. It can be explained by a trapping of carriers that fall below the conduction band edge with increasing pressure. In this simplified picture, the Si donor states serve as a reservoir of carriers that loses electrons into B-states with increasing pressure P. This explanation allows further analysis of the $n(P)$ data. By numerical differentiation one obtains dn/dP which is a measure for the density of states that fall below the conduction band edge. The results of this analysis are presented in fig. 4.25 for both samples. In the case of sample B, the Hall-resistance suffered from strong noise due to the high sample resistance. This is manifested in the strong scattering of the dn/dP-data points that were obtained at different magnetic field strengths. Therefore and due to the limited pressure range, this data will not be discussed further. The results obtained for sample A are

[4]The parameters used here were the following: $dE_C/dP = 10\,\mathrm{meV/kbar}$ (from PR-measurements under pressure), $dE_B/dP = 0\,\mathrm{meV/kbar}$, $E_C(P = 0\,\mathrm{kbar}, T = 10\,\mathrm{K}) = 1.45\,\mathrm{eV}$ and $E_C(P = 0\,\mathrm{kbar}, T = 293\,\mathrm{K}) = 1.36\,\mathrm{eV}$. Furthermore, the B-spectrum as a function of energy has been calculated for both 0 kbar and 15 kbar in order to confirm that there is no significant variation due to pressure between B-states of different energy which, if present, would "stretch-out" or "contract" the B spectrum with pressure. All of this had been done using the same random B distribution for consistency of course.

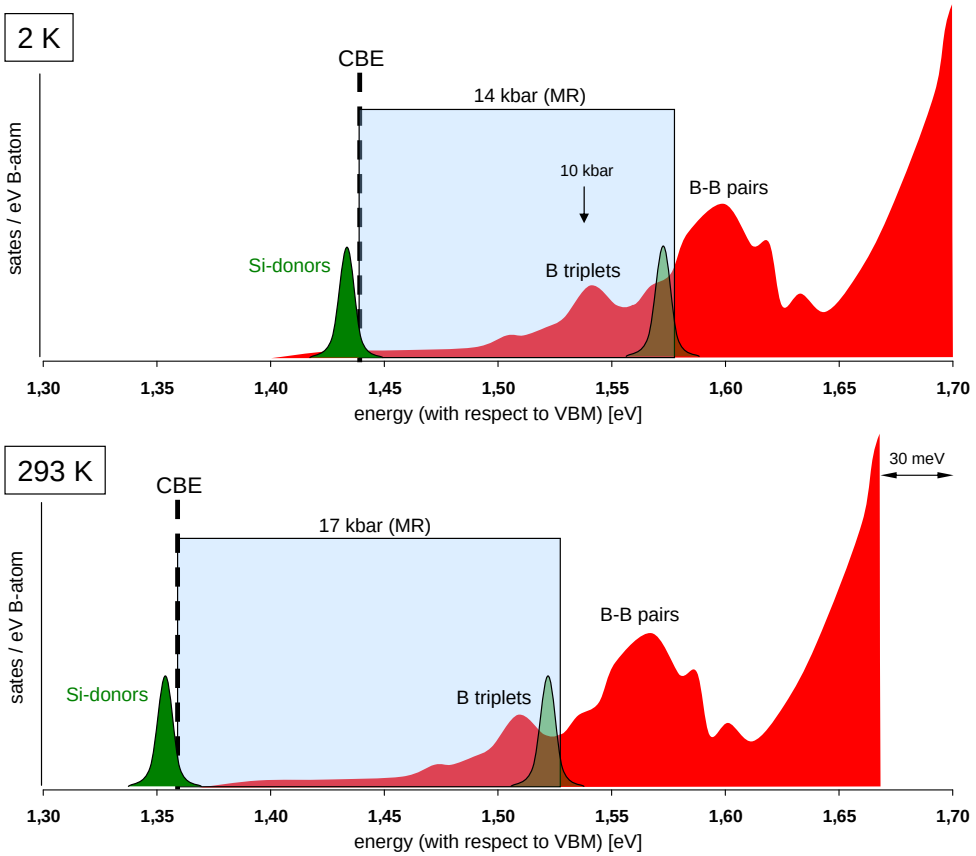

Figure 4.24: Schematic illustration of the consequences of applying hydrostatic pressure, when the conduction band edge is shifted through the distribution of localized B-cluster states. The two figures correspond to low and high temperature. Boron localized states are shown in red, silicon donor states in green. Gray areas indicate the pressure range accessible in transport measurements.

much more convincing, as the dn/dP-data is almost independent of the magnetic field.

When compared to the theoretical density-of-states calculations, striking similarities appear. The maximum of dn/dP at about 12 kbar can be interpreted as being due to the C_S triplet states. The total number of these states can be approximated as $1 \times 10^{18}\,\mathrm{cm}^{-3}$ which is close to the measured free carrier concentration of $n = 8 \times 10^{17}\,\mathrm{cm}^{-3}$ (ambient pressure) which can be regarded as the "volume" of the reservoir[5]. Still the number of B-states seems too high compared to the available free carrier concentration, since lower lying clusters should already have trapped a considerable amount of carriers. This allows to conclude that not all B-cluster states are able to trap carriers. In detail, this problem remains an open question for further theoretical analysis of the trapping mechanism.

[5]It holds that $N_{\mathrm{triplet}} \approx 4x^3$ with the total boron concentration $x = 0.027$.

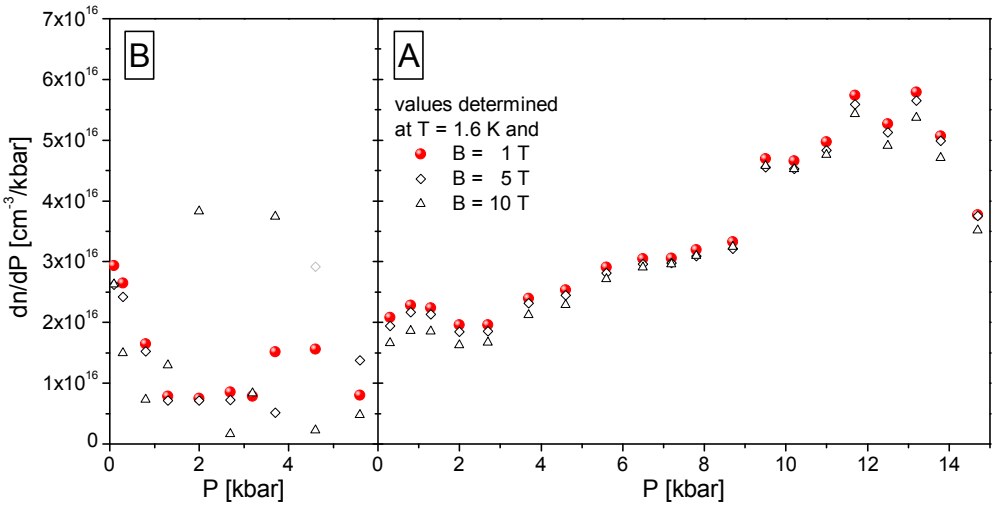

Figure 4.25: Pressure dependence of dn/dP obtained by numerical differentiation of the experimental data. This quantity corresponds to the density of B-related states in the simple trapping model.

Figure 4.24 also suggests that the energy range under pressure covered at 2 K differs slightly from that at 293 K and the maximum in dn/dP should appear at higher pressure values. This is in excellent agreement with experiment, as presented in fig. 4.26 that shows $n(P)$ at 280 K together with the extracted dn/dP-data (red data points). Black data points represent low temperature data (same as fig. 4.25) shifted by 3.0 kbar towards higher pressure (equivalent

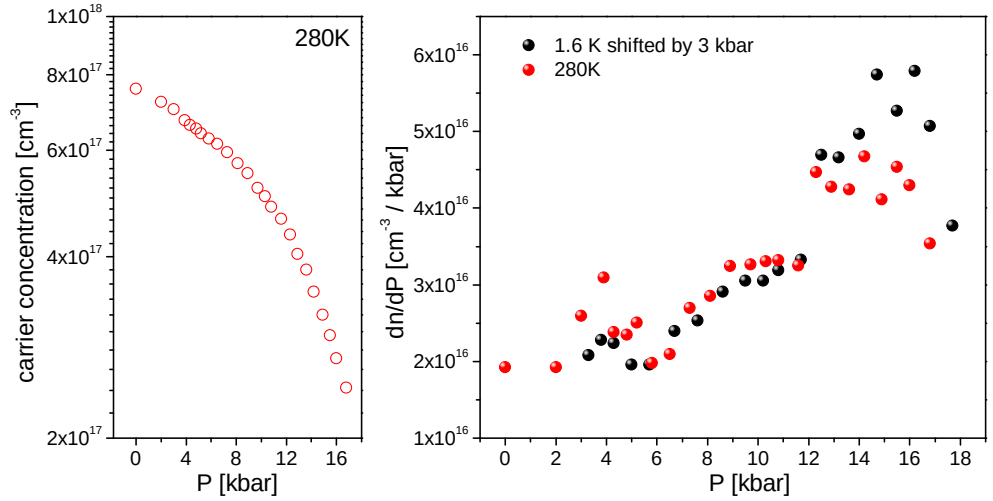

Figure 4.26: a) Dependence of the free carrier concentration on hydrostatic pressure at room temperature. b) Comparison of dn/dP values obtained at 1.6 K and at room temperature. The 1.6 K data have been shifted by 2.8 kbar towards higher P to show the similarity of the two data sets.

to 30 meV shift in energy). The excellent match is a further hint for the validity of the scenario shown in fig. 4.24.

The considerably decreased mobility observed for both samples under pressure (fig.4.23) is also in concordance with the presence of boron cluster states in the vicinity of the Fermi level, as the cluster states are excellent scattering sites. With an increased number of boron states below the conduction band edge, it is not surprising to find the Fermi level within a region of localized states at high pressures and thus to measure typical impurity band mobilities of the order of $10\,\mathrm{cm}^2/\mathrm{Vs}$ even for the originally metallic sample A.

This picture is further backed up by an analysis of the activation energy that was extracted from the temperature dependence of the resistivity at low temperatures. Figure 4.27 displays the pressure dependence of this activation energy for both samples.

In the case of sample B (fig. 4.27 a), a significant exponential increase of the activation energy can be observed. Since this sample is almost metallic at ambient pressure, the activation energy is very small of the order of 10^{-2} meV. However, with increasing pressure the Fermi level shifts down in energy into the region of localized boron and silicon states and the activation energy consequently reaches typical values for nearest neighbor hopping of 0.5 meV.

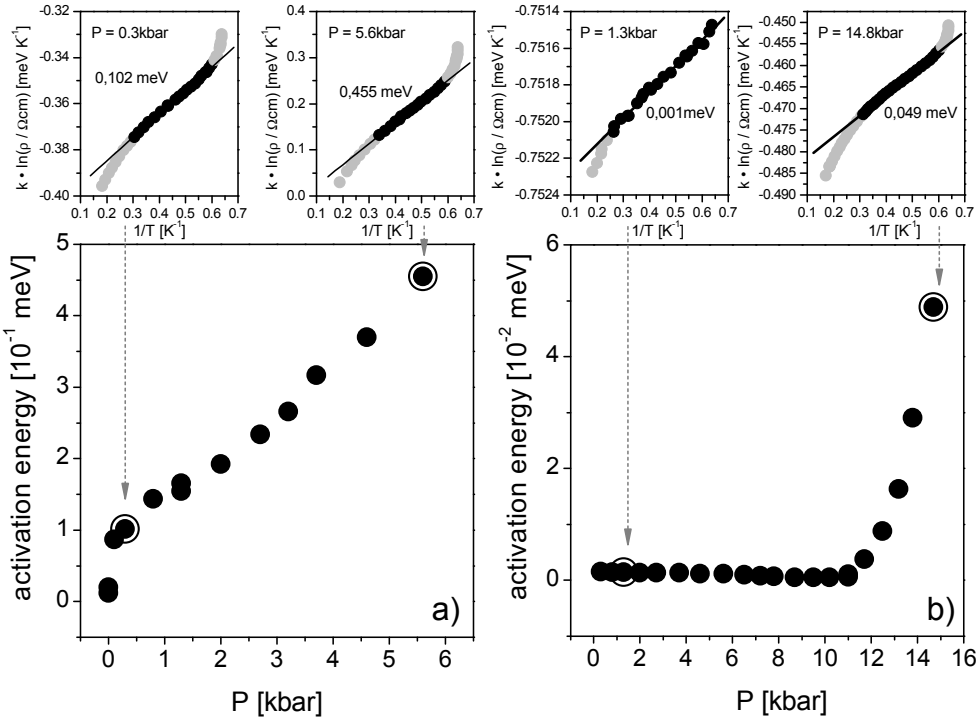

Figure 4.27: Pressure dependence of the activation energy of a) sample B and b) sample A. The values were determined from low temperature $\rho(T)$-plots as exemplarily shown in the upper graphs for the marked pressure values.

In the other case of the metallic sample A, one might ask whether or not it makes sense to measure an activation energy at all. At $P = 0\,\mathrm{kbar}$, the analysis of $\rho(T)$ gives values as low as $1\,\mu\mathrm{eV}$, which can hardly be labeled activation energy compared to $k_\mathrm{B}T \approx 138\,\mu\mathrm{eV}$. Above 11 kbar, however, the activation energy is suddenly strongly increased. It can be supposed that the Fermi level now substantially decreases, since triplet states with high density traverse the conduction band edge and hopping transport between localized states becomes more likely, although the transport path along more extended states still predominates. At 15 kbar, the activation energy is of the order of 0.1 meV and the situation is on the verge of non-metallic behavior.

Conclusions

The material system (B,Ga,In)As renders a complex system with manifold interactions of localized and extended states. Despite the difficulties brought about by this complexity, the properties can be well explained by the model described in the preceding sections. Most valuable were the measurements under hydrostatic pressure that revealed a pressure induced metal-insulator transition. One of the main ideas in this context was the trapping of carriers in localized B-related cluster states that appear in the bandgap at high pressure. In fact, one of the key conclusions that can be drawn from the experimental results is that boron atoms indeed seem to have the character of isovalent electron traps, rendering boron as the first known isovalent trap induced by cationic substitution. Although this character is not as obvious as in other cases, e.g. due to the weak Γ-character of the states, it becomes apparent by a careful evaluation of the experiments. Although none of the experiments alone may appear convincing enough to confirm the existence of resonant B-states and the isovalent trap character of boron impurities, the large number of individual pieces of information that can all be explained within the same picture is conclusive.

5 Influence of isovalent nitrogen and boron on the thermoelectric properties of (Ga,In)(N,As) and (B,Ga,In)As

In the preceding chapter, it was shown that the incorporation of isovalent nitrogen or boron into (Ga,In)As results in strong disorder effects in the conduction band. These become manifest in a variety of experimental findings. In the case of (Ga,In)(N,As), optical spectroscopic studies of interband transitions, involving both conduction and valence band states, often show that a strong linewidth broadening of the interband transitions occurs with increasing content of the isovalent impurity N or that the band gap related photoluminescence of (Ga,In)(N,As) exhibits large Stokes shifts and an S-shaped temperature dependence of its peak position [93, 94].

Transport experiments on n-type (Ga,In)(N,As) and (B,Ga,In)As exhibit striking similarities with strongly disordered or amorphous semiconductor systems, whereas p-type samples behave like conventional semiconductor alloys. Examples are the enhanced weak Anderson localization effects due to strong scattering by the electronegative impurities in n-type (Ga,In)(N,As) and (B,Ga,In)As [50–52] or the insulator-to-metal transition observed in n-type (B,Ga,In)As at low temperatures at a critical carrier concentration which is almost an order of magnitude higher than in conventional semiconductors, as shown in section 4.3. On the other hand, many properties of the perturbed extended host states can still be described in the framework of band structure models, relying on crystal periodicity, e.g. $\mathbf{k} \cdot \mathbf{P}$ models, if their interaction with the B and N cluster states is properly accounted for. Examples are the effective mass or the gyromagnetic factor of the conduction band electrons [35, 37].

The Seebeck effect of n-type semiconductor alloys is a thermoelectric property which is also strongly related to transport of electrons in the conduction band. In particular, the temperature dependence of the Seebeck coefficient in the temperature range from 300 K down to liquid helium temperatures differs considerably between amorphous and crystalline semiconductor materials [4].

In this chapter, it will be studied which of the two facets of the ambivalent conduction band character, i.e. ‘amorphous’ or ‘crystalline’, dominates the Seebeck coefficient of these non-amalgamation type alloys [95, 96]. The results are discussed in the context of the phonon structure of these alloys.

Sample properties and sample preparation

The samples used for thermoelectric and Raman measurements discussed in this chapter were similar to those used for the magnetotransport measurements of chapter 4. They were epitaxial layers of (Ga,In)(N,As) and (B,Ga,In)As with B and N concentrations of about 3% grown by metal-organic vapor-phase epitaxy on semi-insulating (100) GaAs substrates [60, 97, 98]. The sample thickness was about 1 μm. The In-contents of all samples were chosen such as to obtain lattice matching to GaAs. A series of GaAs:Si epitaxial layers served as reference. Compositions, dopants, and free carrier concentrations are summarized in table 5.1. These data were obtained at room temperature by Hall measurements, using pieces of the same epitaxial layer. The undoped samples were used for the Raman measurements described in section 5.3.

No	composition	n[cm^{-3}]	μ[cm^2/Vs]
B–1	$B_{0.027}Ga_{0.913}In_{0.060}As$:Si	1.2×10^{18}	1140
B–2	$B_{0.027}Ga_{0.913}In_{0.060}As$	undoped	
N–1	$Ga_{0.935}In_{0.065}N_{0.038}As_{0.962}$:Te	2.5×10^{17}	330
N–2	$Ga_{0.935}In_{0.065}N_{0.038}As_{0.962}$:Te	7.0×10^{17}	270
N–3	$Ga_{0.935}In_{0.065}N_{0.038}As_{0.962}$:Te	1.8×10^{18}	430
N–4	$Ga_{0.935}In_{0.065}N_{0.038}As_{0.962}$:Te	2.2×10^{19}	130
N–5	$Ga_{0.935}In_{0.065}N_{0.038}As_{0.962}$	undoped	
Ref–1	GaAs:Si	8.6×10^{16}	4130
Ref–2	GaAs:Si	2.0×10^{17}	3320
Ref–3	GaAs:Si	2.5×10^{18}	1810
Ref–4	GaAs:Si	5.0×10^{18}	1200
Ref–5	GaAs	undoped	

Table 5.1: Properties of the samples used for thermoelectric and Raman measurements. Free carrier concentration and mobility were determined by Hall measurements at room temperature.

For the thermoelectric measurements, each sample was cleaved into a stripe of $4 \times 15\,\mathrm{mm}^2$. Indium was attached to the ends of the stripe as ohmic contacts and CoNi/NiCr thermocouples were soldered into the In contacts. The sample was mounted into the apparatus described in section 2.2 and proper corrections for the measurement wires have been performed (see eqs. 2.7, 2.8). The sample pieces were large enough to establish well defined temperature gradients along the sample and to obtain good measurement accuracy for temperatures as low as 45 K.

5.1 The thermoelectric power

In the range of low temperatures, the total thermoelectric power of a semiconductor crystal can be divided into two parts. The first is due to the electron diffusion, when a temperature gradient is present. The second is connected with

the fact that the temperature gradient in the lattice produces a phonon current. In other words, the thermoelectric power S can be expressed as the sum of an electronic part and a phonon part [95]

$$S = S_e + S_p. \tag{5.1}$$

In the following, both parts will be considered in more detail, before the results of the thermoelectric measurements will be presented.

The electronic contribution to the Seebeck coefficient

The general expression for the Seebeck coefficient given by the Boltzmann transport theory in relaxation time approximation reads [99]:

$$S_e = -\frac{1}{eT}\frac{\mathcal{L}^1}{\mathcal{L}^0} \tag{5.2}$$

where the integrals $\mathcal{L}^\alpha$ are defined as[1]

$$\mathcal{L}^\alpha = e^2 \int \frac{\mathrm{d}\boldsymbol{k}}{4\pi} \left(-\frac{\partial f}{\partial \epsilon}\right) \tau\left(\epsilon(\boldsymbol{k})\right) \nabla_{\boldsymbol{k}}\epsilon(\boldsymbol{k}) \cdot \nabla_{\boldsymbol{k}}\epsilon(\boldsymbol{k}) \left(\epsilon(\boldsymbol{k}) - \varepsilon_\mathrm{F}\right)^\alpha . \tag{5.3}$$

Here $f(\epsilon)$ denotes the carrier distribution function, $\tau(\epsilon)$ the relaxation time, $\epsilon(\boldsymbol{k})$ the energy dispersion relation and ε_F the Fermi level.

For a lightly doped semiconductor[2] in the impurity range, i.e. when the number of intrinsic carriers is negligible compared to the number of carriers released by impurities, the following two assumptions can be made. First the carriers obey classical statistics and the distribution function may be replaced by the Boltzmann distribution function $f(\epsilon) = \exp\left(-(\epsilon - \varepsilon_\mathrm{F})/k_\mathrm{B}T\right)$. Secondly, most of the carrier scattering is due to the lattice and the relaxation time is independent of the carrier kinetic energy. In such a situation, eq. 5.2 can be written for a parabolic band of the form $\epsilon(\boldsymbol{k}) = E_\mathrm{C} + (\hbar^2/2m)\,\boldsymbol{k}^2$ as:

$$S_e = -\frac{k_\mathrm{B}}{e}\left[\frac{E_C - \varepsilon_F}{k_\mathrm{B}T} + 2\right]. \tag{5.4}$$

Furthermore, the Fermi level is related to the carrier density n as

$$E_\mathrm{C} - \varepsilon_\mathrm{F} = k_\mathrm{B}T \ln\left(\frac{2\left(2\pi\, m_\mathrm{eff}\, k_\mathrm{B}T\right)^{3/2}}{8\pi^3\hbar^3\, n}\right) \tag{5.5}$$

and the electronic contribution to the Seebeck coefficient may be written as

$$S_e = -\frac{k_\mathrm{B}}{e}\left[\ln\left(\frac{T^{3/2}}{ne}\right) - A + \frac{3}{2}\ln\left(\frac{m_\mathrm{eff}}{m_0}\right)\right] \tag{5.6}$$

[1] For simplicity it is assumed that only one single band is involved and no interband transitions take place, i.e. that no band index has to be considered.

[2] with a single sign of carrier predominating

with

$$A = 2 + \ln\left(\frac{2\,e\,(2\pi\,m_0\,k_\mathrm{B})^{3/2}}{8\pi^3\hbar^3}\right). \tag{5.7}$$

The assumption of pure lattice scattering is best fulfilled for samples at high temperatures and low impurity concentrations. With decreasing temperature and increasing impurity content, scattering by impurity atoms has to be taken into account. According to Conwell and Weisskopf [100], the mean free path due to impurity scattering is roughly proportional to the square of the kinetic energy. Thus, $\tau(\epsilon)$ will depend on energy and the integrals in 5.2 can only be solved numerically, which was done by Johnson et al. [101]. Astonishingly, in eq. 5.6 the only consequence of the introduction of impurity scattering is a variation of A from $A = 5.32$ for pure lattice scattering to $A = 3.82$ for pure impurity scattering[3].

The phonon drag effect

In the presence of a temperature gradient, the lattice vibrations are not isotropic, but travel preferentially from the hot part of the crystal to the cold part. As a consequence, the scattering of charge carriers is not random. It is more likely that carriers are scattered towards the cold parts than the reverse. This effect is called the phonon drag effect [95]. As a result, the cold parts of the crystal will acquire an excess of carriers and an electrostatic field will be established. The system reaches equilibrium and the current will be zero, when this electrostatic field counterbalances the combined effect of the phonon drag and the normal tendency of carriers to diffuse from hot to cold. The mutual drag of charge carriers and phonons obviously increases the absolute value of S regardless of the sign of carriers involved. Since at high temperatures the lattice vibrations are more rapidly restored to randomness by phonon-phonon collisions in particular Umklapp processes, the effect of the phonon drag is more pronounced at low than at high temperatures. Therefore, the typical signature of the phonon drag is a sharp rise of the Seebeck coefficient at low temperatures [102–104]. As long as one sign of carrier predominates over the other, the effect on S is independent of the carrier concentration, at least if n is sufficiently low.

A large concentration of crystalline imperfections can directly scatter low-energy phonons. Thus, the phonon drag effect has been observed only in semiconductor crystals of high crystalline perfection. In strongly disordered systems, the phonon drag will be suppressed. In amorphous semiconductors, the phonon contribution S_p can be neglected at all, because no extended, but only localized phonon modes exist and the coupling between the modes is weak [4].

[3] This assumes that n is determined as $n = 1/(eR_\mathrm{H})$ and the Hall constant R_H is measured in cm^3/C.

5.2 The influence of isovalent nitrogen and boron on the Seebeck coefficient

The results of the thermopower measurements are depicted in fig. 5.1. For all curves, $|S|$ decreases slightly with decreasing temperature, reaching a minimum at approximately 100 K. Below 100 K, $|S|$ is strongly enhanced due to the phonon drag effect. The temperature dependence of the Seebeck coefficients is very similar for all three material systems. In particular, no distinct differences can be observed due to the incorporation of nitrogen and boron.

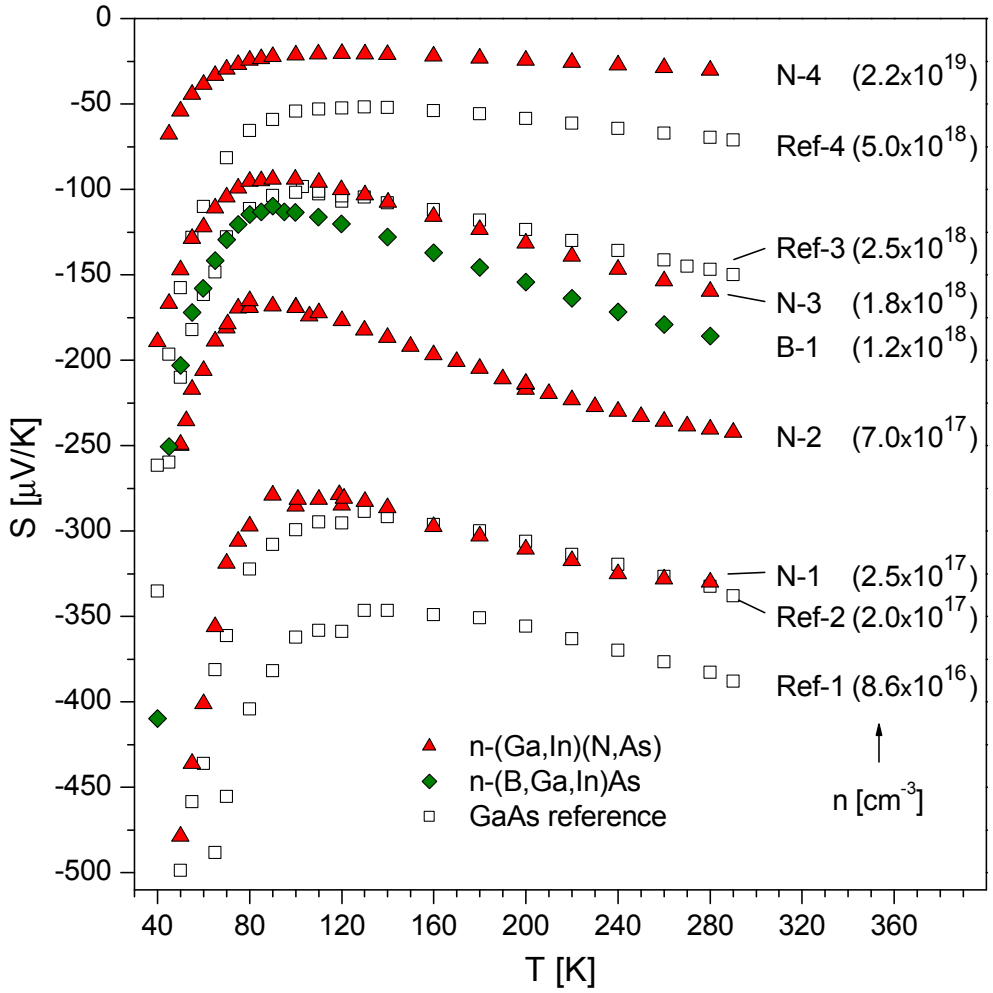

Figure 5.1: Temperature-dependent Seebeck coefficients of n-type (Ga,In)(N,As), (B,Ga,In)As and GaAs of different doping.

From eq. 5.6, it can be seen that a change in free electron concentration n and/or effective mass m_{eff} leads to a shift of $S\,(T)$-curves that can be nicely observed in fig. 5.1. At room temperature, the Seebeck coefficient is dominated by the electronic contribution, which allows a comparison of the experimental values with the prediction of eq. 5.6. This is depicted in fig. 5.2 where $S\,(T)$ is plotted

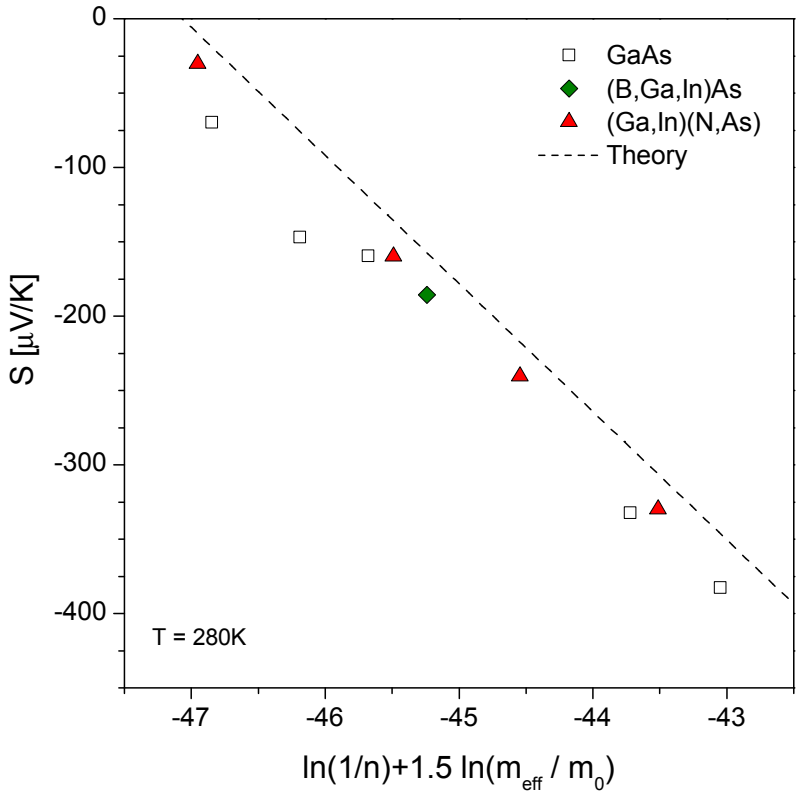

Figure 5.2: Comparison of Seebeck coefficients measured at 280 K (symbols) with the theoretical prediction of equation 5.6 (dotted line).

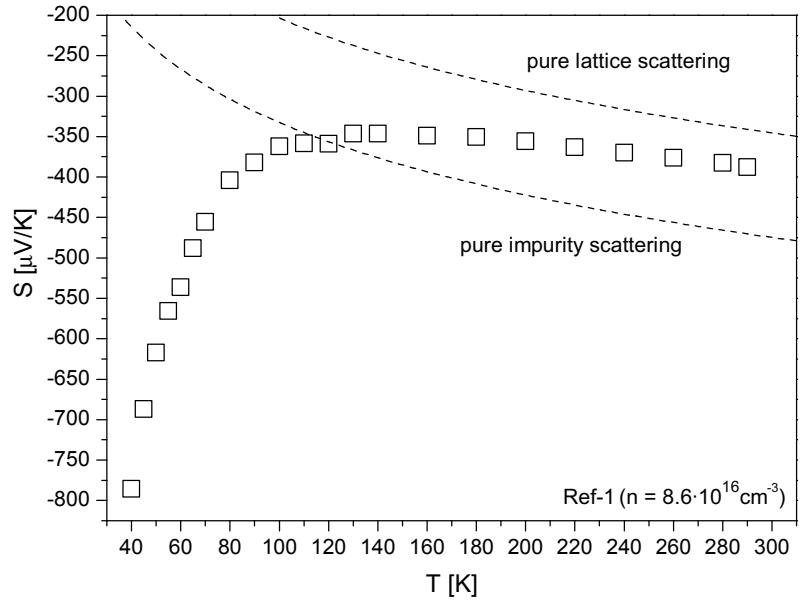

Figure 5.3: Comparison of experimental data of the Seebeck coefficient (sample Ref-1) as compared to the predictions of equation 5.6.

versus $\ln(1/n) + \frac{3}{2}\ln(m_{\text{eff}}/m_0)$. Reasonable values for the effective mass were used according to the literature (B-1: 0.09 [47]; N-1 to N-3: 0.1, N-4: 0.2 [105]; Ref-1 to Ref-4: interpolated 0.067–0.08 [106]).

Due to a non-zero phonon contribution, the experimental Seebeck coefficients lie below the theoretical curve (dotted line) predicted by eq. 5.6. Below room temperature, i.e. in the temperature range studied the phonon drag effect starts to play an important role reflected by the deviations of the experimental curves of $S(T)$ from the theoretical prediction based on eq. 5.6, which is shown exemplarily for sample Ref-1. The two dotted lines represent the two cases of pure lattice scattering and pure impurity scattering. As expected, the experimental values are close to the limit of pure lattice scattering at higher T and approach the limit for pure impurity scattering with decreasing T. Below 100 K, the deviations become unambiguous, indicating a well pronounced phonon drag effect. As mentioned above, the existence of a phonon drag effect implies the existence of a distinct structure of extended phonon modes.

5.3 Probing the phonon structure using Raman measurements

Figure 5.4 depicts Raman spectra of (B,Ga,In)As, (Ga,In)(N,As) and a GaAs-reference sample obtained at room temperature. All three samples show a sharp peak between 290 and 300 cm^{-1} due to first-order scattering by LO-phonons. The signal at lower energies between 260-270 cm^{-1} can be assigned to TO-phonon scattering. It has a much lower intensity than the LO-peak, being forbidden by selection rules in backscattering from a (100)-surface. The similar intensities of TO- and LO-signals in (Ga,In)(N,As) are an indication of the weakening of the selection rules due to increased structural disorder. At higher Raman shifts in the range of 400 to 600 cm^{-1}, additional structures become visible. Three lines at 506 cm^{-1}, 534 cm^{-1} and 570 cm^{-1}, respectively, occur in the GaAs spectrum that can be assigned to second-order Raman scattering by LO+TO(K), 2TO(L) and 2LO(Γ), respectively [107]. These lines, though broadened, also appear in the spectra of the other two samples. However, in addition to those, (Ga,In)(N,As) and (B,Ga)(In,As) show signals of local vibrational modes. In (B,Ga,In)As, this is mainly the peak at 515 cm^{-1} and the shoulder on its high energy side (see arrows in fig. 5.4) that were shown to originate from ^{10}B and ^{11}B local vibrations, respectively, in ternary (B,Ga)As [108–110]. In case of (Ga,In)(N,As), a more complicated structure is expected and found resulting from the various possibilities of N bonding in different environments, as widely discussed in literature [111–114]. The Raman measurements demonstrate that the incorporation of the much lighter N and B-atoms into the (Ga,In)As-host leads to a two-mode behavior. The dispersions of extended phonons, acoustic as well as optical phonons, of the (Ga,In)As host almost remain intact, i.e. the host phonons possess a defined wave-vector. In contrast, the N- and B-related modes are strongly localized and no defined phonon dispersion exists. In other

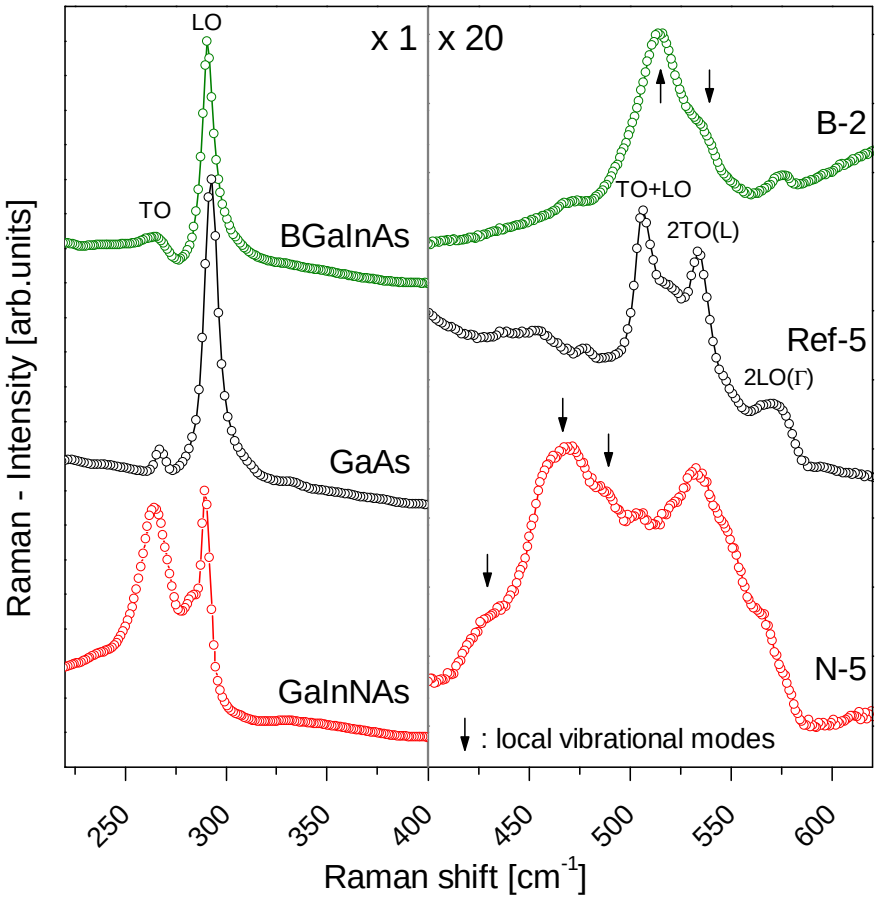

Figure 5.4: Unpolarized Raman spectra of undoped (B,Ga,In)As, (Ga,In)(N,As) and GaAs obtained at room temperature.

words, the (Ga,In)As phonons are crystal-like, whereas the localized vibrational modes are similar to those in amorphous material.

5.4 Conclusions

Whereas the electric-field driven electronic transport in n-type (Ga,In)(N,As) and (B,Ga,In)As differs considerably from that of n-type GaAs, the temperature-gradient driven electronic transport is very similar for the three semiconductors, despite the distinct differences in the conduction band structure of (Ga,In)(N,As) and (B,Ga,In)As compared to GaAs. The temperature-dependent Seebeck coefficients are almost the same for non-amalgamation type alloys and GaAs with the same free carrier concentration, i.e. the non-amalgamation type alloys exhibit a Seebeck effect typical for conventional crystalline semiconductors. This similar behavior in case of temperature-gradient driven electric transport is caused by the similarity of the dispersions of the extended phonon states of the three semiconductor materials in conjunction with the dominance of the phonon drag

effect. From a thermoelectric point of view, both (Ga,In)(N,As) and (B,Ga,In)As appear with crystalline character rather than amorphous. In electric-field driven electronic transport, phonons are less important and the differences in the electronic structure between the non-amalgamation type alloys and GaAs become more apparent.

6 Influence of magnetic ions on the impurity band transport and the metal-insulator transition in semiconductors

By incorporating magnetic impurities into semiconductors, one immediately enters interesting intermediate areas between the fields of magnetism and semiconductor physics. One example is the area of so called dilute magnetic and magnetic semiconductors where currently one main interest lies on obtaining ferromagnetic semiconductors with Curie temperatures above room temperature, which may be employed as spin injectors or spin aligners in future III-V semiconductor spintronics or spin-optoelectronics [115–117]. To achieve this aim one usually attempts to raise the magnetic ion content within the semiconductor to a few percent, i.e. to obtain magnetic semiconductor alloys.

The first section of this chapter addresses such dilute magnetic semiconductors (DMS), using paramagnetic $Zn_{0.94}Mn_{0.06}Se$ epitaxial layers as an example and modifications of the impurity band transport induced by magnetic interactions will be studied. In this material, Mn^{2+} ions provide large localized magnetic moments due to their half filled inner 3d-shells, but, being isovalent with the Zn cations, do not lead to a doping of the crystal and the charge carriers are provided by additional Cl donors. Thus, localized magnetic moments and shallow impurity atoms are of different origin and do not coincide spatially. Nevertheless, the electronic wavefunction of a Cl donor overlaps with several hundred magnetic ions, when the concentration of magnetic ions is of the order of a few percent. The resulting magnetic interactions can strongly affect the impurity band transport.

The second section focuses on InSb:Mn samples with low magnetic impurity content. Here the situation is different. In III-Mn-V compounds the magnetic impurity Mn serves both as the source of a large localized magnetic moment and as the source of a loosely bound hole due to its acceptor character. It will be shown that due to the on-site character of the magnetic interaction between acceptor hole and localized 3d-states of magnetic ions (despite their low concentrations), a significant influence on the transport behavior close to the metal-insulator transition is observed.

Magnetic interactions

The magnetic interactions in magnetic semiconductors are manifold and complex. Besides the interaction with an applied external magnetic field leading to Landau quantization and normal Zeeman splitting, a carrier with spin $\boldsymbol{s}$ interacts with the local magnetic moments of the magnetic ions[1]. This interaction, the s,p-d exchange, may completely dominate the other contributions leading to the so called giant Zeeman splitting of the energy levels in paramagnetic dilute magnetic semiconductors. Additionally, the local magnetic moments are influenced by the external magnetic field and the interaction between them via direct exchange coupling (d-d exchange coupling). The magnetic part of the Hamiltonian of a system consisting of a free carrier with spin $\boldsymbol{s}$ and magnetic ions with spin $\boldsymbol{S}_i$ is usually written in the form

$$\begin{aligned} H_{\text{magnetic}} &= H_{\text{Landau}} + \hat{g}\mu_{\text{B}}\boldsymbol{B}\boldsymbol{s} - \sum_i J_{\text{s,p-d}}\boldsymbol{S}_i\boldsymbol{s} \\ &\quad -\frac{1}{2}\sum_{i\neq j} J_{\text{d-d}}\boldsymbol{S}_i\boldsymbol{S_j} + \sum_i g\mu_{\text{B}}\boldsymbol{B}\boldsymbol{S}_i \ . \end{aligned} \tag{6.1}$$

The first and second terms denote the Landau quantization and the normal Zeeman splitting, respectively. The third contribution describes the s,p-d exchange interaction between the spin of the free carrier and the spins of localized magnetic ions, giving rise to the giant Zeeman splitting. The last two terms are due to the interaction of the magnetic ions between themselves and with the external magnetic field. Most important for this chapter is the s,p-d exchange interaction $H_{\text{s,p-d}} = -\sum_i J_{\text{s,p-d}}\boldsymbol{S}_i\boldsymbol{s}$. It can be treated in a mean field approximation, which allows to substitute the individual spins of the magnetic ions S_i by the average spin in magnetic field direction $\langle S_z\rangle$ which can be described by a modified Brillouin function:

$$\langle S_z\rangle = aSB_S\left(\frac{g\mu_{\text{B}}SB}{k_{\text{B}}(T+\theta)}\right) \tag{6.2}$$

with the empirical parameters a and θ and

$$B_S(x) = \frac{2S+1}{2S}\coth\left(\frac{2S+1}{2S}\,x\right) - \frac{1}{2S}\coth\left(\frac{1}{2S}\,x\right). \tag{6.3}$$

The antiferromagnetic temperature $\theta > 0$ opposes the paramagnetic ordering of a spin and the parameter a accounts for a net reduction of spin per magnetic

[1] In ferromagnetic dilute magnetic semiconductors such as (Ga,Mn)As with a few percent of Mn, additional effects such as carrier-carrier interaction and RKKY interaction (ferromagnetic coupling of localized magnetic moments by the free carrier plasma) come also into play. These will not be discussed here, because they are not of importance in the following, as the carrier concentrations in the samples are much too low for these effects to be dominant.

ion. The latter results from a strong antiferromagnetic interaction between localized moments due to superexchange that takes place in pairs, triplets and larger clusters of magnetic ions in the crystal. Therefore, an effective concentration of magnetic ions can be defined as $x_{\text{eff}} = ax$ with $0 < a < 1$ [118]. Within the virtual crystal approximation, the summation over Mn sites can be substituted by a summation over the whole cationic sublattice and multiplying by the effective concentration x_{eff}. Taking into account these approximations, $H_{\text{s,p-d}}$ can be treated by perturbation theory. With the s-like wavefunction $|\psi_{\text{s}}\rangle$ for the conduction band and the p-like wavefunction $|\psi_{\text{p}}\rangle$ for the valence band, the giant Zeeman splitting of the conduction and valence band at the Γ-point is given by:

$$\begin{aligned} \Delta E_{\text{C}} &= -N_0\alpha\, x_{\text{eff}} s_z \langle S_z\rangle\,, \quad s_z = \pm\frac{1}{2} \\ \Delta E_{\text{V}} &= -\frac{1}{3}N_0\beta\, x_{\text{eff}} j_z \langle S_z\rangle\,, \quad j_z = \pm\frac{1}{2}, \pm\frac{3}{2} \end{aligned} \tag{6.4}$$

with the number of unit cells per cm^3 N_0 and the exchange interaction parameters $\alpha = \langle\psi_{\text{s}}|J_{\text{s,p-d}}|\psi_{\text{s}}\rangle$ and $\beta = \langle\psi_{\text{p}}|J_{\text{s,p-d}}|\psi_{\text{p}}\rangle$.

For a concentration of magnetic ions of the order of several per cent, this splitting is usually much larger than the other modifications of the band structure in a magnetic field due to Landau level quantization

$$\Delta E_{\text{Landau}} = \left(n + \frac{1}{2}\right)\hbar\omega_c, \quad n \in \mathbb{N} \quad \text{with} \quad \omega_c = \frac{\hbar eB}{m_{\text{eff}}} \tag{6.5}$$

and normal Zeeman splitting

$$\Delta E_{\text{Zeeman}} = \hat{g}\mu_{\text{B}} B s_z. \tag{6.6}$$

6.1 Magnetically induced modifications of the impurity band transport

The hopping mechanism of conduction in ordinary, non-magnetic semiconductors has been studied extensively, but little is known about the influence of magnetic interactions in this regime. In $\text{II}_{1\text{-x}}\text{-Mn}_{\text{x}}\text{-VI}$ compounds (e.g. (Cd,Mn)Te, (Zn,Mn)Te, (Zn,Mn)Se), Mn^{2+}-ions are incorporated isovalently on group II lattice sites. The half filled d-shells of Mn ions reside deeply within the valence band, but give rise to local magnetic moments (total spin $S = 5/2$). At a concentration of $x \approx 5\%$, the hydrogen-like wavefunction of a shallow donor overlaps with several hundred localized spins giving rise to s-d exchange interaction described above. This section discusses the magnetotransport properties of n-doped $Zn_{0.94}Mn_{0.06}Se$ crystals with doping concentrations both below and above the metal-insulator transition. Although II-Mn-VI compounds were extensively studied in the past, magnetotransport measurements of (Zn,Mn)Se have not been reported up to now.

The (Zn,Mn)Se samples used for the experiments were grown by molecular-beam epitaxy (MBE) on semi-insulating (001) GaAs substrates [119]. In order to achieve n-type conductivity, the layers were doped with chlorine which is known to form shallow donor levels with an ionization energy of $E_\mathrm{i} = 26\,\mathrm{meV}$ [120, 121]. The epitaxial layers had a thickness of $1\,\mu m$. The manganese concentration in all four samples was fixed to 6% and the four samples presented here varied in chlorine concentration only. The four samples can be divided into two groups. The first group consists of two epitaxial layers with free carrier concentrations of $3.4 \times 10^{17}\,\mathrm{cm}^{-3}$ and $4.5 \times 10^{17}\,\mathrm{cm}^{-3}$. These samples show clearly activated behavior at low temperatures with activation energies of 0.51 meV and 0.28 meV and mobilities below $10\,\mathrm{cm}^2/\mathrm{Vs}$, typical for hopping in an impurity band, and will therefore be regarded as '*hopping samples*'. The remaining two samples, representing the second group, have much higher carrier concentrations of $4.9 \times 10^{18}\,\mathrm{cm}^{-3}$ and $8.2 \times 10^{18}\,\mathrm{cm}^{-3}$ and show clearly metallic transport behavior with high mobilities above $200\,\mathrm{cm}^2/\mathrm{Vs}$ even at the lowest temperatures due to transport in extended states. They will be named '*metallic samples*' in the following.

Figure 6.1 shows the magnetoresistance curves at various temperatures of the four (Zn,Mn)Se:Cl samples under study. It becomes evident that there are well pronounced differences between the two sample groups. In the case of the hopping samples, relatively low magnetic fields are sufficient to boost the resistivity at 1.6 K by more than 1500%. At low temperatures, the resistivity goes through a maximum, before it slowly decreases at high fields and saturates. The steep rise at low fields is significantly weakened at slightly higher temperatures, shifting the maximum towards higher magnetic fields. Simultaneously, the negative contribution loses strength with increasing temperature very quickly and vanishes at approximately 10 K. The observed increase of the resistivity at low fields is found in the metallic samples as well, but obviously the magnitude of the effects differs considerably, as the positive magnetoresistance in this case does not exceed 2%. At elevated temperatures, the magnetoresistance curves show a complex interplay between weak positive and negative contributions.

The results of the measurements of the hopping samples bring up two questions. The most striking one is that of the origin of the strong positive magnetoresistance at low temperatures. It has been found in other II-Mn-VI compounds with similar Mn concentrations and for carrier concentrations below the metal-insulator transition. A comparison of the magnetoresistance results obtained for the magnetic compounds and its non-magnetic pendants (e.g. (Cd,Mn)Se and CdSe in [122]) clearly shows the magnetic origin of the effect, as it cannot be observed in the latter case. For $Cd_{0.95}Mn_{0.05}Se$ and $Cd_{0.95}Mn_{0.05}Te$, Shapira et al. find that the increase of the resistivity is correlated with the samples magnetization and they conclude that s-d interaction is responsible for the observed effects [123–125]. The authors propose a mechanism of redistribution of electrons between the two spin polarized conduction subbands. They claim that in their samples the Fermi level lies inside the conduction band. The band splitting due to eq. 6.4 leads to a redistribution of electrons between the two spin

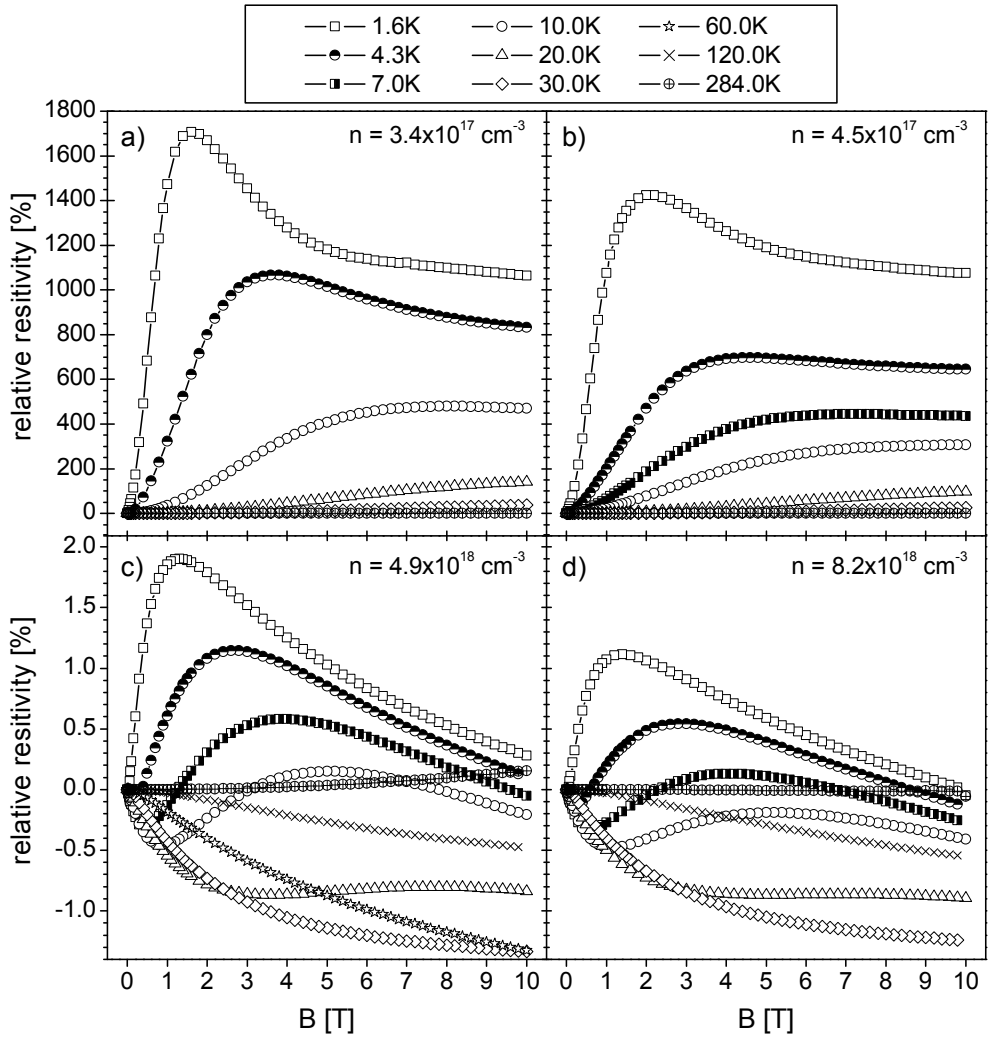

Figure 6.1: Magnetoresistance curves of the four $Zn_{0.94}Mn_{0.06}Se$:Cl epitaxial layers for various temperatures. Whereas the hopping samples (a) and (b) show large relative changes of the magnetoresistance of the order of 1000% at low temperatures (see text), the resistivity of the metallic samples (c) and (d) hardly changes by more than 1%. Also, the effects in the hopping case are strongly temperature dependent.

subbands, raising the Fermi level E_F^+ in the majority spin subband and lowering E_F^- in the other subband. It is further argued that this effect in turn increases scattering by ionized impurities which depends, in part, on the screening of the Coulomb potential of these impurities. In the Thomas-Fermi approximation, the screening radius is a function of the density of states at the Fermi energy, summed over both spin subbands. As the conduction band splits, the redistribution of electrons between the two subbands produces a change of $N(E)$ at E_F. Shapira et al. estimate for a parabolic band that the spin splitting leads to an increase of the screening radius which implies weaker screening and stronger scattering.

Still, this argumentation has an important shortcoming, as it is based completely on the assumption of a metallic transport regime and neglects the presence of an impurity band. Therefore, the explanation does not hold for the (Zn,Mn)Se hopping samples studied here as stated at the beginning[2]. Quite the contrary is the case, since the Fermi level lies in a region of localized impurity states. For the metallic samples, where the argumentation would be valid, the magnetoresistance effects are very weak. Thus, the model to explain the experimental results for the low doped samples must be based on the assumption of hopping conduction.

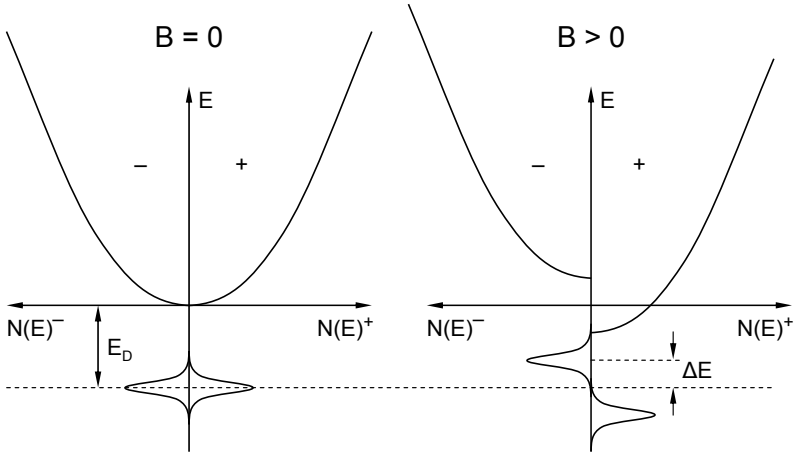

Figure 6.2: Schematic illustration of the spin splitting of the impurity band in one electron approximation. The two sides in the energy diagram correspond to different spin orientations.

Let us first consider a scenario of nearest neighbor hopping. The mechanism to explain the strong increase of the resistivity at low fields is motivated by the work of H. Kamimura [126] and will be described in the following. It is based on the assumption that both singly occupied and doubly occupied donor levels coexist at the Fermi level.

Usually, the Coulomb repulsion avoids doubly occupied impurity sites, i.e. the two Hubbard subbands are well separated, and transport in an impurity band happens due to hopping towards empty (either ionized or compensated) localized states. However, in $Zn_{0.94}Mn_{0.06}Se$ the impurity band can be assumed to be broadened due to statistical fluctuations of the Mn concentration. For an ionization energy of the chlorine donors of 26 meV, the effective Bohr radius can be estimated as $a_B \simeq 3\,\mathrm{nm}$. With a Mn concentration of 6%, the localization radius of a single donor covers approximately 150 Mn ions. Because the Mn ions are statistically distributed in the crystal, the local Mn concentration x differs for each impurity atom. Since the energy of the bandedge E_C of $Zn_{1-x}Mn_xSe$ and other II-Mn-VI compounds increases with x (in the case of (Zn,Mn)Se for

[2]This assumption is at least not totally fulfilled for Shapira's samples either, because the (Cd,Mn)Se and (Cd,Mn)Te samples with well pronounced positive magnetoresistance effect showed clearly defined hopping energies indicating impurity band transport.

$x > 4\%$), local variations of x translate into local variations in E_C, resulting in a broadening of the impurity band. One can propose that this leads to an overlap of the two Hubbard bands and both singly occupied and doubly occupied donor levels coexist at the Fermi level. With an applied magnetic field, the spin-splitting (eq. 6.4) does not only influence the band states, but leads to a splitting of the impurity band as well (as schematically shown in fig. 6.2), since the shallow impurity wavefunctions originate from states at the conduction band edge. This changes the energetic situation for doubly occupied sites, because the two spin states now differ in energy due to the s-d-interaction. For doubly occupied sites, this mechanism works in the same direction as the Coulomb repulsion, making those less likely to occur with increasing magnetic field. As a consequence, this reduces the number of possible hopping sites and increases the resistivity. As the s-d-splitting is very strong, relatively weak magnetic fields of approximately 2 T are sufficient to completely separate the two impurity subbands of different spin orientation and the positive effect saturates quickly.

In the case of the metallic samples, the Fermi level lies inside the conduction band and the situation in the impurity band does not affect the transport any more. In this regime other models may be valid, as described above.

In the case of nearest neighbor hopping an analysis of the activation energies should be informative. Figure 6.3 depicts the activation energies extracted from

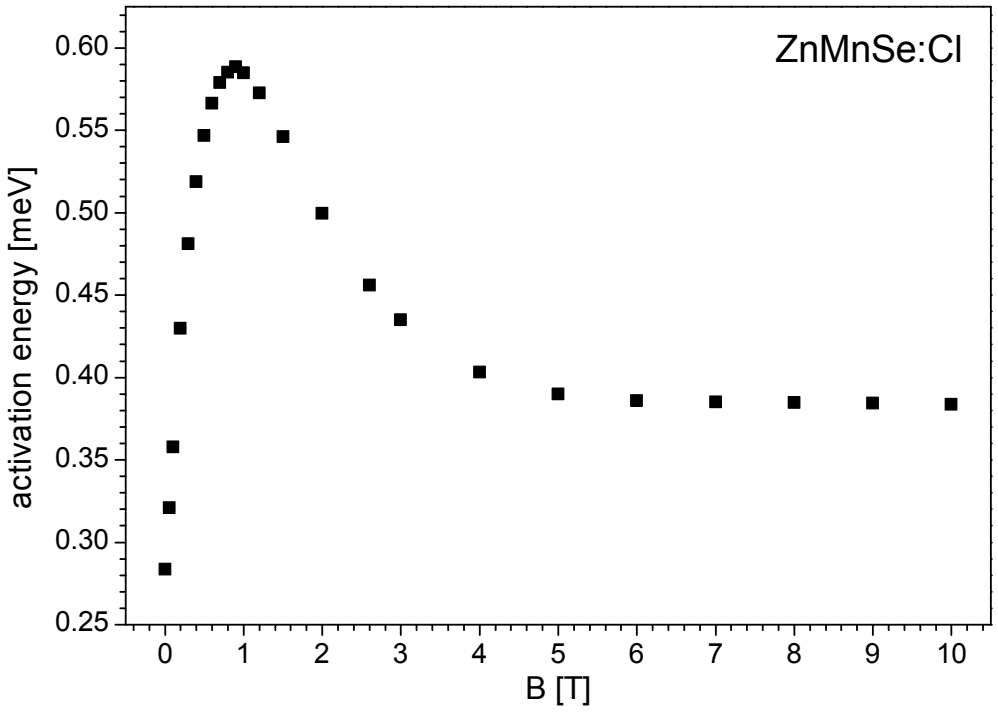

Figure 6.3: Magnetic field dependence of the activation energy for the hopping sample with $n = 4.5 \times 10^{17}\,\mathrm{cm}^{-3}$, as determined from $\rho(1.6\,K < T < 4\,K, B)$.

the temperature dependence of the resistivity (in the range of 1.6 – 4 K) at different magnetic fields. Starting with a value of 0.3 meV at $B = 0\,\mathrm{T}$, the activation energy is doubled, as B increases to $B = 1\,\mathrm{T}$, then slightly decreases and saturates at high fields. The qualitative behavior resembles that of the resistivity curves.

However, such complex behavior of the activation energy is difficult to explain. Furthermore, there remain other open questions. The most striking one addresses the strength of the Coulomb repulsion. Typical binding energies for doubly occupied donors are of the order of $0.1E_{\mathrm{D},0}$ with $E_{\mathrm{D},0}$ being the donor ionization energy [12]. Thus, singly and doubly occupied states can be assumed to be separated by an energy of $\approx 20\,\mathrm{meV}$, which is in contradiction to the assumption of overlapping Hubbard bands, as mentioned above. Additionally, the scenario of nearest neighbor hopping is in question. Since the hopping samples are well on the insulating side of the metal-insulator transition ($Na_{\mathrm{B}}^3 \approx 0.002$), one would expect much higher activation energies than those measured. Unfortunately, from the experimental data, one is not capable to distinguish between nearest neighbor hopping ($\ln(\rho) \propto T^{-1}$) and variable range hopping ($\ln(\rho) \propto T^{-1/4}$) because of a lack of sufficient data at low temperatures. Therefore, the interpretation of the data as activated transport (fig. 6.3) might be wrong.

These concerns render the scenario of variable range hopping much more likely than that of nearest neighbor hopping. However, the most important ingredient, namely the spin splitting in a magnetic field (fig. 6.2), remains unaffected. The resistivity in the variable range hopping regime depends on the density of states at the Fermi level $g(\mu)$ via T_0 (eq. 3.10). Without magnetic field these states are spin degenerate. The spin splitting of the donor impurity band due to the magnetic field removes this degeneracy, decreases the density of states and decreases the transition probabilities. It is important to note that, no matter which one of the two hopping scenarios is adequate here, the explanation of the positive contribution to the magnetoresistance must be related to spin selection effects. Thus, the transport scenario discussed here goes beyond current theoretical models for hopping transport, as those do not account for spin effects.

The second question brought up by the experimental results addresses the negative contribution that dominates at high magnetic fields. Also, the effect responsible for the negative magnetoresistance is related to disorder as well as the s-d-exchange splitting and works in intermediate magnetic fields. As explained above, fluctuations in the Mn concentration lead to a broadening of the impurity band and a magnetic field splits the impurity band into two subbands for the two spin orientations. However, this spin splitting $\Delta E_{\text{s-d}}$ is larger for higher Mn concentrations, as it linearly depends on x_{eff}. Simply speaking, as the magnetic field increases, the higher energy donor levels will catch up with those of lower energy. As a direct consequence, the width of the lower impurity spin-subband shrinks slightly, improving the conditions for hopping conduction, since the spatial distance of states with the same energy (i.e. within $k_{\mathrm{B}}T$), a quantity that

exponentially influences the resistivity, is reduced. This effect saturates with the Brillouin function in eq. 6.4 which takes place at higher fields than at the maximum of $\rho(B)$.

In order to provide a quantitative estimate for the strength of this effect, a simple calculation of the distribution of donor levels under an applied magnetic field was carried out. According to eqs. 6.4 and 6.6, the donor energies in the two impurity subbands are

$$\begin{aligned} E_{\mathrm{D},\,s_z}(x,B,T) &= E_{\mathrm{C}}(x) - E_{\mathrm{D},0} \\ &\quad + \hat{g}\mu_{\mathrm{B}} s_z B - N_0 \alpha x_{\mathrm{eff}} s_z S B_{5/2}\left(\frac{g\mu_{\mathrm{B}}\frac{5}{2}B}{k_{\mathrm{B}}(T+\theta(x))}\right) \end{aligned} \tag{6.7}$$

with $s_z = \pm\frac{1}{2}$. For the calculation the following numerical values were used: $E_{\mathrm{D},0} = 26\,\mathrm{meV}$ [120, 121], $g = 2$, $N_0\alpha = 0.26\,\mathrm{eV}$ [127], $\hat{g} = 1.1$ [128], $E_{\mathrm{C}}(x)$ from [129], $x_{\mathrm{eff}}(x)$ and $\theta(x)$ from [130][3].

The histograms of fig. 6.4 are derived from the calculated values of E_{D} weighted by their individual statistical probability for $x_{\mathrm{mean}} = 0.06$. It can be seen that the dependence of the conduction band edge on x leads to the broadening of the donor energies as mentioned. It must be emphasized that the simple calculation takes only disorder induced broadening into account and can only be regarded as a simple estimation. With increasing magnetic field, the impurity band states split. At 1 T, the two subbands are well separated, giving rise to the strong increase of the resistivity, since doubly occupied states are not allowed any more. Simultaneously, the width of the two subbands changes. Whereas the upper one increases in width, that of the lower subband decreases with increasing field strength. At 10 T, the size of the effect is approximately 25%. This result of course depends critically on the assumed parameterizations, especially on $E_{\mathrm{C}}(x)$ and $x_{\mathrm{eff}}(x)$. For instance, a less pronounced increase of E_{C} with x would increase the relative shrinkage of the band. Detailed theoretical modeling has to be performed in order to decide whether or not the described disorder effects are sufficient to explain the decrease of the resistivity at intermediate fields.

Conclusions

The transport experiments on (Zn,Mn)Se:Cl show well pronounced magnetoresistivity effects for doping concentrations below the metal-insulator transition similar to other II-Mn-VI semiconductors. For metallic samples, these variations

[3] The dependence of the quantities $E_{\mathrm{C}}(x)$, $x_{\mathrm{eff}}(x)$ and $\theta(x)$ on the concentration x was represented by the relations
$E_{\mathrm{C}}(x)/\mathrm{eV} = 2.802 - 0.07487\,x + 4.89058\,x^2 + 17.18963\,x^3 - 311.31541\,x^4$,
$x_{\mathrm{eff}}(x) = +0.56103\,x - 2.80685\,x^2 + 3.88871\,x^3$ and
$\theta(x)/\mathrm{K} = 15\,x$
which give a good parametrization for the concentration range below 10%.

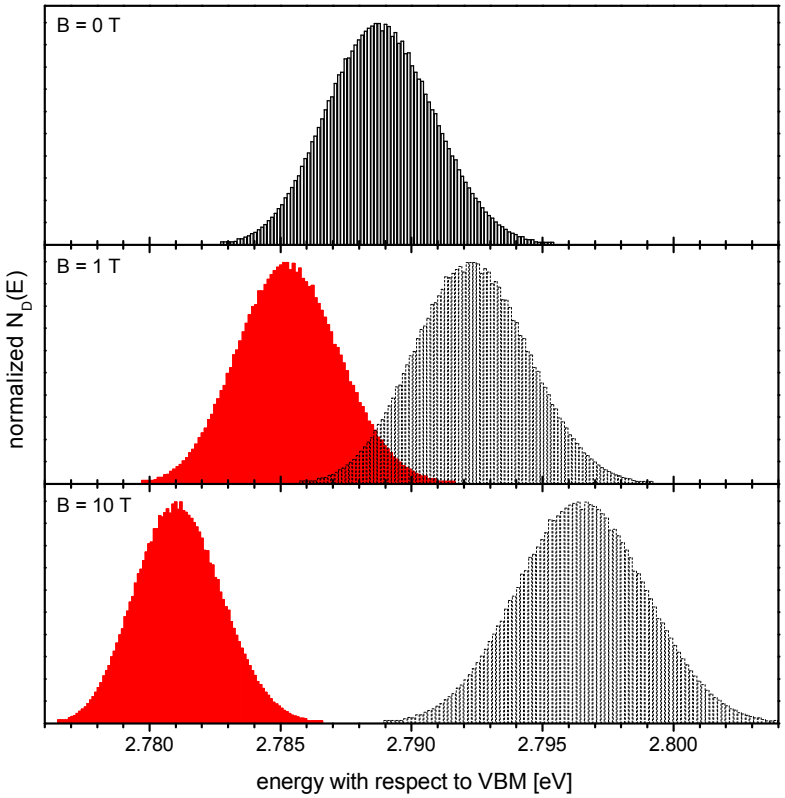

Figure 6.4: Distribution of donor energies of the two donor spin-subbands. At a magnetic field of 1 T, the two subbands are well separated. At high magnetic field, the width of the lower energy subband is considerably smaller than that of the upper one and smaller than the one for $B = 0$.

of the magnetoresistance are almost negligible. They can be explained qualitatively taking into account magnetic interactions between free carriers and localized magnetic moments of Mn ions as well as disorder effects. A variable range hopping scenario at low temperatures appears most likely. The strong positive magnetoresistance at low magnetic fields can be understood as a consequence of the decrease of the density of states at the Fermi level due to s-d-splitting of the donor states. Fluctuations in the Mn concentration are regarded as the origin for the negative magnetoresistance at high magnetic fields. Further experimental work has to be done including a detailed analysis of the temperature dependence of the resistivity at low temperatures in order to clarify the transport mechanism. As well, theoretical modeling is required to explore the situation and to clarify, if the proposed mechanisms withstand a real quantitative analysis.

6.2 Influence of magnetic dopants on the metal-insulator transition in semiconductors

So far, the theories describing the metal-insulator transition, such as the Hubbard model or the Anderson model (section 3.2, p. 26), make no distinction between magnetic (e.g. Mn) and non-magnetic impurities (e.g. Ge). However, it can be anticipated that in the case of magnetic impurities additional correlation effects, such as the exchange interaction between the localized magnetic moment of the $3d^5$ shell of the Mn acceptor and the magnetic moment of the acceptor hole, will have a significant impact on the transport behavior at the metal-insulator transition.

In this section, the transport behavior of InSb doped with non-magnetic Ge and that of InSb doped with magnetic Mn will be compared. Both Mn and Ge form shallow acceptor levels in InSb with identical acceptor activation energies of $\varepsilon_{1,\mathrm{Mn}} = \varepsilon_{1,\mathrm{Ge}} = 9.5\,\mathrm{meV}$ [131, 132]. Consequently, the metal-insulator transition occurs at the same critical impurity concentration of $N_{\mathrm{cr}} = N_{\mathrm{Ge}} = N_{\mathrm{Mn}} \approx 2 \times 10^{17}\,\mathrm{cm}^{-3}$ and the two systems are directly comparable. Any differences in their transport properties can be related to the different magnetic nature of the impurities. It is important to note that the magnetic impurity Mn serves both as the source of a large localized magnetic moment due to its half filled inner 3d-shell and as the source of a loosely bound hole due to its acceptor character. It will be demonstrated that magnetic impurities such as Mn provoke dramatical changes in the character of the metal-insulator transition which need to be accounted for in respective theories.

InSb - sample characteristics

The InSb crystals were grown by the Czochalsky method. The samples ($3 \times 1 \times 0.5\,\mathrm{mm}^3$ in size) were cut from single crystal ingots perpendicular to the growth axis to minimize the impurity-concentration gradient along their length. Before the transport measurements, the samples were etched in a solution of nitric acid HNO_3, hydrofluoric acid HF and acetic acid CH_3COOH (5:3:3) for 3–5 seconds in order to remove any conductive oxidation layer that may have possibly built up after growth. Ohmic contacts were immediately attached to the cleaved faces of the samples with indium solder. The measurements under hydrostatic pressure were performed in the non-magnetic clamp pressure cell described in section 2.5. Within the available pressure range of the cell, no structural phase transitions are to be expected [133]. Resistivity and Hall effect have been measured either in van der Pauw or Hall bar geometry. No distinct differences have been found between these two contact methods. In total, fifteen InSb samples were studied and three among them were selected for measurements under hydrostatic pressure. These were one sample of InSb:Ge (No. 250-3) and two samples of InSb:Mn (No. 459-3-3 and 459-11-1). Since the two manganese doped samples

showed very similar results with only minor quantitative differences, but identical qualitative behavior, only one of them will be considered in the following discussion.

Differences in the transport behavior induced by the magnetic nature of shallow impurities

Figure 6.5 displays the dependence of the resistivity on temperature (6.5 a) and hydrostatic pressure (6.5 b) of both InSb:Mn and InSb:Ge with $N_{\mathrm{cr}} \approx 2 \times 10^{17}\,\mathrm{cm}^{-3}$. In fig. 6.5 a, for each sample three curves are shown corresponding to different values of the applied hydrostatic pressure. At ambient pressure, both InSb:Ge and InSb:Mn exhibit metallic behavior, i.e. constant resistivity at low temperatures. In the case of InSb:Ge, pressure-induced changes are negligible at high temperatures and only a minor increase of the resistivity with pressure is observed at 1.6 K. The general qualitative behavior of $\rho(T)$ does hardly change by applying hydrostatic pressure. In the case of InSb:Mn, applying pressure also does not influence the resistivity at room temperature, but causes significant changes at low T (fig. 6.5 b). A huge increase of the resistivity at 1.6 K by more than four orders of magnitude occurs with increasing pressure, leading to a rise of the activation energy from 0.1 meV at ambient pressure to 1.6 meV at 12 kbar. This is a first indication of a completely different transport situation at low temperatures in samples doped with *magnetic* impurities compared to those doped with conventional *non-magnetic* impurities.

The magnetoresistance measurements yield differences of similar distinctness at

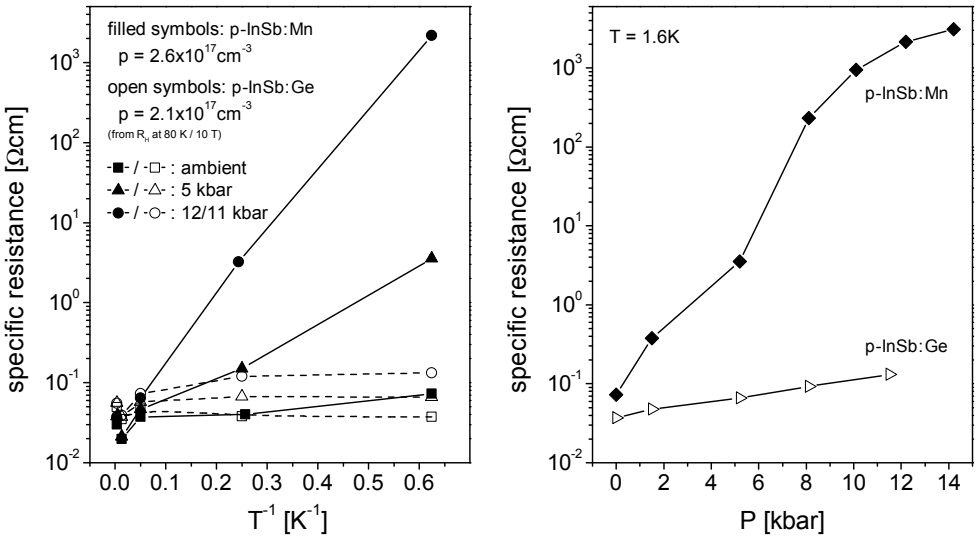

Figure 6.5: a) Arrhenius-plot of the resistivity for InSb:Mn and InSb:Ge crystals for various hydrostatic pressures (ambient, 5.2 kbar both InSb:Mn and InSb:Ge, 12.2 kbar and 11.1 kbar for InSb:Mn and InSb:Ge, respectively). InSb:Mn shows a dramatic increase of the activation energy in contrast to InSb:Ge. b) Pressure dependence of the resistivity of InSb:Mn and InSb:Ge crystals at $T = 1.6\,\mathrm{K}$.

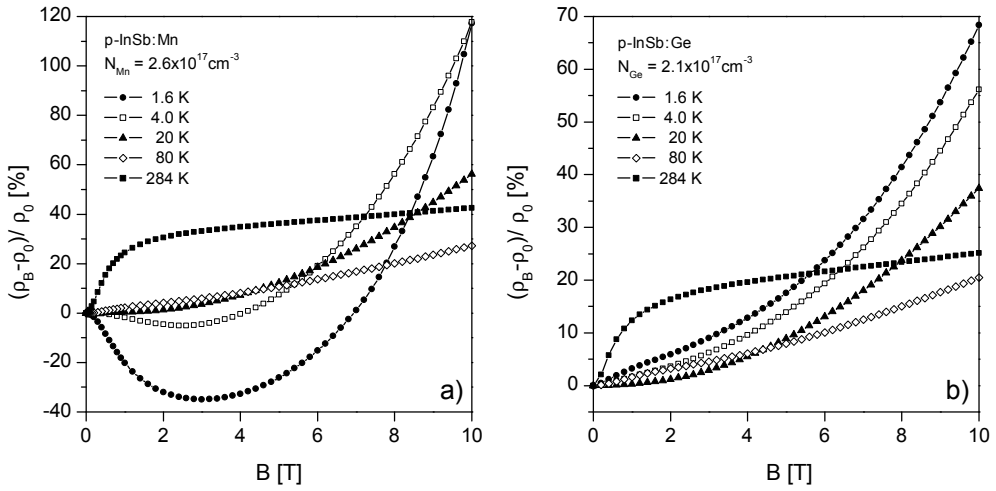

Figure 6.6: Relative magnetoresistance curves of both InSb:Mn and InSb:Ge at various temperatures. Distinct differences occur at low temperatures only.

low temperatures. In the case of Ge doping (fig. 6.6 b), a small positive magnetoresistance effect is observed at 1.6 K. In contrast, large negative magnetoresistance effects dominate the curves for InSb:Mn (fig. 6.6 a). The sample shows a very large negative magnetoresistance effect with a minimum of the relative magnetoresistance of -35% at 3 T. At higher magnetic fields, positive magnetoresistance is observed most likely due to the normal quadratic contribution. Influences of wavefunction shrinkage is not likely since the magnetic fields can still be regarded as being small since $H_C \approx 13\,\mathrm{T}$ in this case (using eq. 4.2). It is important to note that the differences between the two samples are restricted to the low temperature range only. At higher temperatures, i.e. above 10 K, the magnetoresistance curves are very similar. For this reason, the following considerations will focus on the low temperature regime.

Under hydrostatic pressure the magnetoresistance curves of InSb:Ge remain positive and do not change significantly in magnitude (fig. 6.7 b), whereas in the case of InSb:Mn, the negative contribution becomes even more pronounced up to 8 kbar with a minimum of -97% (fig. 6.7 a). Simultaneously, the positive contribution loses strength or is shifted towards higher magnetic fields, as no significant positive magnetoresistance is found up to 10 T. With even higher hydrostatic pressure, the negative magnetoresistance becomes less pronounced again and the steep decrease of the resistivity at low fields is smeared out. Still only a very weak positive magnetoresistance is found up to 10 T.

At slightly elevated temperatures, the effects of hydrostatic pressure vanish, as depicted in fig. 6.8 which shows data taken at $T = 20\,\mathrm{K}$. Here, the absolute value of the resistivity is plotted versus magnetic field squared for various values of the applied pressure. The resistivity hardly changes with applied pressure and the linear curves indicate the normal quadratic dependence $\rho(B) \propto B^2$.

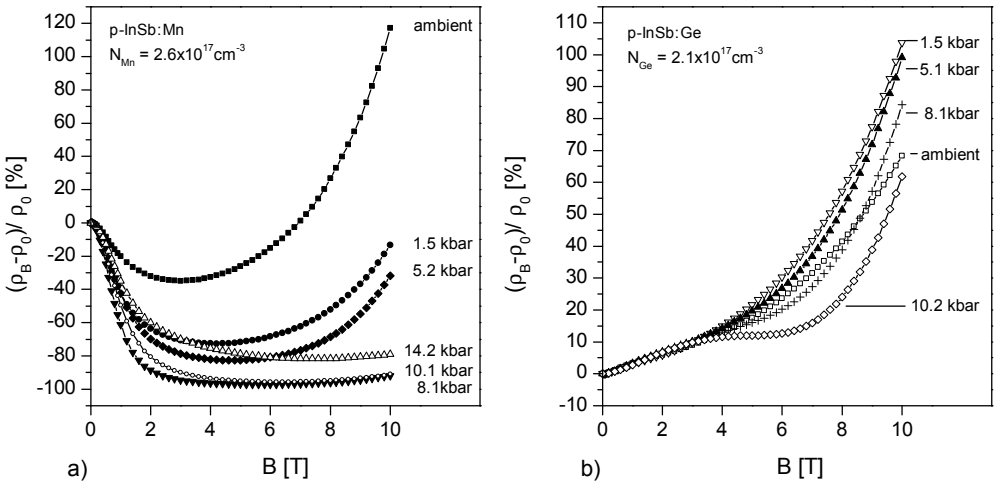

Figure 6.7: Magnetoresistance in p-InSb:Mn and p-InSb:Ge as a function of magnetic field shown for various pressures at $T = 1.6\,K$.

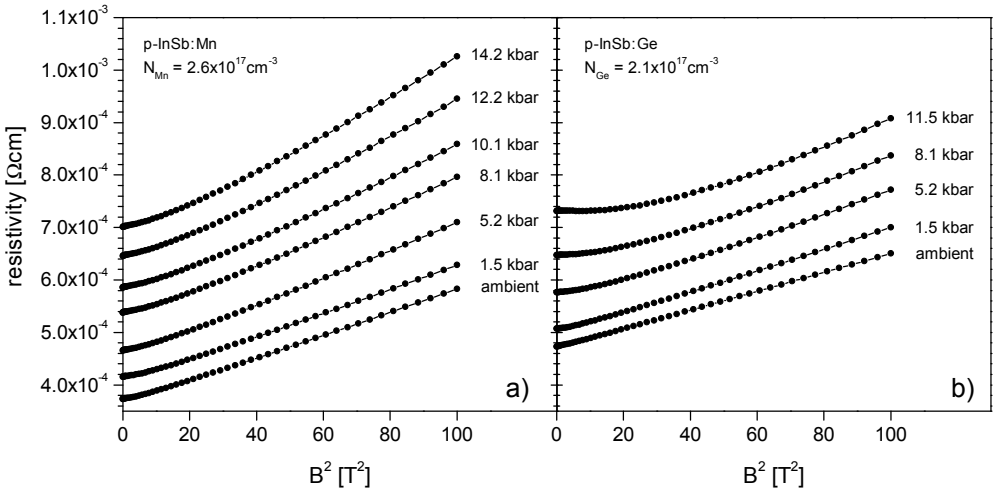

Figure 6.8: Resistivity versus B^2 at $T = 20\,\mathrm{K}$ for both InSb:Mn and InSb:Ge at various hydrostatic pressures. The results do not show any of the unusual magnetoresistance effects visible at low temperature, but obey normal quadratic behavior.

In conclusion, the magnetotransport measurements reveal well pronounced differences between magnetic and non-magnetic impurities. These differences are restricted to the low temperature regime. The extremely strong negative magnetoresistance effects of InSb:Mn are too large to be explained by standard theories of magnetoresistance (weak Anderson localization [14, 61] or spin dependent hopping [84]) and do not arise in Ge doped InSb. Therefore, the origin of the effect has to be connected to the magnetic nature of the Mn impurities.

The interaction of free hole spins and localized magnetic moments

A qualitative explanation of these unusual transport properties in InSb:Mn can be given in the Mott picture [21] accounting for additional correlation effects due to the p-d exchange between the localized Mn $3d^5$ spins and the hole spins of the Mn acceptor. At the metal-insulator transition, a significant overlap of the wave functions of neighboring acceptors can be assumed and the hole transport follows a percolation path through the acceptor system, as described in section 3.2. The situation along the percolation path corresponds to the transport along a one-dimensional chain of impurity atoms. Since the acceptor wave functions are symmetric in space, the significant overlap between the wave functions of acceptors forces an antiparallel alignment of the hole spins of neighboring acceptors and the system forms an antiferromagnetic insulator [21]. This is the case for both Mn and Ge doped InSb (see fig. 6.9 a).

The difference between the two systems arises due to the additional p-d exchange coupling of the Mn localized magnetic moment and the spin of the hole localized at a Mn site. This coupling has two consequences: First, if the temperature is low enough, the antiferromagnetic order of the hole spins on neighboring Mn sites leads via p-d coupling to an antiferromagnetic order of the localized Mn $3d^5$ spins along the acceptor chain. The antiferromagnetic alignment of neighboring $S = 5/2$ spins is mediated through the localized holes[4]. Secondly, the p-d coupling lifts the spin degeneracy of acceptor levels, i.e. the energy level of the hole will depend on the relative orientation of its spin to that of the localized $S = 5/2$ Mn $3d^5$ spin. The corresponding spin Hamiltonian of the form $H_{\mathrm{p-d}} = -J_{\mathrm{p-d}}\vec{S} \cdot \vec{s}$ leads to the exchange splitting Δ of the acceptor hole levels (see Fig. 6.9 b), where $J_{\mathrm{p-d}}$ is the p-d exchange constant, $\vec{S}$ and $\vec{s}$ are the localized Mn $3d^5$ spin and the hole spin, respectively. The p-d exchange splitting Δ is much larger than the effects due to hole-hole interaction. The corresponding energy states are defined locally, with the low energy state given by an antiparallel alignment of hole and Mn spins and a high energy state characterized by parallel alignment. This corresponds to an antiferromagnetic coupling $J_{\mathrm{p-d}} < 0$, as reported by Schneider et al. [134] for GaAs:Mn and by Kudelski et al. [135] for InAs:Mn[5]. These authors report typical values $|J_{\mathrm{p-d}}|$ of about 1 meV which is also the order of magnitude of the exchange splitting Δ. The activation energies E_{A} which are observe in InSb:Mn, but not in InSb:Ge, are also in this range (see discussion of fig. 6.5). Below the Néel temperature, the transport path in InSb:Mn at the metal-insulator transition is along an antiferromagnetically ordered chain of Mn spins. The hole states of the same spin orientation on neighboring Mn sites of the chain will differ by the p-d exchange splitting $\Delta \gg k_{\mathrm{B}}T$ and thus inhibit hopping between these states. In InSb:Ge, neglecting hole-hole correlations, the two hole states on the acceptor will be degenerate. Obviously, the hole-hole correlation as an on-site interaction

[4] This must not be mistaken with the RKKY interaction between two Mn ions which is mediated by a free carrier plasma.

[5] Our discussion is independent of the sign of $J_{\mathrm{p-d}}$.

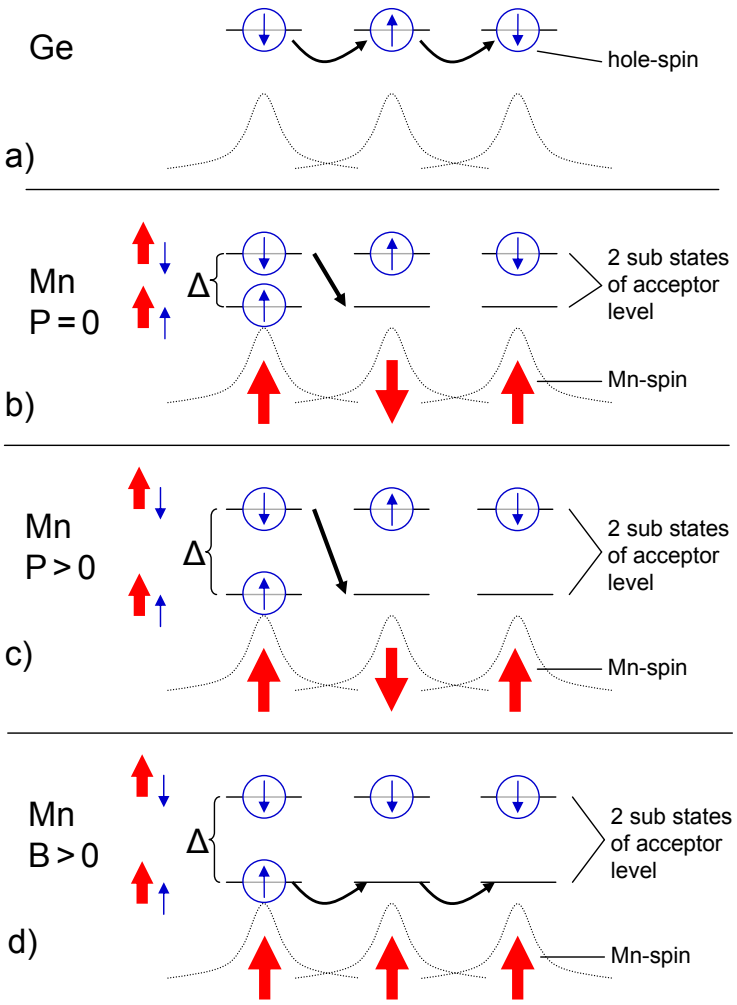

Figure 6.9: Schematic illustration of hopping between impurity levels in a) InSb:Ge where no splitting takes place and in b)–d) InSb:Mn where the impurity level is split into two substates due to the magnetic interaction. Note that the corresponding energy states are defined locally, with the low energy state given by an antiparallel alignment of hole and Mn spins and a high energy state characterized by parallel alignment. The different subfigures represent the situations of b) InSb:Mn at zero magnetic field and ambient pressure c) InSb:Mn under the influence of hydrostatic pressure (with increased splitting) and d) InSb:Mn with applied magnetic field (ferromagnetic alignment of the magnetic moment)

only slightly lifts this degeneracy. The corresponding splitting is much smaller than the p-d-exchange induced splitting Δ. Therefore, hopping along the Ge chain will be much easier than along a Mn chain.

Crucial for the differences in transport between a Mn and Ge chain is the establishment of the antiferromagnetic order of the Mn $3d^5$ spins along the chain. This antiferromagnetic ordering requires low temperatures, because above the

corresponding Néel temperature, the $3d^5$ Mn spins are randomly arranged and hopping between neighboring Mn ions is no longer fully inhibited. This explains why the transport results of InSb:Mn and InSb:Ge differ significantly at low temperatures $T < T_N$ only. In this case, the activation energy E_a in InSb:Mn is of the order of the exchange splitting Δ.

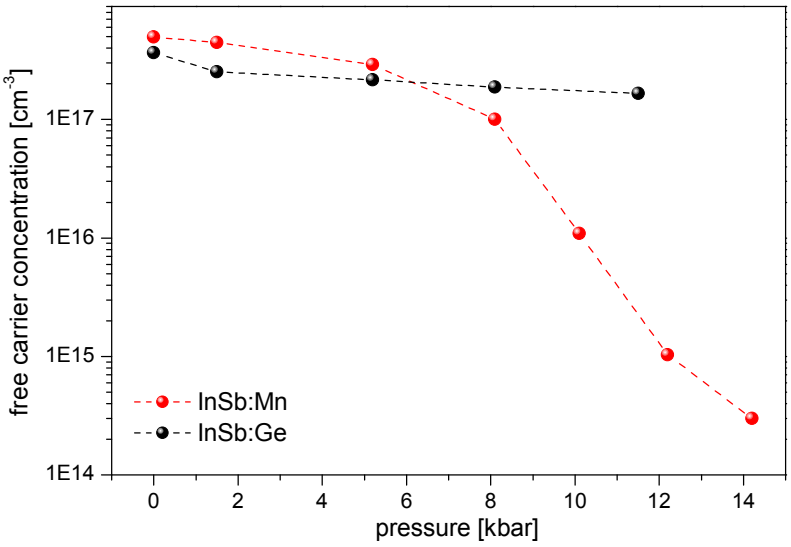

Figure 6.10: Pressure dependence of the free carrier concentration at 1.6 K of both samples. This quantity strongly decreases for InSb:Mn, whereas it hardly changes for InSb:Ge.

Within the picture described above, one can also explain the observed dependence on hydrostatic pressure (see fig. 6.9 c) and on magnetic field (see fig. 6.9 d). Hydrostatic pressure leads to an increase of T_N. It compresses the crystal, enhancing the wave-function overlap of holes located at neighboring impurity sites and also enhancing exchange coupling J_{p-d}, leading to an pressure-induced increase of Δ which is reflected in the increase of E_a in InSb:Mn under pressure and a corresponding strong reduction of the number of free holes (determined by Hall measurements) which is not observed in InSb:Ge (see fig. 6.10). For example, the p-d exchange between localized Mn spins and free hole spins in (Zn,Mn)Te increased linearly by almost 70% by increasing hydrostatic pressure from ambient conditions to 30 kbar [136].

By applying an external magnetic field, the antiferromagnetic ordering of the Mn $3d^5$ spins can be overcome and a ferromagnetic alignment may be established (fig. 6.9 d). Consequently, an additional (spin-up) hole on a Mn site finds unoccupied spin-up hole states of the same energy on the neighboring sites (in contrast to the situation without magnetic field, fig. 6.9 b, c), allowing for hopping between sites of equal energy. With increasing magnetic field the situation changes from that described in fig. 6.9 b to that depicted in fig. 6.9 d, i.e. from hopping with an activation energy of Δ to hopping with zero activation energy. Consequently, one observes a negative magnetoresistance effect with increasing magnetic field which saturates at higher field. As Δ increases with hydrostatic

pressure, the corresponding negative magnetoresistance must also increase as observed in the experiment. In InSb:Ge none of the mentioned effects is present due to the nonmagnetic nature of Ge.

The magnitude of the negative magnetoresistance effect depends on how well antiferromagnetic ordering is established. Perfect ordering relates to the maximum difference between zero and applied field. It can be speculated that a compression of the crystal results in an increase of the antiferromagnetic coupling and thus to an increased negative magnetoresistance up to a point of saturation where antiferromagnetic ordering cannot be significantly enhanced anymore. This is in concordance with experiment where a maximum of negative magnetoresistance is observed at 8 kbar. Even higher pressure may result in a stabilization of antiferromagnetic ordering which manifests itself in the fact that the sharp decrease of the resistivity at low pressure is smeared out and the minimum of the curves is shifted towards higher magnetic fields, as the pressure is increased above 8 kbar. Further indication can be found in the fact that the negative magnetoresistance is more stable with increasing temperature at 14 kbar than at 10 kbar, as depicted in fig. 6.11.

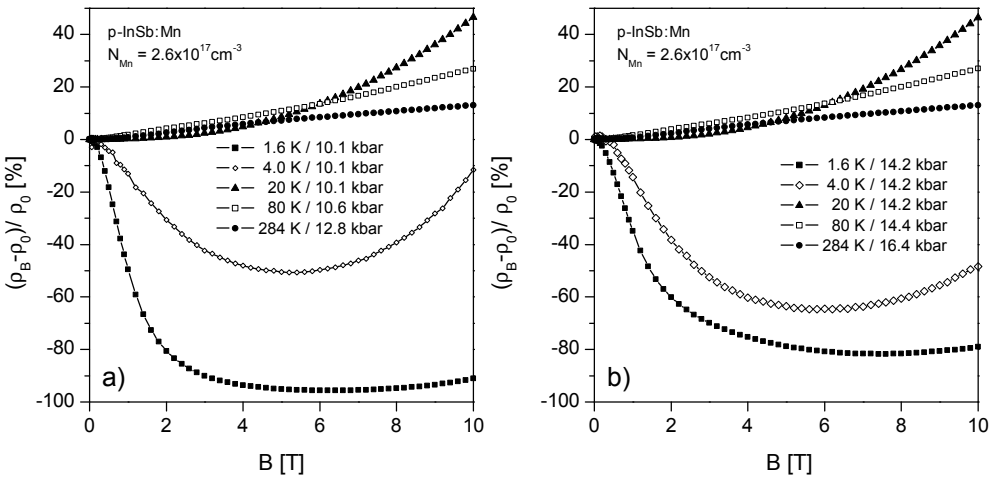

Figure 6.11: Magnetoresistance at a) 10 kbar and b) 14 kbar for various temperatures.

Furthermore, it should be noted that the differences in electric transport of InSb:Mn and InSb:Ge are most pronounced in the vicinity of the metal-insulator transition [137], as displayed in fig. 6.12. The reasons are the following: For $N_{\mathrm{Mn}} \ll N_{\mathrm{cr}}$, no continuous percolation path consisting of overlapping Mn acceptor wave functions is formed as the main transport path. Thus, no fully antiferromagnetically ordered Mn chain is established, which was the prerequisite for the observed effects. For $N_{\mathrm{Mn}} \gg N_{\mathrm{cr}}$, a Mn ion along the transport path is likely to have more than two Mn neighbors with overlapping acceptor wave functions. Due to competing interactions between Mn spins, the formation of the one-dimensional antiferromagnetically ordered Mn chain will also be perturbed, leading again to a degradation of the corresponding transport effects compared to the situation close to the metal-insulator transition.

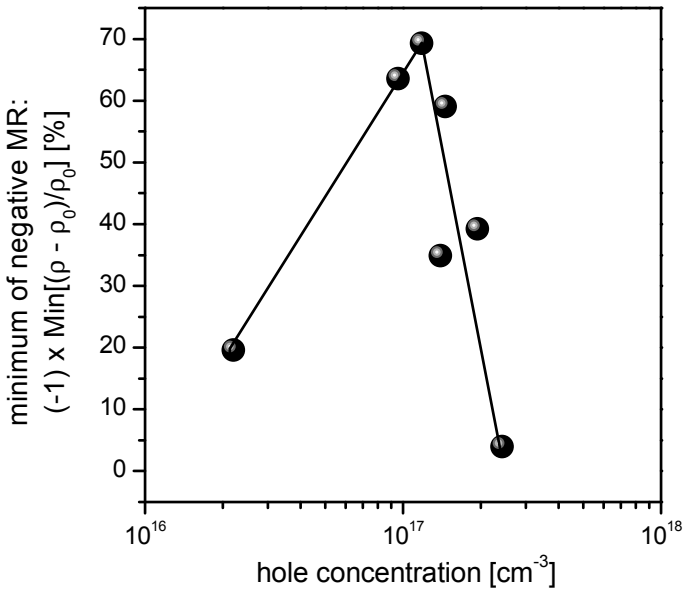

Figure 6.12: Dependence of negative magnetoresistance effects on Mn content.

Conclusions

It was proved that magnetic dopants can significantly influence the metal-insulator transition in semiconductors. Correlation effects between the localized magnetic moments and the loosely bound carriers of the magnetic dopant can be significantly stronger than on-site carrier-carrier correlations, leading to new interesting phenomena in an area between magnetism and semiconductor physics.

7 Overall conclusions

One characteristic property of semiconductors is their sensitivity to impurity atoms. As a consequence, the transport mechanisms at low temperature are governed by a strong interplay between localized states of impurities and extended band states. Within the present work, several mechanisms of those interactions have been addressed in a doping regime close to the metal-insulator transition.

The isovalent-trap character of boron impurities in GaAs has been analyzed in a study of the transport properties of (B,Ga,In)As. It was found that B impurities significantly influence the transport properties of (B,Ga,In)As as compared to n-GaAs. Measurements under hydrostatic pressure proved to be very useful, as they revealed the trap character of B localized states. Under pressure this leads to a draining of the reservoir of electrons originating from Si donors into localized B states. All other experimental findings follow from the resulting decrease of the Fermi energy. The hydrostatic pressure experiments allowed to perform transport spectroscopy to experimentally determine the density of B-related states near the conduction band edge. The results from this analysis are in concordance with theoretical tight binding calculations. Thus, despite the complexity of the system, the experimental results are well understood. Further research could be done by investigating samples with different B concentrations or exploring the photoconductivity under applied hydrostatic pressure, using IR-excitation.

In order to investigate the influence of isovalent traps on the thermoelectric properties of semiconductors, measurements of the Seebeck coefficient have been performed. Whereas the electric-field driven electronic transport in n-type (Ga,In)(N,As) and (B,Ga,In)As differs considerably from that of n-type GaAs, the temperature-gradient driven electronic transport is very similar for the three semiconductors, despite the distinct differences in the conduction band structure of (Ga,In)(N,As) and (B,Ga,In)As compared to GaAs. From a thermoelectric point of view, both (Ga,In)(N,As) and (B,Ga,In)As appear with crystalline character rather than amorphous as indicated by electrical transport results. Here, further insight could be achieved from measurements at low temperatures, i.e. in the hopping regime. This hopping thermopower might yield information about the strength of disorder fluctuations.

A very rich and interesting field of research is the influence of magnetic interactions on the transport phenomena in semiconductors. Although the area of magnetic semiconductors has been extensively studied in the past, the hopping regime of electrical transport was mostly omitted up to now. However, it was

shown within the present work that the hopping transport in an impurity band is significantly influenced by magnetic interactions. Isovalent Mn ions with half filled Mn-3d shells introduce large localized magnetic moments that interact with the localized donor electrons. For Mn concentrations of several percent, these interactions in conjunction with disorder effects result in extremely large magnetoresistance effects observed in this and other II-Mn-VI compounds. Further theoretical modeling is required to explore the situation and to clarify, if the proposed mechanisms withstand a quantitative analysis. Possibilities for further experimental research might include the influence of the exchange integrals done by hydrostatic pressure experiments.

New aspects of the metal-insulator transition were discovered in a situation where the impurity band itself consists of impurities that provide localized magnetic moments, as it is the case in InSb:Mn. It was found that InSb:Mn and InSb:Ge samples reveal distinct differences in their electric resistivity near the metal-insulator transition, although Mn and Ge are acceptors of comparable depth. The distinctly different behavior of InSb:Mn compared to InSb:Ge arises from the magnetic nature of Mn ions. The local exchange interaction between the hole spin of the Mn acceptor and the $S = 5/2$ spin of its $3d^5$ shell is the dominant correlation effect, leading to the formation of an antiferromagnetic alignment of the Mn $3d^5$ spins along the percolation path, which in turn inhibits hopping of holes between neighboring Mn sites and leads to a splitting of the acceptor states. Thus a magnetic field, causing a parallel alignment of the $3d^5$ spins, strongly advances the transport situation leading to extraordinary large negative magnetoresistance effects at low temperature. Under hydrostatic pressure the exchange interaction was shown to be strongly amplified.

Both transport scenarios of the magnetic systems at the vicinity of the metal-insulator transition, that in InSb:Mn and that in (Zn,Mn)Se:Cl, are beyond current theoretical models for hopping conduction, as these do not account for spin effects.

Despite the fact that research into the metal-insulator transition of doped semiconductors goes back quite a long way and many models are established for standard samples of n- and p-type conventional semiconductor alloys, it becomes clear that the progress in semiconductor technology yields many new semiconductor systems which provide new transport scenarios whose description goes far beyond the standard theories. This makes research of the metal-insulator transition still an interesting and active research area of semiconductor physics. Altogether, the present work was aimed at shedding some more light on the still numerous fundamental questions that arise from the interplay between localized and extended states in semiconductors.

Bibliography

[1] L. J. van der Pauw, Philips Res. Rep. **13**, 1 (1958).

[2] L. J. van der Pauw, Philips Tech. Rev. **20**, 22 (1958/59).

[3] J. Yaeger and M. A. Hrusch-Tupta, editors, *Low Level Measurements Handbook: Precision DC Current, Voltage, and Resistance Measurements, 5th edition*, Keithley Instruments Inc., 1998.

[4] H. Overhof and P. Thomas, *Electronic transport in hydrogenated amorphous semiconductors*, Springer (Berlin), 1989.

[5] National Institute of Standards and Technology, www.nist.gov (download of ITS-90 thermoelectric voltage files: http://srdata.nist.gov/ /its90/download/download.html).

[6] J. Nyström, Arkiv. Mat., Astron., Fysik **34A**, 1 (1947).

[7] D. E. Aspnes, Surf. Sci. **37**, 418 (1973).

[8] J. Teubert, *Magnetotransport in epitaktischen (Ga,In)(N,As)-Schichten*, Diplomarbeit, Philipps-University of Marburg, 2004.

[9] H. K. Mao, J. Xu, and P. M. Bell, J. Geophys. Res. - Solid **91**, 4673 (1986).

[10] F. Bassani, G. Iadonisi, and B. Preziosi, Rep. Prog. Phys. **37**, 1099 (1974).

[11] N. F. Mott, Rev. Mod. Phys. **40**, 677 (1968).

[12] B. Shklovskii and A. L. Efros, *Electronic properties of doped semiconductors*, Sringer (Berlin), 1984.

[13] F. Gebhard, *The Mott metal-insulator transition: models and methods*, Springer (Berlin), 2008.

[14] P. W. Anderson, Phys. Rev. **109**, 1492 (1958).

[15] B. Gudden and W. Schottky, Z. Techn. Phys. **16**, 323 (1935).

[16] J. A. Chroboczek, E. W. Prohofsky, and R. J. Sladek, Phys. Rev. **169**, 593 (1968).

[17] H. Fritzsche, J. Phys. Chem. Solids **6**, 69 (1958).

[18] H. Fritzsche and K. Lark-Horovitz, Phys. Rev. **99**, 400 (1955).

[19] B. Shklovskii and I. S. Shlimak, Sov. Phys. Semiconduct. **6**, 104 (1972).

[20] H. Fritzsche and M. Cuevas, Phys. Rev. **119**, 1238 (1960).

[21] N. F. Mott and E. A. Davis, *Electronic processes in noncrystalline materials*, Clarendon Press (Oxford), 1979.

[22] N. F. Mott, J. Non-Cryst. Solids **1**, 1 (1968),

[23] S. D. Baranovskii, T. Faber, F. Hensel, and P. Thomas, J. Phys.: Cond. Mat. **9**, 2699 (1997).

[24] M. Grünewald, P. Thomas, and D. Würtz, phys. status solidi (b) **100**, K139 (1980).

[25] W. Czaja, Festkörperprobleme **11**, 65 (1971).

[26] J. J. Hopfield, D. G. Thomas, and R. T. Lynch, Phys. Rev. Lett. **17**, 312 (1966).

[27] P. J. Dean, J. Lumin. **1–2**, 399 (1970).

[28] S. Fahy and E. P. O'Reilly, Appl. Phys. Lett. **83**, 3731 (2003).

[29] S. Fahy and E. P. O'Reilly, Physica E **21**, 881 (2004).

[30] R. A. Faulkner, Phys. Rev. **175**, 991 (1968).

[31] J. C. Phillips, Phys. Rev. Lett. **22**, 285 (1969).

[32] A. C. Aten, J. H. Haanstra, and H. de Vries, Philips Res. Rep. **20**, 395 (1965).

[33] P. J. Klar et al., Appl. Phys. Lett. **76**, 3439 (2000).

[34] J. Wu et al., Phys. Rev. B **68**, 195202 (2003).

[35] F. Masia et al., Phys. Rev. B **73**, 073201 (2006).

[36] G. Pettinari et al., Phys. Rev. Lett. **98**, 146402 (2007).

[37] G. Pettinari et al., Phys. Rev. B **74**, 245202 (2006).

[38] A. Lindsay and E. P. O'Reilly, Phys. Rev. Lett. **93**, 196402 (2004).

[39] J. F. Geisz and D. J. Friedman, Semicond. Sci. Technol. **17**, 769–777 (2002).

[40] A. R. Adams, Electronic Lett. **40**, 1086 (2004).

[41] A. L. Allred, J. Inorg. Nucl. Chem. **17**, 215 (1961).

[42] H. P. Hjalmarson, P. Vogl, D. J. Wolford, and J. D. Dow, Phys. Rev. Lett. **44**, 810 (1980).

[43] D. J. Wolford, J. A. Bradley, K. Fry, and J. Thompson, *The nitrogen isoelectronic trap in GaAs*, in *Proceedings of the 17th international conference on the physics of semiconductors*, page 627, 1984.

[44] X. Liu, M.-E. Pistol, L. Samuelson, S. Schwetlick, and W. Seifert, Appl. Phys. Lett. **56**, 1451 (1990).

[45] G. Hart and A. Zunger, Phys. Rev. B **62**, 13522 (2000).

[46] P. R. C. Kent and A. Zunger, Phys. Rev. B **64**, 115208 (2001).

[47] A. Lindsay and E. P. O'Reilly, Phys. Rev. B **76**, 075210 (2007).

[48] W. Shan et al., Phys. Rev. Lett. **82**, 1221 (1999).

[49] A. Lindsay, private communication.

[50] J. Teubert, P. J. Klar, and W. Heimbrodt, phys. status solidi (c) **5**, 858 (2008).

[51] J. Teubert et al., phys. status solidi (b) **244**, 431 (2007).

[52] J. Teubert et al., Appl. Phys. Lett. **84**, 747 (2004).

[53] G. Hart and A. Zunger, *BAs-GaAs semiconductor alloys as a photovoltaic alternative to nitride alloys*, in *Proceedings of the NCPV program review meeting, Denver (CO), USA*, pages 125–126, 2000.

[54] W. Shan et al., J. Appl. Phys **93**, 2696 (2003).

[55] N. G. Szwacki and Boguslawski, Phys. Rev. B **64**, 161201 (2001).

[56] T. Hofmann et al., *The inertial-mass scale for free-charge-carriers in semiconductor heterostructures*, in *Physics of semiconductors: 27th international conference on the physics of semiconductors*, edited by J. Menendez and C. Van de Walle, page 455, 2005.

[57] A. Lindsay and E. P. O'Reilly, Physica B **340–342**, 434 (2003).

[58] K. Seeger, *Semiconductor physics*, Springer (Berlin), 2002.

[59] P. Y. Yu and M. Cardona, *Fundamentals of semiconductors*, Springer (Berlin), 2001.

[60] V. Gottschalch, G. Leibiger, and G. Benndorf, J. Cryst. Growth **248**, 468 (2003).

[61] G. Bergmann, Phys. Rev. B **28**, 2914 (1983).

[62] J. Chroboczek, A. Klokocki, and K. Kopalko, J. Phys. C **7**, 3042 (1974).

[63] J. A. Chroboczek and R. J. Sladek, Phys. Rev. **151**, 595 (1966).

[64] D. Ferre, H. Dubois, and G. Biskubski, phys. status solidi (b) **70**, 81 (1975).

[65] L. Halbo and R. J. Sladek, Phys. Rev. **173**, 794 (1968).

[66] H. Kahlert, G. Landwehr, A. Schlachetzki, and H. Salow, Z. Phys. B **24**, 361 (1976).

[67] W. W.-Y. Lee and R. J. Sladek, Phys. Rev. **158**, 788 (1967).

[68] D. Lemoine, C. Pelletier, S. Rolland, and R. Granger, Phys. Lett. A **56**, 493 (1976).

[69] R. Mansfield and L. Kusztelant, J. Phys. C **11**, 4157 (1978).

[70] J. L. Robert, A. Raymond, R. L. Aulombard, and C. Bousquet, Philos. Mag. B **42**, 1003 (1980).

[71] J. R. Sites and A. K. Nedoluha, Phys. Rev. B **24**, 4309 (1981).

[72] R. J. Sladek, J. Phys. Chem. Solids **5**, 157 (1958).

[73] H. Tokumoto, R. Mansfield, and M. J. Lea, Solid State Commun. **35**, 961—964 (1980).

[74] H. Tokumoto, R. Mansfield, and M. J. Lea, Philos. Mag. B **46**, 93 (1982).

[75] A. K. Walton, J. Phys. C **13**, 6677 (1980).

[76] A. K. Walton and J. C. Dutt, J. Phys. C **10**, L29 (1977).

[77] N. Mikoshiba, Phys. Rev. **127**, 1962 (1962).

[78] N. Mikoshiba and S.-i. Gonda, Phys. Rev. **127**, 1954 (1962).

[79] Y. Yafet, R. W. Keyes, and E. N. Adams, J. Phys. Chem. Solids **1**, 137 (1956).

[80] M. C. Maliepaard et al., Phys. Rev. B **39**, 1430 (1989).

[81] M. E. Raikh, J. Czingon, Q.-Y. Ye, and F. Koch, Phys. Rev. B **45**, 6015 (1992).

[82] J. Woods and C. Chen, Phys. Rev. **135**, A1462 (1964).

[83] M. E. Raikh, Solid State Commun. **75**, 935 (1990).

[84] W. Schirmacher, Phys. Rev. B **41**, 2461 (1990).

[85] Q.-Y. Ye, B. I. Shklovskii, A. Zrenner, and F. Koch, Phys. Rev. B **41**, 8477 (1990).

[86] R. Rentsch et al., phys. status solidi (b) **127**, 691 (1986).

[87] A. Lindsay and E. P. O'Reilly, Solid State Commun. **118**, 313 (2001).

[88] A. Lindsay and E. P. O'Reilly, Physica E **21**, 901 (2004).

[89] S. Paul, J. B. Roy, and P. K. Basu, J. Appl. Phys. **69**, 827 (1991).

[90] S. K. Brierley, H. T. Hendriks, W. E. Hoke, P. J. Lemonias, and D. G. Weir, Appl. Phys. Lett. **63**, 812 (1993).

[91] D. Lancefield, A. R. Adams, and M. A. Fisher, J. Appl. Phys. **62**, 2342 (1987).

[92] D. Lancefield, A. R. Adams, and B. J. Gunney, Appl. Phys. Lett. **45**, 1121 (1984).

[93] I. A. Buyanova, W. M. Chen, and C. W. Tu, Semicond. Sci. Technol. **17**, 815 (2002).

[94] H. Grüning et al., phys. status solidi (c) **1**, 109 (2004).

[95] C. Herring, Phys. Rev. **96**, 1163 (1954).

[96] H. Overhof and W. Beyer, Philos. Mag. B **43**, 433 (1981).

[97] D. Geisz, J.F. Friedman et al., J. Cryst. Growth **225**, 372 (2001).

[98] J. Geisz et al., Appl. Phys. Lett. **76**, 1443 (2000).

[99] N. W. Ashcroft and N. D. Mermin, *Festkörperphysik*, Oldenbourg Wissenschaftsverlag GmbH (München), 2001.

[100] E. Conwell and V. F. Weisskopf, Phys. Rev. **77**, 388 (1950).

[101] V. A. Johnson and K. Lark-Horovitz, Phys. Rev. **92**, 226 (1953).

[102] O. V. Emelyanenko, E. E. Klotinsh, D. N. Nasledov, and V. G. Sidorov, phys. status solidi **12**, K89 (1965).

[103] T. H. Geballe and G. W. Hull, Phys. Rev. **94**, 1134 (1954).

[104] T. H. Geballe and G. W. Hull, Phys. Rev. **98**, 940 (1955).

[105] C. Skierbiszewski et al., Appl. Phys. Lett. **76**, 2409 (2000).

[106] M. Cardona, Phys. Rev. **121**, 752 (1961).

[107] R. Trommer and M. Cardona, Phys. Rev. B **17**, 1865 (1978).

[108] G. Leibiger et al., Phys. Rev. B **67**, 195205 (2003).

[109] R. Leigh et al., Semicond. Sci. Technol. **9**, 1054 (1994).

[110] R. C. Newman, F. Thompson, M. Hyliands, and R. F. Peart, Solid State Commun. **10**, 505 (1972).

[111] H. C. Alt and Y. V. Gomeniuk, Phys. Rev. B **70**, 161314 (2004).

[112] H. C. Alt, Y. V. Gomeniuk, and G. Mussler, Semicond. Sci. Technol. **21**, 1425 (2006).

[113] S. Kurtz et al., Appl. Phys. Lett. **78**, 748 (2001).

[114] J. Wagner, T. Geppert, K. Köhler, P. Ganser, and N. Herres, J. Appl. Phys. **90**, 5027 (2001).

[115] P. Ball, Nature **404**, 918 (2000).

[116] T. Dietl, H. Ohno, F. Matsukura, J. Cibert, and D. Ferrand, Science **287**, 1019 (2000).

[117] G. A. Prinz, Science **282**, 1660 (1998).

[118] W. Heimbrodt, *Habilitationsschrift*, Humboldt Universität, Berlin, 1996.

[119] B. Daniel, K. C. Agarwal, J. Lupaca-Schomber, C. Klingshirn, and M. Hetterich, Appl. Phys. Lett. **87**, 212103 (2005).

[120] H. Abad, B. T. Jonker, W. Y. Yu, S. Stoltz, and A. Petrou, Appl. Phys. Lett. **66**, 2412 (1995).

[121] C. M. Townsley et al., Phys. Rev. B **53**, 10983 (1996).

[122] T. Dietl, L. Swierkowski, J. Jaroszynski, M. Sawicki, and T. Wojtowicz, Phys. Scr. **T14**, 29 (1986).

[123] Y. Shapira, N. F. Oliveira, P. Becla, and T. Q. Vu, Phys. Rev. B **41**, 5931 (1990).

[124] Y. Shapira et al., Phys. Rev. B **34**, 4187 (1986).

[125] Y. Shapira et al., J. Appl. Phys. **57**, 3210 (1985).

[126] H. Kamimura, Philos. Mag. B **52**, 541 (1985).

[127] A. Twardowski, M. von Ortenberg, M. Demianiuk, and R. Pauthenet, Acta Phys. Polon. A **67**, 339 (1985).

[128] J. J. Davies, J. E. Nicholls, and C. P. Hilton, J. Phys. C **18**, L1035 (1985).

[129] P. J. Klar, *Magneto-optical studies of wide-gap dilute magnetic semiconductors heterostructures and quantum dots*, PhD thesis, University of East Anglia, Norwich, 1996.

[130] W. Heimbrodt and P. J. Klar, *Magnetic nanostructures*, chapter 1, page 17, American scientific publishers (Stevenson Ranch, CA), 2002.

[131] Landolt-Börnstein, *Semiconductors - Physics of group IV elements and III-V compounds*, volume 17 a, Springer (Berlin), 1982.

[132] D. L. Partin, J. Heremans, and C. M. Thrush, J. Cryst. Growth **175–176**, 860 (1997).

[133] M. D. Banus and M. C. Lavine, J. Appl. Phys. **40**, 409 (1969).

[134] J. Schneider, U. Kaufmann, W. Wilkening, M. Baeumler, and F. Köhl, Phys. Rev. Lett. **59**, 240 (1987).

[135] A. Kudelski et al., Phys. Rev. Lett. **99**, 247209 (2007).

[136] F. Hamdani, A. R. Gõni, K. Syassen, and R. Triboulet, phys. status solidi (b) **223**, 171 (2001).

[137] S. A. Obukhov, phys. status solidi (b) **242**, 1298 (2005).

List of publications

- J. Teubert, P. J. Klar, W. Heimbrodt, K. Volz, W. Stolz, P. Thomas, G. Leibiger, V. Gottschalch, *Enhanced weak Anderson localization phenomena in the magnetoresistance of n-type (Ga,In)(N,As)*, Appl. Phys. Lett. **84**, 747 (2004).
- J. Teubert, P. J. Klar, W. Heimbrodt, K. Volz, W. Stolz, *Influence of N on the electron transport in (Ga,In)(N,As) probed by magnetotransport under hydrostatic pressure*, IEE Proc., Optoelectron. **151**, 357 (2004)
- J. Teubert, P. J. Klar, W. Heimbrodt, K. Volz, W. Stolz, A. Polimeni, M. Capizzi, *Competition of N-passivation and Te-passivation in hydrogenation of Te-doped (Ga,In)(N,As)*, Physica E **32**, 218 (2006)
- J. Teubert, P. J. Klar, W. Heimbrodt, V. Gottschalch, E. P. O'Reilly, *Effect of localized B and N states on the magneto-transport of (B,Ga,In)As and (Ga,In)(N,As)*, phys. status solidi (b) **244**, 431 (2007)
- M. T. Elm, J. Teubert, P. J. Klar, W. Heimbrodt, C. Michel, P. Thomas, S. Baranovskii, *Transport study of the annealing-induced transition from $Ga_{1-x}Mn_xAs$ alloys to GaAs:Mn/MnAs hybrids*, AIP Conf. Proc. **893**, 1275 (2007)
- P. J. Klar, J. Teubert, M. Güngerich, T. Niebling, H. Grüning, W. Heimbrodt, K. Volz, W. Stolz, A. Polimeni, M. Capizzi, E. P. O'Reilly, A. Lindsay, M. Galuppi, L. Geelhaar, H. Riechert und S. Tomic, *Hydrostatic pressure experiments on dilute nitride alloys* phys. status solidi (b) **244**, 24 (2007)
- K. Volz, W. Stolz, J. Teubert, P. J. Klar, W. Heimbrodt, F. Dimroth, C. Baur, A. W. Bett, *Doping, electrical properties and solar cell application of (Ga,In)(N,As)* in *Springer series in materials science 105: dilute III-V nitride semiconductors and material systems*, edited by A. Erol, Springer (Berlin), 2008
- J. Teubert, P. J. Klar, W. Heimbrodt, *Metal-insulator transition in n-BGaInAs*, phys. status solidi (c) **5**, 858 (2008)
- G. Homm, P. J. Klar, J. Teubert, and W. Heimbrodt, *Seebeck coefficients of n-type (Ga,In)(N,As), (B,Ga,In)As and GaAs*, Appl. Phys. Lett. **93**, 042107 (2008)

Acknowledgments

An dieser Stelle möchte ich all denen meinen besonderen Dank aussprechen, die mich während der Erstellung dieser Arbeit in vielfacher Hinsicht unterstützt haben. In (fast) beliebiger Reihenfolge gilt mein Dank:

Prof. Dr. Peter J. Klar für die Betreuung dieser Arbeit, für sein unermüdliches Engagement und sein Vertrauen sowie die vielen Diskussionen und Ratschläge.

Prof. Dr. Bruno K. Meyer für die Begutachtung dieser Arbeit und das nette "Betriebsklima" im Institut, das er nach Kräften fördert.

Prof. Dr. Wolfram Heimbrodt und den Mitgliedern seiner Arbeitsgruppe an der Uni Marburg für die vielen Jahre der guten Zusammenarbeit und das stets angenehme und humorvolle Miteinander - ebenso den übrigen Mitgliedern der AG Experimentelle Halbleiterphysik.

Ähnliches gilt für die noch junge, wachsende Abteilung Klar sowie für alle Mitglieder des I. Physikalischen Instituts der Uni Gießen – ein Arbeitsplatz mit Wohlfühlcharakter. Ein Dank insbesondere auch an die vielen "dienstbaren Geister", deren Arbeit man im Alltag leider zu oft übersieht.

Für ihre Mitarbeit und Unterstützung im Labor: Matthias Elm, Gert Homm und Dr. Sergei Obukhov (v.a. Transportmessungen), Christian Karcher, Björn Metzger und Tobias Niebling (Modulationsspektroskopie), Alexej Chernikov, Swantje Horst und Christoph Lange (PL unter Druck, zeitaufgelöste Messungen).

Der Feinmechanischen Werkstatt und dem Elektroniklabor, Uni Marburg, für die stets kompetente Hilfe bei technischen Problemen und die Herstellung aller im Rahmen dieser Arbeit verwendeten Spezialanfertigungen. Die Sachen haben nicht nur funktioniert, es hat auch immer Spaß gemacht, damit zu arbeiten. Ebenso allen anderen in Marburg und Gießen, die mir mit ihrem technischen Wissen und ihrer Hilfsbereitschaft bei so manchem Problem im Labor zur Seite stehen konnten.

Für die Bereitstellung der Proben: Prof. Dr. Volker Gottschalch und Dr. Gunnar Leibiger, Uni Leipzig, sowie Dr. John F. Geisz, National Renewable Energy Laboratory in Golden, CO (BGaAs, BGaInAs und GaAs); Dr. habil. Wolfgang Stolz und Dr. habil. Kerstin Volz, Uni Marburg (GaInNAs); PD Dr. Michael Hetterich, Uni Karlsruhe (ZnMnSe); Dr. Serguei Obukhov, A. F. Ioffe Institute of Physics & Technology, St. Petersburg (InSb).

Dr. Andrew Lindsay and Prof. Dr. Eoin P. O'Reilly for their valuable theoretical work and many fruitful discussions.

Für viele hilfreiche Diskussionen (alphabetisch): Prof. Dr. Sergei D. Baranovskii, Dr. Sangam Chatterjee (auch für die schnelle und unbürokratische Bereitstellung von allerlei Messgerätschaften ein herzliches Dankeschön), Prof. Dr. Florian Gebhard, Prof. Dr. Wolfram Heimbrodt, Prof. Dr. Peter Thomas, Prof. Dr. Gerhard Weiser, alle Uni Marburg, und die bereits oben genannten.

Dem Graduiertenkolleg „Electron-Electron Interactions in Solids“ und dessen Sprecher Prof. Dr. Florian Gebhard für die gute Ausbildungsarbeit und die finanzielle Unterstützung einiger meiner Konferenzreisen.

Den Korrekturlesern für ihre unschätzbar wertvolle Arbeit.

Den Äthiopiern für die Erfindung des Kaffees (Blitzrecherche auf wikipedia.org).

Meinen Freunden dafür, dass sie es sind.

Meiner Familie, insbesondere meinen Eltern, für meine Förderung, ihre Ermutigungen und ihr Vertrauen.

Meiner Frau Marina für so vieles, was sich nur schwer in Worte fassen lässt.

Danke!

Ich erkläre:

Ich habe die vorgelegte Dissertation selbständig und ohne unerlaubte fremde Hilfe und nur mit den Hilfen angefertigt, die ich in der Dissertation angegeben habe. Alle Textstellen, die wörtlich oder sinngemäß aus veröffentlichten Schriften entnommen sind, und alle Angaben, die auf mündlichen Auskünften beruhen, sind als solche kenntlich gemacht. Bei den von mir durchgeführten und in der Dissertation erwähnten Untersuchungen habe ich die Grundsätze guter wissenschaftlicher Praxis, wie sie in der „Satzung der Justus-Liebig-Universität Gießen zur Sicherung guter wissenschaftlicher Praxis“ niedergelegt sind, eingehalten.

Jörg Teubert